

# Molecule and dust synthesis in the inner winds of oxygen-rich Asymptotic Giant Branch (AGB) stars

**Inauguraldissertation**

zur

Erlangung der Würde eines Doktors der Philosophie

vorgelegt der

Philosophisch-Naturwissenschaftlichen Fakultät

der Universität Basel

von

David Leon

Gobrecht

aus Gebenstorf

Aargau

Basel, 2016

Originaldokument gespeichert auf dem Dokumentenserver der Universität Basel  
edoc.unibas.ch

Genehmigt von der Philosophisch-Naturwissenschaftlichen Fakultät

auf Antrag von

Prof. Dr. F.-K. Thielemann, PD Dr. Isabelle Cherchneff, PD Dr. Dahbia Talbi

Basel, den 17. Februar 2015

Prof. Dr. Jörg Schibler  
Dekanin/Dekan



IK Tau as seen by Two Micron All Sky Survey, 2MASS, (top) and Sloan Digital Sky Survey, SDSS, (bottom) from the Aladin Sky Atlas in the Simbad astronomical database (Wenger et al., 2000)

## Abstract

This thesis aims to explain the masses and compositions of prevalent molecules, dust clusters, and dust grains in the inner winds of oxygen-rich AGB stars. In this context, models have been developed, which account for various stellar conditions, reflecting all the evolutionary stages of AGB stars, as well as different metallicities. Moreover, we aim to gain insight on the nature of dust grains, synthesised by inorganic and metallic clusters with associated structures, energetics, reaction mechanisms, and finally possible formation routes. We model the circumstellar envelopes of AGB stars, covering several C/O ratios below unity and pulsation periods of 100 - 500 days, by employing a chemical-kinetic approach. Periodic shocks, induced by pulsation, with speeds of 10 - 32 km s<sup>-1</sup> enable a non-equilibrium chemistry to take place between 1 and 10 R<sub>\*</sub> above the photosphere. The various models include the well-studied, galactic Mira variables like IK Tau and TX Cam, galactic S-stars, semi-regular variables of type SRa and SRb, as well as Mira stars of lower metallicity in the Magellanic clouds. In addition, we perform quantum-chemical calculations on the Density Functional Theory (DFT) level for several alumina and silicate clusters, in order to obtain structures, electronic properties, and infrared (IR) spectra of the potential dust components.

The results for the gas phase agree well with the most recent observational data for IK Tau and VY CMa. Major *parent* molecules form in the shocked gas under non-equilibrium conditions and include CO, H<sub>2</sub>O, SiO, SiS, SO and SO<sub>2</sub>, as well as the unexpected carbon-bearing species HCN, CS and CO<sub>2</sub>, and the recently detected phosphorous species PO and PN. In the galactic models, small alumina clusters form and condense efficiently close to the star. In the case of galactic Miras, silicate clusters with forsterite mineralogy form and coalesce around 4 R<sub>\*</sub>. In the lower metallicity and semi-regular models, the dust formation is hampered by the unavailability of the critical elements (Si and Al), low densities, and high temperatures. The dust/gas mass ratio ranges from 10<sup>-9</sup> to 10<sup>-5</sup> for alumina, and from 10<sup>-6</sup> to 10<sup>-3</sup> for forsterite, and agrees with the dust-to-gas mass ratio derived for oxygen-rich AGB stars.

For the first time, a complete non-equilibrium model - including gas phase chemistry, cluster growth and dust formation - is built up self-consistently, and explaining successfully the most recent observations.

# Contents

<b>1</b>	<b>Introduction</b>	<b>10</b>
<b>2</b>	<b>AGB Stars</b>	<b>18</b>
2.1	Evolution of Low- and Intermediate Mass Stars . . . . .	18
2.2	Mira Stars . . . . .	18
2.3	Semi-Regular Variables (SRVs) . . . . .	21
2.4	S-type AGB Stars . . . . .	24
2.5	Stars in the Magellanic Clouds . . . . .	24
<b>3</b>	<b>Physical Model</b>	<b>27</b>
3.1	Structure of the Envelope . . . . .	27
3.2	Immediate Shock Layer . . . . .	30
3.3	Mass-loss, Densities and Velocities in the Wind . . . . .	32
3.4	Stellar Mass . . . . .	38
3.5	Pulsation . . . . .	40
<b>4</b>	<b>Chemistry</b>	<b>41</b>
4.1	Initial Elemental Compositions . . . . .	41
4.2	Metallicity . . . . .	43
4.3	Thermodynamic Equilibrium . . . . .	44
4.4	Chemical-Kinetic Networks . . . . .	47
4.5	Post-Shock Chemistry . . . . .	50
4.6	Cluster Structures . . . . .	52
4.7	Gas-Phase Nucleation . . . . .	56
4.8	Coalescence and Condensation . . . . .	60
<b>5</b>	<b>Results for IK Tau</b>	<b>62</b>
5.1	Initial Photospheric Abundances . . . . .	62
5.2	Post-Shock Chemistry . . . . .	63
5.3	Sulphur Chemistry . . . . .	70
5.4	Nitrogen and Phosphorus Chemistry . . . . .	75
5.5	Clusters and Dust Grains . . . . .	76
5.6	Alumina . . . . .	76
5.7	Silicates . . . . .	78
5.8	A High Gas Number Density Case . . . . .	81
<b>6</b>	<b>Results for Semi-regular Variables</b>	<b>84</b>
6.1	Initial Photospheric Abundances . . . . .	84
6.2	Post-Shock Chemistry . . . . .	85
6.3	Clusters and Dust Grains . . . . .	89

<b>7</b>	<b>Results for S-type AGB Stars</b>	<b>92</b>
7.1	Initial Photospheric Abundances . . . . .	92
7.2	Post-Shock Chemistry . . . . .	93
7.3	Clusters and Dust Grains . . . . .	96
<b>8</b>	<b>Results for Subsolar Metallicities</b>	<b>102</b>
8.1	Initial Photospheric Abundances . . . . .	102
8.2	Post-Shock Chemistry . . . . .	102
8.3	Clusters and Dust Grains . . . . .	103
<b>9</b>	<b>Summary</b>	<b>108</b>

## List of Figures

1	The Hertzsprung-Russel diagram . . . . .	10
2	Evolutionary tracks of a star in the Hertzsprung-Russell-diagram . . . . .	19
3	Discovery of IK Tau . . . . .	19
4	Physical structure of the envelope (Bertschinger & Chevalier, 1985) . . . . .	27
5	Results of the atmospheric models of Nowotny et al. (2010) . . . . .	29
6	Gas parcel excursions at different radii . . . . .	32
7	Post-shock velocities in the Lagrangian frame . . . . .	33
8	Post-shock number densities . . . . .	34
9	Post-shock number temperatures . . . . .	34
10	Observed velocity profile in IK Tau (Decin et al., 2010a) . . . . .	36
11	Adiabatic gas parcel excursion for different stellar masses . . . . .	39
12	Elemental gas phase compositions . . . . .	43
13	Elemental gas phase compositions at different metallicities . . . . .	44
14	H and H <sub>2</sub> abundances in the post-shock gas . . . . .	52
15	Structure of alumina clusters . . . . .	54
16	Alumina cluster energies relative to semi-classical energies . . . . .	55
17	Silicate cluster nucleation scheme (Goumans & Bromley (2012)) . . . . .	59
18	Molecular abundances in the immediate shock layer at 1 R <sub>*</sub> . . . . .	63
19	Molecular abundances in the immediate shock layer at 3 R <sub>*</sub> . . . . .	64
20	Molecular abundances in the parcel excursion at 1R <sub>*</sub> . . . . .	65
21	Molecular abundances in the parcel excursion at 3R <sub>*</sub> . . . . .	66
22	Molecular abundances as a function of radius . . . . .	67
23	Comparison of modelled and observed abundances . . . . .	69
24	Alumina cluster abundances . . . . .	78
25	Alumina grain size distributions . . . . .	79
26	Silicate cluster abundances . . . . .	79
27	Silicate cluster abundances at 3.5 R <sub>*</sub> . . . . .	80
28	Forsterite grain size distributions . . . . .	81
29	Alumina grain size distributions in the ×10 density case . . . . .	82
30	Forsterite grain size distributions in the ×10 density case . . . . .	83
31	Elemental gas phase compositions: SRa and SRb case . . . . .	85
32	Molecular abundances at 1R <sub>*</sub> in the SRb case . . . . .	86
33	Molecular abundances versus radius in the SRb case . . . . .	87
34	Molecular abundances at 1R <sub>*</sub> in the SRa case . . . . .	88
35	Molecular abundances versus radius in the SRa case (10 km/s) . . . . .	88
36	Comparison of modelled and observed abundances in the SRa case . . . . .	89
37	Alumina grain size distribution in the SRa case . . . . .	90
38	Forsterite grain size distribution in the SRa case . . . . .	91
39	Molecular abundances versus radius in the S-star case (20 km/s) . . . . .	93
40	Molecular abundances versus radius in the S-star case (32 km/s) . . . . .	94

41	Comparison of modelled with observed abundances in S-type stars . . . . .	95
42	Molecular abundances at $1R_*$ in the S-star case (20 km/s) . . . . .	96
43	Molecular abundances at $1R_*$ in the S-star case (32 km/s) . . . . .	98
44	Alumina grain size distribution in S-type case (20 km/s) . . . . .	99
45	Alumina grain size distribution in S-type case (32 km/s) . . . . .	100
46	Forsterite grain size distribution in S-type case (20 km/s) . . . . .	100
47	Forsterite grain size distribution in S-type case (32 km/s) . . . . .	101
48	Molecular abundances at $1R_*$ in the LMC case . . . . .	103
49	Molecular abundances at $1R_*$ in the SMC case . . . . .	104
50	Molecular abundances versus radius in the LMC case . . . . .	104
51	Molecular abundances versus radius in the SMC case . . . . .	105
52	Alumina grains size distribution in the LMC . . . . .	106
53	Alumina grains size distribution in the SMC . . . . .	106
54	Forsterite grains size distribution in the LMC . . . . .	107
55	Forsterite grains size distribution in the SMC . . . . .	107

## List of Tables

1	Stellar parameters used for modelling IK Tau . . . . .	21
2	Stellar parameters used for modelling TX Cam . . . . .	21
3	Stellar parameters of semi-regular variables of class SRb. . . . .	23
4	Stellar parameters of S-type AGB stars . . . . .	25
5	Gas conditions in the preshock, shock front, and post-shock zone . . . . .	35
6	Solar abundances (Asplund et al., 2009) . . . . .	42
7	Molecular equilibrium abundances . . . . .	46
8	Chemical reaction types . . . . .	47
9	Chemical species . . . . .	51
10	Silaformyl radicals and silanone reactions . . . . .	60
11	Molecular equilibrium abundances in comparison . . . . .	62
12	Comaprison of modelled and observed molecular abundances . . . . .	68
13	Dust-to-gas mass ratios . . . . .	77
14	Molecular equilibrium abundances in the SRb and SRa case . . . . .	85
15	Molecular equilibrium abundances in the S-type case . . . . .	92
16	Observed molecular abundances in the S-type case . . . . .	97
17	Dust-to-gas mass ratios in the S-type case . . . . .	98
18	Molecular equilibrium abundances in the SMC and LMC case . . . . .	102
19	Dust-to-gas mass ratio in the LMC and SMC case . . . . .	105



# 1 Introduction

Asymptotic Giant Branch (AGB) stars are a family of stars with remarkable properties and phenomena. They represent the largest and reddest known stars. Therefore, AGB stars reside on top right corner of the Hertzsprung-Russel-Diagramm (HRD) characterised by high luminosities ( $L_* \sim 10^3 - 10^4 L_\odot$ ) and rather cool surface temperatures ( $T_* = 1800 - 3000 \text{ K}$ ) as can be seen in Figure 1.

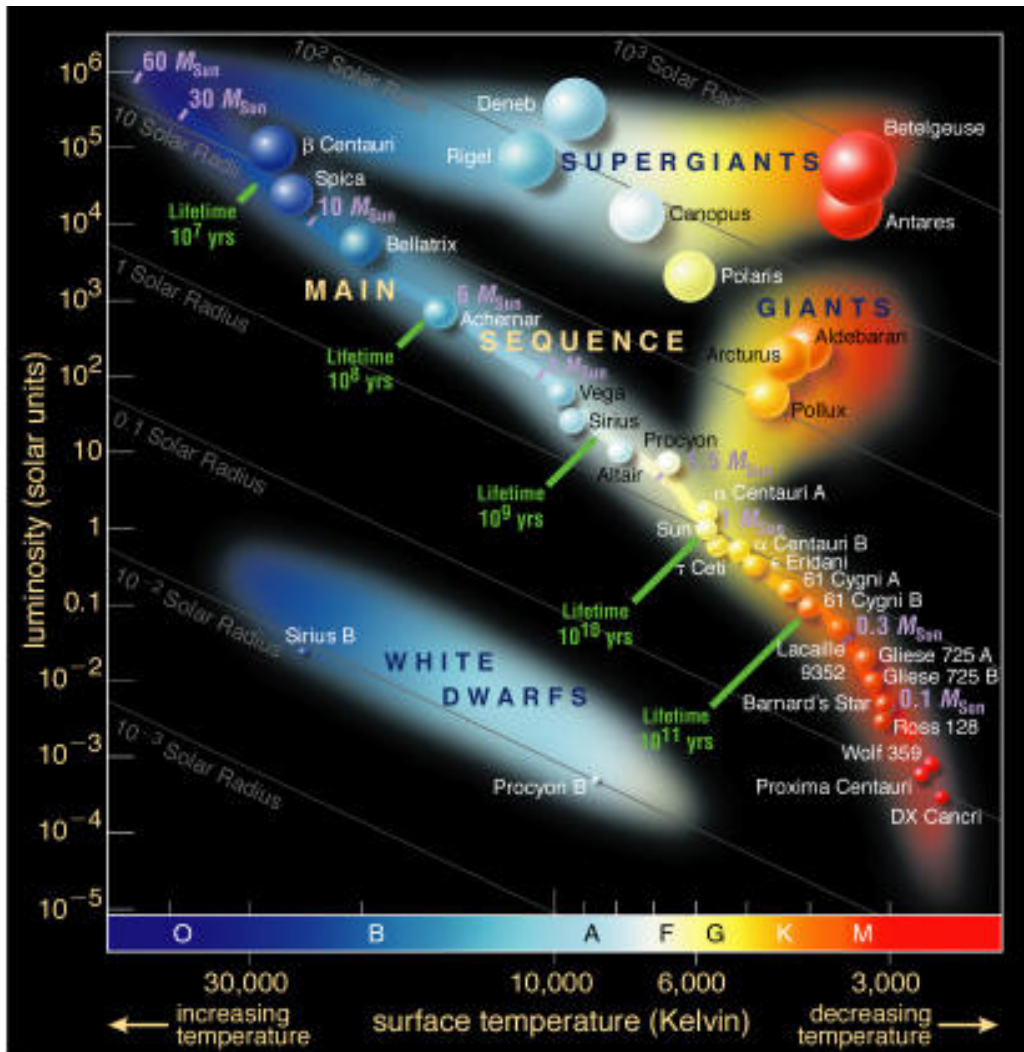


Figure 1: The Hertzsprung-Russel diagram classifies stars according to their surface temperature  $T_*$  and their luminosities. AGB stars reside on the top right part of the diagram, implying rather cool surface temperatures and high luminosities. The figure is taken from [www.daviddarling.info](http://www.daviddarling.info).

Nuclear fusion, which supplies the AGB star with energy (luminosity), occurs in shells surrounding the inert and degenerate central part of the star. Moreover, AGB stars have a large convective envelope that penetrates the burning shells and mixing newly synthesised material to the surface. A particular interesting element found in the atmospheres of some AGB stars is technetium (Tc) (Little-Marenin & Little, 1979). Tc has no stable isotopes

and the half-life of the presumed isotope  $^{99}\text{Tc}$  of  $2 \times 10^5$  years is shorter than the lifetime of AGB stars. Its atmospheric presence means that it has been produced inside the star (presumably by the s-process), and that it has been brought to the stellar surface within that timescale. This is the first and direct evidence for the production of new elements inside stars.

The majority of AGB stars are long period variables (LPVs) implying that these stars pulsate in more or less regular intervals. Moreover, AGB stars lose mass in high amounts in the form of a dusty wind, thereby contributing significantly to the dust return in the interstellar medium (ISM), and to the Galactic Chemical Evolution (GCE). AGBs are along with red super giants, novae and supernovae the most important source for the enrichment of the ISM and thus responsible for the higher metallicity of successive stellar populations. During the evolution on the AGB thermal pulses (TPs) lead to strong luminosity variations, which significantly change the chemical composition of the atmosphere. The dusty mass-loss eventually terminates the life of an AGB star. Once the hydrogen-rich envelope is (almost) removed, the central remnant star is revealed. The naked central star becomes hotter and interacts with the expelled envelope. The star has entered the Planetary Nebula (PN) phase where the central star ionises and shapes its expelled envelope. Roughly one quarter of all post AGB stars undergo a final thermal pulse (explosive He ignition). As the envelope has been almost entirely removed, the star expands and cools to similar radii and temperatures as red giants. Thus, the star returns from the PN phase to the AGB phase. This rapid evolution is called *born again star* scenario.

This thesis focuses particularly on the chemistry of the inner wind in O-rich AGB stars including the formation of dust grains.

Stars not only emit radiation but also matter. In contrast to the solar wind AGB winds are dust-driven. The term dust-driven refers to the radiation pressure exerted by stellar photons on dust grains (i.e. photons transfer part of their momentum to dust grains located in the AGB atmospheres). In the case of dust-driven wind, grains can absorb (or scatter) radiation over a broad range of wavelengths. Such winds are thus also referred to as continuum-driven winds (Lamers & Cassinelli, 1999). In contrast, winds from younger and hotter stars like our Sun do not contain enough dust grains to drive the wind. In such a case, the opacity sources are lines of atomic and molecular transitions and the wind is called line-driven. The difference between the two types of stellar winds exhibits in various quantities such as Doppler shifts, terminal speeds and mass-loss rates.

Mass-loss is probably the most crucial property of AGB stars representing the late evolutionary stage of low- and intermediate mass stars. Mass-loss determines the lifetime of the star. The magnitude of mass-loss ranges from  $10^{-8}M_{\odot}/\text{yr}$  for irregular and semi-regular variables on the early AGB to  $10^{-4}M_{\odot}/\text{yr}$  for optically thick OH/IR stars. In order to initiate a mass-loss in such intensities two conditions are required: First, the stellar atmosphere is periodically levitated due to recurrent pulsations and second, dust grains are formed within

10R<sub>\*</sub> - the so called inner envelope - to efficiently gain momentum from stellar photons and to drag the gas along with it. During the evolution on the AGB a star evolves from low to high mass-loss rates and eventually reaches a superwind phase towards the tip of the AGB. Not only the amount of mass expelled in the circumstellar envelope but also the chemical composition changes during stellar evolution. Responsible for the change in the envelope chemistry are thermal pulses which dredge up fresh products of nucleosynthesis, mainly carbon, from inside the star. This is reflected in a time-dependent, increasing C/O ratio. As a consequence an initially oxygen-rich AGB star can turn into a carbon-rich AGB.

The photospheric C/O ratio determines the atmospheric chemistry, governed that Thermodynamic equilibrium (TE) applies (Habing & Olofsson, 2003). In stars with a carbon-rich chemistry (e.g. IRC+10216) - characterised by  $C/O > 1$  - carbonaceous molecules are expected. Indeed, a large variety of more than 60 predominantly carbonaceous molecules are detected in mm, sub-mm and IR surveys in IRC+10216, substantiating their presence for a wide range of gas conditions (Ziurys, 2006). Conversely, in oxygen-rich AGB stars ( $C/O < 1$ ) oxygen-bearing molecules are expected to be prevalent. Observations confirm the presence of (metal) oxides and water, but the number of detected molecular species constitutes around 25 (see e.g. Sanchez Contreras et al. 2011), far below the carbon-rich case. The diverse number of molecular-associated detections indicates a richer and more complex chemistry in C-rich environments. Possible reasons for this imbalance are the proximity of IRC+10216, the observational attention drawn to IRC+10216, and the presence of organic hydro-carbons, which serve as basic building blocks of life. In oxygen-rich AGB stars, inorganic compounds and processes play a role.

The nature of the dichotomy of oxygen-rich (M-type) and carbon-rich (C-type) AGB stars is based on the high binding energy of the triple bonded CO molecule (11 eV  $\approx$  127'650 K, (Tielens, 2010)) which forms at any C/O ratio in significant quantities and almost entirely locks up the lesser abundant element, namely C for  $C/O < 1$  and O for  $C/O > 1$ . As a consequence one expects no other oxygen-bearing molecule than CO in the envelope of carbon stars with  $C/O > 1$  and, on the other hand, no carbonaceous molecule except CO in oxygen-rich (M-type) stars with  $C/O < 1$ .

This dichotomy is broken as H<sub>2</sub>O, OH and SiO are found in large quantities C-rich objects like IRC 102+16, whereas M-type stars display the presence of HCN (Deguchi & Goldsmith, 1985), CS (Lindqvist et al., 1988), and CO<sub>2</sub> (Justtanont et al., 1998) in their envelope.

Consequently, the validity of TE is challenged and cannot hold throughout the entire envelope.

To explain the unexpected species mentioned above several scenarios have been proposed:

- The presence of icy comets releasing water in the vicinity of IRC102+16 (Melnick et al., 2001),
- The photo-dissociation of <sup>13</sup>CO in the intermediate envelope by the interstellar UV

field(the most abundant molecules  $^{12}\text{CO}$  and  $\text{H}_2$  are protected by self-shielding against interstellar UV photons) (Agundez et al., 2010)

- Non-equilibrium chemistry induced by pulsations releasing free carbon and oxygen from collisional dissociation of CO (Cherchneff, 2006), (Cherchneff, 2012), (Duari et al., 1999)

The most recent observations could rule out icy comets and photodissociation in the intermediate and the outer envelope as the loci of the unexpected species is within the inner envelope between  $1R_*$  and  $10R_*$  (Neufeld et al., 2011), (Decin et al., 2010a). TE is valid at and very close to the photosphere, where the average densities are above  $\sim 10^{10} \text{ cm}^{-3}$ , ensuring enough collisions between molecules / atoms. The situation is different when moving out to the intermediate and outer envelope. Close above the photosphere shocks heat up and accelerate the gas which do not (completely) thermalise before the next shock arrives. The unexpected high amount of molecular species like HCN,CS and  $\text{CO}_2$  is a result of non-equilibrium processes and cannot be explained by TE.

The regularity of the pulsations is another property, by means of AGB stars can be classified. In the case of regular, large amplitude and long period pulsations the AGB star is classified as Mira Variable. Less regular pulsators with smaller periods and amplitudes and higher temperatures belong to the group of semi-regular variables (SRVs) SRVs are comprise a quite numerous number of objects (Kerschbaum & Hron, 1992). Carbon-rich SRVs are generally even more abundant than C-rich Miras (Lebzelter et al., 1995). SRVs therefore represent a not negligible class of AGB stars. According to their temperatures, luminosities and densities SRVs are interpreted as evolutionary phase prior to the Mira phase. Not only the C/O ratio, but also pulsational properties, temperatures and densities thus change with temporal evolution along the AGB.

Another aspect concerns the pulsation mode of SRVs and Miras. Owing to their short pulsation periods SRVs are thought to oscillate in the first overtone mode. Observations of Mira variables in the LMC presume that Miras pulsate in the fundamental mode (Wood & Sebo, 1996). However, Feast (1996) provides evidence that both, Miras and SRVs, pulsate in their first overtone.

As they oscillate in radial direction only, fundamental mode pulsators are easier to describe than stars oscillating in overtone modes (and thus not only radially).

Dust is ubiquitous in the Universe and intimately linked to mass-loss processes in stars. Although dust only composes a small fraction of the total mass budget of a galaxy, dust grains are important ingredients of star formation and GCE, not least they drive the wind of AGB stars. The presence of dust within a few stellar radii above the photosphere of AGB stars can be inferred from Spectral Energy Distributions (SEDs) which show the characteristic features described above. Generally, dust-enshrouded AGB stars show an excess at IR and sub-mm wavelengths of the order of 90 % (Molster et al., 2010) relative to bare stars. The search for candidate dust carriers is bound to the following conditions:

- The dust grains are built up from abundant elements and molecules available from the gas phase.

- The dust species is refractory, i.e. able to resist/survive destructive processes like dissociation by collisions, photons from (inter-)stellar radiation, or thermal destruction by the passage of shocks.
- The opacity of the dust grains at visible and ultraviolet wavelengths, depending on size, shape, and composition, must be high enough to efficiently transfer momentum from stellar photons to the grains to overcome gravity

Dust grains form in dense and warm molecular gas layers in the inner wind. It is thus inevitable to accurately describe the molecular gas dynamics before considering dust formation. The prevalent chemical elements in the outflow of oxygen-rich AGB stars, i.e., silicon, magnesium, aluminum, iron, titanium, and their corresponding oxides are considered as candidates of dust grains. Each cluster species, structure and size is related to a fingerprint in the observed IR spectrum of the star. The modelling and the reproduction of gas phase species in the *inner* envelope is crucial for our understanding of dust formation. Dust grains form from molecules in the gas phase within a few  $R_*$ . It is thus 'parent'<sup>1</sup> species are injected to the interstellar medium from this confined region.

Most elements are less abundant in the ISM than in stars, thus indicating elemental depletion by condensation into solids (Jenkins, 2009). Evidence for dust is not only proved by elemental depletion and radiation absorption, but also proved by IR and sub-mm emission. Dust grains absorb or scatter UV photons, distribute the energy among the various degrees of freedom and emit radiation at longer wavelengths. Composition, shape and size of the grain strongly affects the broad dust features in the infrared spectrum. In the case of silicates, emission features around  $9.7 \mu\text{m}$  and  $18 \mu\text{m}$  are present, characteristic for Si-O stretching mode and the O-Si-O bending, respectively. Posch et al. (1999) discussed the origin of  $13 \mu\text{m}$  emission seen in oxygen-rich AGBs and concluded that  $\text{MgAl}_2\text{O}_4$  (spinel) is the most probable carrier. However, this has been questioned by Sloan et al. (2003), who find a strong correlation of this dust feature with warm  $\text{CO}_2$  and attribute it to crystalline alumina (Little-Marenin & Little, 1990). The  $30 \mu\text{m}$  feature seen in C-rich objects and attributed to MgS (Hony et al., 2002) has not been observed in M-type AGB stars. Furthermore, hydrocarbons with a C-H emission feature at  $3.4 \mu\text{m}$ , and silicon carbon (SiC) grains with a signature at  $11.3 \mu\text{m}$ , are also not seen in oxygen-rich objects.

In order to assess the amount and composition of dust returned to the ISM, several efforts have been undertaken (Ferrarotti & Gail, 2006), (Boyer et al., 2012). These studies address the AGB dust contribution in the local and the red-shifted universe and questioned the primacy of AGB stars as dust providers at subsolar metallicity. In how far supernovae provide the dust production in the Milky Way and galaxies of lower metallicity is a matter

---

<sup>1</sup>Parent species are molecules from the stellar atmosphere that have not been incorporated into dust, daughter species, however, result from photochemical processing of the parent species in the intermediate envelope

of debate (see e.g. Dwek & Cherchneff 2011, Zhukovska & Henning 2014).

Ferrarotti & Gail (2006) evaluated the dust return from AGB stars as a function of stellar mass and metallicity. The authors distinguish between several dust types (silicate, iron and SiC grains), according to the chemical type of AGB stars (M-type, S-type and C-type). This study presumes preexisting seed nuclei without describing the gas phase and may be too oversimplifying. However, it may constrain the dust condensation degree which is determined by the abundance of key elements (i.e. the least abundant element required to form a dust species).

In carbon-rich stars, the dust formation is relatively well understood. Duley (1985) found a plausible dust condensate: Amorphous carbon (AMC). It is stable and refractory, abundant in carbon-rich AGB stars and additionally very opaque in the near-infrared (NIR) and the optical wavelength domain. It has been shown that the presence of AMC can supply enough radiation pressure to drive the wind (Winters et al., 2000). AMC is formed by clusters of Polycyclic Aromatic Hydrocarbons (PAHs). Chemical models successfully describe the PAH formation in acetylenic flames and circumstellar environments (Frenklach & Feigelson, 1989). Further investigations revealed that PAH cluster formation is only efficient in a narrow temperature range of 900 - 1100 K (Cherchneff et al., 1992), (Cau, 2002)). In these model the temperature window is periodically crossed owing to pulsations, thereby largely increasing the timescale for PAH formation.

The situation is different in oxygen-rich AGB winds. Several wind-driving condensates have been proposed: alumina ( $\text{Al}_2\text{O}_3$ ) (Onaka et al., 1989), solid iron (Fe) (Gail & Sedlmayr, 1999),  $\text{TiO}_2$  (Gail & Sedlmayr, 1998), silica ( $\text{SiO}_2$ ) (Speck, 1998), magnesium rich silicates (enstatite ( $\text{MgSiO}_3$ ), forsterite ( $\text{Mg}_2\text{SiO}_4$ )), iron-rich silicates (ferrosilite ( $\text{FeSiO}_3$ ), fayalite ( $\text{Fe}_2\text{SiO}_4$ ), and mixtures of magnesium and iron silicates (Hackwell et al., 1970), (Gail & Sedlmayr, 1999). These condensates can be abundant and thermally stable. However, most of the condensates are too transparent in the optical and NIR regime ( $\text{SiO}_2$ ,  $\text{TiO}_2$ ,  $\text{Al}_2\text{O}_3$  and  $\text{Mg}_2\text{SiO}_4$ ) (Woitke, 2006), or they are too opaque, absorb too much radiation and heat up to a point beyond their stability (pure Fe silicates and Mg-Fe silicates). Instead of absorbing stellar radiation, the grains may also scatter the photons. Based on radiation-hydrodynamical models, Höfner (2008) demonstrated that the winds of M-type stars can be driven by micron-sized Fe-free silicate grains, if scattering is considered. Despite of its low absorption cross section, these Mg-end member silicates have a considerable scattering cross section.

Alumina grains can condense below  $T = 1500$  K (Onaka et al., 1989) and have been observed at distances as small as  $1.5R_*$  (Verhoelst et al., 2006) and  $2.1R_*$  (Karovicova et al., 2013). Despite the observational evidence for alumina dust close to the star and its refractory nature, it cannot explain the wind driving in high mass-loss objects. In low mass-loss AGB stars, however, alumina dust shells suffice to drive the observed mass-loss.  $\text{TiO}_2$  has similar properties to alumina, but its abundance is too low. However,  $\text{TiO}_2$  may act as a seed nuclei and other condensates could grow on its surface (Jeong et al., 2003).

Another important characteristic of dust concerns the problem, whether dust exists in crystalline or amorphous form. Crystalline dust shows relatively sharp spectral signatures, whereas a spectra with amorphous dust is broad and smeared out. Therefore, these two forms can be distinguished spectroscopically. Observations of evolved oxygen-rich AGB stars revealed that only star with a significant mass-loss show signatures of crystalline silicate dust (Waters et al., 1996). It was concluded that a dense wind is required to form crystalline silicates and that stars with low mass-loss rates lack silicates in crystalline form in their dust shells. Kemper et al. (2001) questioned above conclusion and proposed that in stars with low mass-loss rates crystalline signatures could indeed be present, but blended by other wind components. Molster et al. (1999) suggested that the apparent absence of crystalline silicates in most of evolved stars is a temperature effect. Owing to their structure, crystalline grains have temperatures lower than 1000 K (lower than its amorphous form) resulting in a negligible spectral features for wavelengths shorter than 20 microns. Higher temperatures destroy the crystal structure and result in amorphous silicates. Moreover, Molster et al. (1999) showed that crystalline silicates consist at least partially of pure Mg-end members, namely enstatite and forsterite. On Earth amorphous structures can be synthesised by melting a crystalline substance with a subsequent fast cooling.

In order to identify dust components with their spectral signatures, the knowledge of optical constants is required. Optical constants comprise the refractive index  $n$ , absorption coefficient  $A_{ij}$  (Einstein coefficient), and the reflectivity  $R$  and can be found in tabulated form (see e.g. Palik 1991). Optical constants depend not only on the composition of the material, but also on the shape and the size of the dust grain. For the sake of simplicity often spherical grains are presumed. However, it is improbable that clusters coalesce spherically and stardust found in meteoric inclusions is not spherical. Furthermore, the wavelength of the radiation interacting with dust grain is crucial to the optical constants. In general, the rule of equal dimensions applies. Micron-sized dust grains also interact with photons in the micron range. Radiative transfer models of circumstellar envelopes conduce to generate synthetic spectra by presuming a grain composition (grain opacity) and size distributions (GSD) (see e.g. Höfner et al. 2003). Conversely, by fitting the synthetic spectra to observations the most realistic GSDs can be ascertained. A distinction between grey (wavelength-independent) and non-grey (wavelength-dependent) models is made, whereas the non-grey models are certainly more realistic. A consequence of the radiation hydrodynamic models of Höfner et al. (2003) and Höfner (2008) is the thermal decoupling of dust grains and gas phase molecules. As a consequence, dust grains have different temperatures than gas components. Gas phase molecules may cool more efficiently than dust grains, if radiative equilibrium of the gas is assumed. Once excited, a molecule can relax easily by the emission of IR radiation to its ground state. Dust grains, however, have a more complex structure and the excitation energy cannot easily be irradiated, but is distributed among various degrees of freedom in the grain. This implies that dust grains are hotter than the gas.

In this thesis, a chemical network is built up, involving prevalent 'parent' species formed in the inner wind, unexpected non-equilibrium gas-phase molecules, and dust clusters, and implemented in a stellar pulsation model. Simultaneously, this model describes the amount, composition and sizes of the dust grains that drive the stellar wind. The main goal of this work is thus to qualitatively and quantitatively account for the molecules, clusters and dust grains.

This thesis is organised as follows: Section 2 presents the modelled stars and its parameters. Section 3 describes the physics of the shock model and its parameters (i.e. the pulsation model), the underlying chemistry and the related chemical network is described in Section 4. In Section 5 model results for the galactic Mira variable star IK Tau are presented and compared to observations. Results for the semi-regular models are shown in Section 6, for S-type AGB stars in Section 7, and for AGB stars at subsolar metallicity in Section 8, respectively. Finally, in Section 9 the main outcomes are discussed and this thesis is summarised.



## 2 AGB Stars

### 2.1 Evolution of Low- and Intermediate Mass Stars

The birthplaces of stars are found in molecular clouds where the conditions for star formation are met. When a molecular core starts to collapse due to self-gravity, pressure and temperature increase. Eventually, the star becomes dense and hot enough to ignite hydrogen in its central region and the collapse is halted. A new star is born and it resides on the zero-age main sequence (ZAMS). Stars spend most of their lifetime on the main sequence quiescently burning hydrogen in their cores. In low and intermediate mass stars ( $M = 0.1 - 8 M_{\odot}$ ), this phase lasts about  $10^9 - 10^{10}$  years, which is longer than in high mass stars ( $M > 8 M_{\odot}$ ). High mass stars are more wasteful as they burn their hydrogen at a faster rate owing to higher central temperatures and densities, compared to low- and intermediate mass stars. Once the hydrogen in the central core is exhausted, the hydrogen continues to burn in a shell surrounding the core (see e.g. Iben & Renzini 1983, Herwig 2005). As the core has ceased to burn it is not anymore in hydrostatic equilibrium, contracts and heats. As a consequence the outer layers of the star expand and cool which increases significantly the luminosity of the star (see Figure 1). This stage is known as the red giant branch (RGB). The core contraction is halted either by electron degeneracy pressure in the case of low mass stars, or by the onset of core He burning in the case of intermediate mass stars. He burning is extremely density and temperature dependent as it involves three He nuclei (i.e.  $\alpha$  particles). He burning occurs in explosive events (so called He-flashes) due to the  $3\alpha$  reaction (rate). In low mass stars, these flashes happen in the degenerate core in the form of a runaway process leading to a structural readjustment of the star, which resides now on the Horizontal branch (HB). In intermediate mass stars, He burns non-degenerately in the core and flashes occur in a shell surrounding the core. As a result, low- and intermediate mass stars consist of an inert carbon-oxygen core, surrounded by H- and He-burning shells and a large convective envelope. This state is commonly referred to as asymptotic giant branch (AGB) phase. The recurrent, explosive ignition of the He-shell leads to a sudden increase in luminosity and subsequent mixing events (dredge-ups). This evolutionary stage is commonly referred to as thermally-pulsating AGB phase (TP-AGB phase). This phase lasts about  $10^6$  years = 1 My during which the mass-loss increases and chemical composition of the envelope alters. The AGB life is terminated at the tip of the AGB. At the AGB tip mass-loss rates have risen to such a high value that this essentially removes hydrogen-rich envelope.

### 2.2 Mira Stars

#### IK Tau

Mira stars are a class of pulsating variable AGB stars with pulsation periods of the order of hundreds days and amplitudes greater than one magnitude in the IR regime and greater than 2.5 magnitudes at visual wavelengths. The name Mira goes back to the star Mira (o

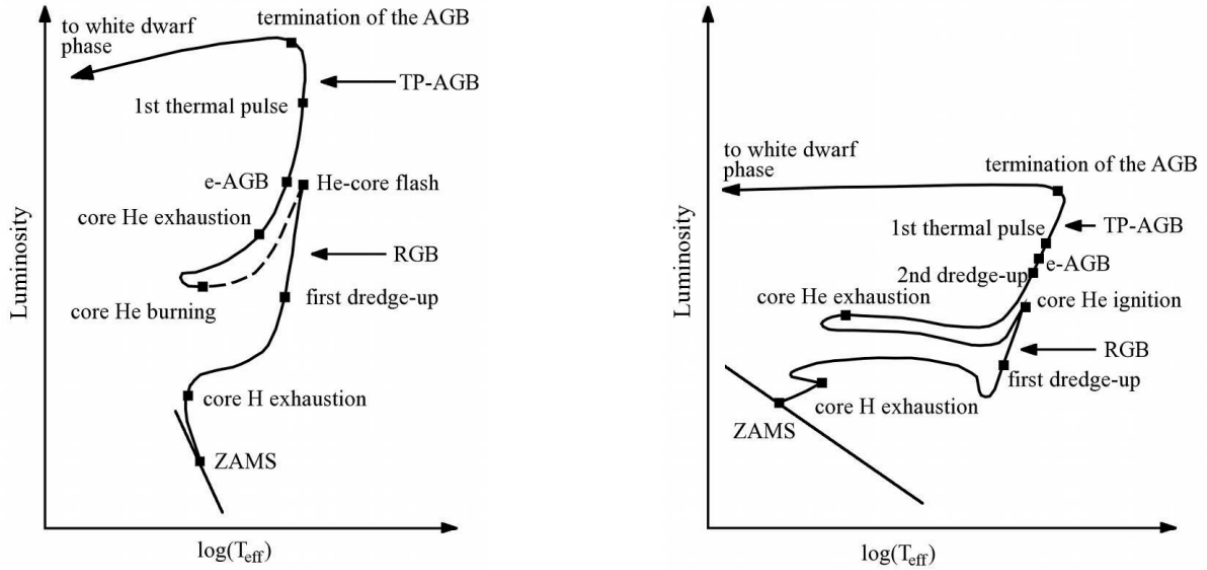


Figure 2: Evolutionary tracks of a star in the Hertzsprung-Russell-diagram. Left: A low mass ( $1 M_{\odot}$ ) star evolving off the main sequence. Right: an intermediate mass ( $5 M_{\odot}$ ) star (Maercker, 2009)

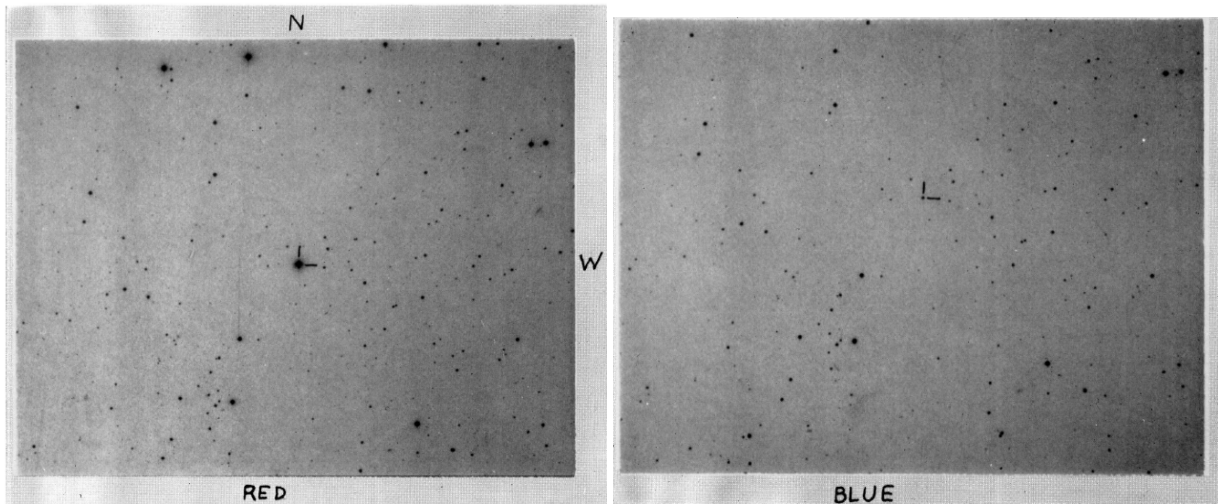


Figure 3: Red and blue colour map of IK Tau made in the year of its discovery (Neugebauer et al., 1965)

ceti) which is not visible to the naked eye for a part of its cycle and then suddenly increases its luminosity (*by miracle*). In the following, two extensively modelled Mira variable stars are described in more detail. IK Tau is a galactic Mira variable star discovered in 1965 (Neugebauer et al., 1965). It is located 250 - 265 pc from our Sun (Olofsson et al., 1998), (Hale et al., 1997) and has a spectral type ranging from M8.1 to M11.2 (Decin et al., 2010a), which renders IK Tau extremely red. The discoverers already concluded that IK Tau is intrinsically extremely red despite the contribution of interstellar reddening.

Due to its proximity and high mass-loss rate, IK Tau is one of the best studied AGB stars in terms of molecular lines. In Table 1, values for IK Tau's stellar parameters from most recent observations are listed. They comprise temperature, radius, pulsation period,

stellar mass, density, C/O ratio, mass-loss, shock radius and velocity as well as mass-loss and dust-to-gas mass ratio. The effective temperature  $T_*$  can be obtained by the blackbody spectrum of the star by the use of Planck's law. Planck's law unambiguously assigns an electromagnetic spectrum (i.e. the blackbody spectrum) to a finite temperature and vice versa:

$$B_\lambda(\lambda, T) = \frac{2hc^2}{\lambda^5} \left( e^{\frac{hc}{\lambda kT}} - 1 \right)^{-1} \quad (1)$$

where  $B_\lambda$  is the spectral radiance of a body,  $\lambda$  the wavelength,  $T$  the absolute temperature,  $k$  the Boltzmann constant,  $h$  the Planck constant, and  $c$  the speed of light, respectively.

The most recent determination of IK Tau's effective temperature resulted in  $T_* = 2200$  K (Decin et al., 2010a). This temperature provides the best fit to observations in a model grid with  $T_*$  ranging from 2000 - 3000 K. This value is in agreement with the value ( $T_* = 2100$  K) used by Duari et al. (1999) and  $T_* = 2000$  derived by Le Sidaner & Le Bertre (1996). The pulsation period can be determined by long-time observations over several years. Photometric observations of the  $1 \mu\text{m}$  band resulted in a pulsation period of 470 days (Wing & Lockwood, 1973), (Hale et al., 1997). The shock velocity can be deduced and estimated by the pulsation and velocity amplitudes. Hinkle et al. (1997) find a typical velocity amplitude of 20-30  $\text{km s}^{-1}$  for Mira variables. For IK Tau, the authors report a visual amplitude of 4.6 a large velocity amplitude approaching 30  $\text{km s}^{-1}$ . The model shock velocities of 25  $\text{kms}^{-1}$  and 32  $\text{kms}^{-1}$  are thus consistent with observations.

The radius of IK Tau can be determined by exploiting the period-luminosity relation for Miras (Duari et al., 1999). The adopted value here is  $2.5 \times 10^{13}$  cm, derived by a fit of a stagger model grid to molecular observations (Decin et al., 2010a). Stellar mass  $M_*$ , photospheric density  $n_0$ , C/O ratio and shock radius  $r_s$  cannot be accessed directly from observations. The choice of these latter model parameters is therefore based on theoretical considerations discussed in Section 3. Expansion velocities and the correlated mass-loss rates can be extracted from Doppler shifts of molecular line transitions (see e.g. Decin et al. 2010a). These values (except mass-loss and dust-to-gas mass ratio) are used as input parameters for the modelling used in this thesis.

## TX Cam

TX Camelopardalis (TX Cam) is another galactic Mira variable star with similar properties to IK Tau. Its pulsation period is larger ( $\sim 558$  days). Its visual magnitude variation of  $m_v = 4.6$  and its spectral type (M8-M10) are almost identical to IK Tau. TX Cam's mass-loss rate, however, is with  $\dot{M} = (1.1 - 3) \times 10^{-6} M_{\odot}$  about one order of magnitude lower than in IK Tau (Knapp & Morris, 1985), (Ramstedt et al., 2008). The distance to TX Cam was estimated to be 390 pc from the period- luminosity relation (Olivier et al., 2001).

The investigation of TX Cam is performed to probe the inner wind conditions of o-rich Mira's and test the applied chemical network. The model parameters of TX Cam are based on the values provided by Cherchneff (2006), except for the stellar mass ( $1 M_{\odot}$  instead of  $0.65 M_{\odot}$ ) and the shock velocity (32  $\text{km s}^{-1}$  instead of 25  $\text{km s}^{-1}$ ). These parameter were

Table 1: Stellar parameters used for modelling IK Tau

Parameter	Value	Reference
$T_*$	2200 K	Decin et al. (2010a)
$M_*$	1 - 1.2 $M_\odot$	Duari et al. (1999)
$R_*$	$2.5 \times 10^{13}$ cm	Decin et al. (2010a)
$v_s$	25 - 32 $\text{kms}^{-1}$	Hinkle et al. (1997)
$P$	470 days	Hale et al. (1997)
$n(1R_*)$	$3.6 \times 10^{14}$ $\text{cm}^{-3}$	
$r_s$	1 $R_*$	Duari et al. (1999)
$C/O$	0.75	Duari et al. (1999)
$\dot{M}$	$(0.4 - 3) \times 10^{-5}$ $M_\odot/\text{yr}$	Decin et al. (2010a)
$\Psi$	$1.9 \times 10^{-2}$	Decin et al. (2010a)

Table 2: Stellar parameters used for modelling TX Cam

Parameter	Value	Reference
$T_*$	2600 K	Olofsson et al. (1991)
$M_*$	1 $M_\odot$	Cherchneff (2006)
$R_*$	$1.95 \times 10^{13}$ cm	Olofsson et al. (1991)
$v_s$	25 - 32 $\text{kms}^{-1}$	Cherchneff (2006)
$P$	557 days	Olofsson et al. (1991)
$n(1R_*)$	$3.6 \times 10^{14}$ $\text{cm}^{-3}$	
$r_s$	1 $R_*$	Cherchneff (2006)
$C/O$	0.75	Cherchneff (2006)
$\dot{M}$	$(1.1 - 3) \times 10^{-6}$ $M_\odot/\text{yr}$	Ramstedt et al. (2008)
$\Psi$	$4 \times 10^{-3}$	Ramstedt et al. (2008)

adjusted to compare the results to the IK Tau case. Consequently, differences may arise owing to the timescale (pulsation period), gas temperature and number densities (scale heights). SiO and H<sub>2</sub>O masers have been detected (Diamond & Kemball, 1998),(Cho et al., 2014) suggesting that TX Cam is an oxygen-rich object.

### 2.3 Semi-Regular Variables (SRVs)

SRV's experience smaller amplitude pulsations in the visual magnitude ( $M_v < 2.5$  mag) according to the classification in the General Catalogue of Variable Stars (GCVS) (Samus et al., 1997). They are further divided in the subclasses SRb, SRa, SRc, SRd, and Lb, on the basis of the pulsation regularity. SRa stars exhibit persistent periodicity, usually small ( $< 2.5$  mag in the visual) light amplitudes, and periods of 35 - 1200 days. SRb stars have a poorly defined periodicity (with mean cycles in the range of 20 to 2300 days). Such stars may experience the simultaneous presence of two or more periods and irregular intervals. This thesis focuses on SRVs of type SRa and SRb. The question whether trends in AGB properties like pulsation period, stellar mass and mass-loss, temperature, scale heights and densities can be attributed to the subclasses SRb and SRa was the scope of several investiga-

tions (Kerschbaum & Hron, 1992), (Lebzelter et al., 1995). Their results revealed surprising facts: The subclass SRa is not a distinct class of SRVs, but a mixture of intrinsic Miras and SRb semi-regular variables. The subclass SRb, however, forms a distinct group in terms of periods, amplitudes and temperatures, at least in the oxygen-rich case. The SRb variables are further separated in a *blue* group with periods smaller than 150 days and effective temperatures above 3200 K, and in a *red* group with Mira-like properties (similar mass-loss, temperature, scale heights and densities), but with roughly half of the period. The SRVs of the blue subgroup are twice as numerous as those in the red subgroup in the galactic sample of Kerschbaum & Hron (1992). On the basis of temperatures, densities and luminosities the authors assigned the blue SRVs to the early, non-thermally pulsing AGB (eAGB). The red group, on the other hand, is believed to be a phase preceding the Mira phase with equal residing time in both phases of stellar life. Moreover, the oxygen-rich SRVs assigned to the blue group can be described by a blackbody with only one temperature. The red SRV's and Miras need two blackbodies to be reasonably well approximated (Kerschbaum & Hron, 1996). The effective blackbody temperatures correspond to the photospheric temperature  $T_{eff}$  or  $T_*$ , and the dust temperature  $T_d$ . In addition to these physically meaningful fit parameters the authors derive a size of the circumstellar dust shell defined as  $r = R_d/R_*$ , where  $R_d$  (and also  $T_d$ ) correspond to a region (temperature) in the innermost part of the shell. The majority of the observed galactic SRVs have weaker CO line compared to their Mira counterparts, i.e. they are low mass-loss objects ( $\dot{M} < 10^{-7} M_\odot/\text{yr}$ ) and have small expansion velocities (Kerschbaum et al., 1996). The authors found no correlation or a weak correlation between effective temperature, expansion velocity and pulsation period.

In conclusion:

- SRVs are the precursors of the MIRA TP-AGB stars.
- SRVs are consists of a blue and a red group rather than SRb and SRa since SRas do not form a distinct class
- The blue SRVs correspond to the e-AGB phase where no (or hardly any) dust grains have formed
- The red SRVs are the preceding phase of Miras having similar properties, but a shorter pulsation period

The choice of the model parameters is based on the stellar properties of L<sup>2</sup> Puppis and W Hydra (WHya), two SRVs of type SRb and SRa, respectively. It should be noted that L<sup>2</sup> Puppis is considered as an extreme case with a low expansion velocity  $v_{exp}=2 \text{ km s}^{-1}$ . Both stars are considered SRVs which pulsate in the first overtone (Kerschbaum et al., 1996) or in the fundamental mode (Lebzelter et al., 2005), but their pulsation is not as powerful as for Miras since the amplitudes are smaller. Nonetheless, carbon-rich SRV's seem to be more affected by variations in the pulsation behaviour (Kerschbaum & Hron, 1992). Originally, the model has been designed for fundamental-mode pulsating Mira variables (Duari et al., 1999), (Cherchneff, 2006), (Cherchneff, 2012). Owing to the reasons listed above, it is reasonable to extend the pulsation model to oxygen-rich SRVs.

Table 3: Stellar parameters of semi-regular variables of class SRb.

Source	P(d) <sup>a</sup>	T <sub>*</sub> (K) <sup>b</sup>	v <sub>e</sub> (km s <sup>-1</sup> ) <sup>d1</sup>	R(R <sub>⊙</sub> ) <sup>c</sup>	M(M <sub>⊙</sub> ) <sup>c3</sup>	$\dot{M}$ (M <sub>⊙</sub> /yr) <sup>d</sup>
L <sup>2</sup> Pup	141	2690-3380	1.9-2.3	126	1.7	(2.2-20)(-9)
R Dor	338	2090-3058	6.2	208-370	1.2-1.5	(1.0-1.3)(-7)
W Cyg	131	2670	7.6-8.3			1.0(-7)
SS Cep	90	2580-3220	10.0-12.9	237	2.4	6.0(-7)
X Her	95	2490-3161	2.2-6.5	214	1.9	(0.4-1.5)(-7)
θ Aps	119	2620-3210	4.5-5.9	196	1.9	(0.4 -1.1)(-7)
UY Cet	440	2400	6.0-10.1			2.5(-7)
UX And	400	2240	12.8-13.0			4.0(-7)
R Crt	160	2130	10.6			8.0(-7)
U Del	110-120	2720	7.5-10.8			1.5(-7)
AH Dra	158	2680	6.4			8.0(-8)
S Dra	136	2230	8.8-9.6			4.0(-7)
UU Dra	120	2260	8.0-10.5			5.0(-7)
g Her	89	2700-3339	8.4	215	2.7	1.0(-7)
AK Hya	75	2430	4.6-4.8			1.0(-7)
RX Lep	60	2660-3339	3.5	186	2.3	5.0(-8)
T Mic	347	2430	4.8			8.0(-8)
SV Peg	145	2330	7.5-10.6			3.0(-7)
TW Peg	929	2690	9.5-9.8			2.5(-7)
V PsA	148	2360	14.4-15.6			3.0(-7)
τ <sup>4</sup> Ser	100	2500-3331	14.4	146	1.8	1.5(-7)
SU Sgr	60	2090	9.5			4.0(-7)
UX Sgr	100	2520	9.5			1.5(-7)
V Tel	125	2260	6.8			2.0(-7)
Y UMa	168	2230	4.8-6.1			1.5(-7)
SU Vel	150	2380	5.5-6.4			2.0(-7)
BK Vir	150	2210	4.0			1.5(-7)
RT Vir	155	2110-3034	7.8	127	0.7	5.0(-7)
SW Vir	150	2190-3051	7.1-7.5	248	1.8	4.0(-7)
V744 Cen	90	3415	6.5	169	2.4	
V806 Cen	12	3508		86	1.3	

<sup>a</sup>Values are taken from Kerschbaum et al. (1996) and Olofsson et al. (2002)

<sup>b</sup>Values are taken from Olofsson et al. (2002) and Dumm & Schild (1998)

<sup>c</sup>Values are taken from Dumm & Schild (1998)

<sup>d</sup>Values are taken from Olofsson et al. (2002)

SRb variable stars have generally higher photospheric temperatures, higher stellar masses and smaller radii than their SRa and Mira counterparts, as can be seen in Table 2.3. Their relative compactness and their hotness implies a short scale height and thus a sharp decrease in the number density with increasing distance from the star. As a consequence, molecu-

lar  $H_2$  is quickly converted into atomic H (see Section 6). In addition, the dust formation is strongly hampered, not only due to low densities, but also owing to the short pulsation period which prevents the cluster to grow and to condense.

## 2.4 S-type AGB Stars

S-type AGB stars are believed to be a brief transitional phase of AGB stars. In low mass AGB stars the C/O ratio is increasing owing to dredge-up events. Having a C/O ratio close to unity (within approximately 5 %), S-type AGB stars may be identified with a transitional phase between oxygen-rich and carbon-rich AGB phase (see e.g. Ramstedt et al. 2009). The spectral sequence the star experiences is thus: M-MS-S-SC-C. In this thesis particularly M, MS and S-type AGB stars are investigated, as the chemical network used here pertains to an oxygen-rich environment. S-type AGB stars show spectral emission features of ZrO (and also LaO and TiO) indicating an ongoing s-process nucleosynthesis.

Dust formation in S-type AGB stars is challenging. Although moderate dust-to-gas mass ratios ( $2 \times 10^{-4}$  -  $5 \times 10^{-4}$ ) and mass-loss rates are observed (see Table 4) in S-type stars, the dust composition is ambiguous. Carbon and oxygen are almost entirely locked in CO leaving hardly to form carbon-dust (AMC, PAHs) or oxygen-rich dust (silicates, metal oxides). Metallic iron has been proposed to account for the observed dust mass and mass-loss (Ferrarotti & Gail, 2006). Since the C/O ratio of S-type is not exactly 1 (but ranges from 0.90 to 1.05), and carbon and oxygen can be released in shocks under non-equilibrium conditions, the formation of carbonaceous and oxygen-bearing dust cannot be excluded in S-type AGBs. Indeed, Ramstedt et al. (2009) assumed either amorphous carbon grains or amorphous silicates for S-type AGB stars based on the IRAS low resolution spectra (LRS) classification.

## 2.5 Stars in the Magellanic Clouds

The Magellanic clouds consist of two dwarf galaxies named Large Magellanic Cloud (LMC) and Small Magellanic Cloud (SMC) which are situated in the vicinity of the Milky Way. The distance to the LMC is 50 kpc (Pietrzyński et al., 2013) and to the SMC 61 kpc (Hilditch et al., 2005), respectively. Owing to these known distances, single sources can be resolved including the determination of the luminosity, effective temperature, and mass-loss (see e.g. Seale et al. 2014 and references therein).

Compared to the Milky Way, the MCs have a lower metal content and harbour older population of stars (see e.g. Cioni et al. 2014). The metal content can thus be interpreted as an age indicator. A quantity describing the metal content of stellar population is the *metallicity*  $Z$ . It measures the mass fraction of elements heavier than He ( $A > 4$ ) in relation to the total mass of elements. The Milky Way has a metallicity of  $Z = Z_{\odot} = 0.014$  (i.e. the solar metallicity). In the LMC, the metallicity is roughly one half of the solar value ( $Z_{LMC} \approx Z_{\odot}/2$ ) In the SMC, the metallicity is approximately one fifth of the solar value ( $Z_{SMC} \approx$

Table 4: Stellar parameters (Pulsation period, effective temperature, terminal velocity, stellar radius, stellar mass, dust-to-gas mass ratio) of S-type AGB stars. The values are compiled from tables of Ramstedt et al. (2009). For the object W Aqu also data from Danilovich et al. (2014) is listed. For the object W Aqu also data from Justtanont et al. (2010) is listed. The notation  $X(Y) \equiv X \times 10^Y$  is used.

Source	P(d)	$T_*$ (K)	$v_e$ (km s $^{-1}$ )	R( $R_\odot$ )	$\dot{M}$ ( $M_\odot$ /yr)	$\Psi$ (dust/gas mass)
Mira variability type						
R And	409	1800	8.3	805	6.6(-7)	6.0(-4)
W And	397	2400	6.0	445	1.7(-7)	
W Aqu	490	1800-2300	16.5-17.2	862	(2.2-4.0)(-6)	(1.1-5.0)(-3)
S Cas	611	1800	20.5	934	3.5(-6)	6.0(-4)
WY Cas	477	2200	13.5	575	1.1(-6)	
TT Cen	462	2400	20.0	474	2.5(-6)	
R Cyg	426	2200	9.0	546	6.3(-7)	
$\chi$ Cyg	407	2400-2600	8.5	445	(3.8-7.0)(-7)	2.0(-4)
S Lyr	438	1800	13.0	819	2.0(-6)	1.2(-3)
RT Sco	449	2400	11.0	474	4.5(-7)	
ST Sgr	395	2400	6.0	445	2.0(-7)	
Ø	451	2170	12.1	620	1.3(-6)	1.1(-3)
Semi-regular variability type						
Z Ant	104	2400	6.0	230	9.0(-8)	
V386 Cep		1800	16.0	661	2.0(-6)	1.9(-2)
DY Gem		2400	8.0	374	7.0(-7)	
ST Her	148	2200	8.5	445	1.3(-7)	4.4(-3)
RX Lac	174	2400	6.5	374	8.0(-8)	
ST Sco	195	2400	5.5	374	1.5(-7)	
Ø	155	2270	8.4	410	5.3(-7)	1.2(-2)



$Z_{\odot}/5$ )

In order to relate metallicities with dust-to-gas mass ratios, an empirical scaling of luminosity, mass-loss rate and dust-to-gas mass ratio according to the color magnitudes is used (Groenewegen, 2006). The dust-to-gas mass ratio  $\Psi$  scales with

$$\Psi = \Psi_{\odot} \times 10^{[Fe/H]} = 5 \times 10^{-3} \times 10^{\log(\frac{ZX_{\odot}}{Z_{\odot}X})} \quad (2)$$

where  $\Psi_{\odot}=0.005$  is the solar dust-to-gas mass ratio,  $X$  the mass fraction of hydrogen,  $Y$  the mass fraction of helium, and  $[Fe/H] \simeq \log(\frac{ZX_{\odot}}{Z_{\odot}X})$  (Boyer et al., 2011).

In the LMC, the metallicity is  $Z=0.008$ , which results in a dust-to-gas mass ratio  $\Psi_{LMC}=2.8 \times 10^{-3}$ . In the SMC, the metallicity is  $Z=0.003$ , which results in a dust-to-gas mass ratio  $\Psi_{SMC}=1.0 \times 10^{-3}$ .

However, it should be noted that  $\Psi$  is uncertain and may not be the same for C-rich and O-rich AGB stars. Nevertheless, the above values are consistent with Boyer et al. (2012), who derived a median dust mass-loss rate of  $\langle \dot{D} \rangle_{SMC}=2.8 \times 10^{-11} \text{ M}_{\odot}/\text{yr}$  for the SMC and  $\langle \dot{D} \rangle_{LMC}=7.1 \times 10^{-11} \text{ M}_{\odot}/\text{yr}$  for the LMC. Combining the dust mass-loss rates with the dust-to-gas mass ratios rate eventually leads to a median mass-loss rate of  $\langle \dot{M} \rangle_{SMC}=2.8 \times 10^{-8} \text{ M}_{\odot}/\text{yr}$  and  $\langle \dot{M} \rangle_{LMC}=7.1 \times 10^{-8} \text{ M}_{\odot}/\text{yr}$  for typical O-rich AGB stars in the SMC and LMC, respectively. These mass-loss rate derivation are based on a large sample of O-rich AGB stars (1851 in the SMC and 8871 in the LMC), which provides a valuable set of stars. Jones et al. (2014) find mass-loss rates in the range of  $\dot{M}_{LMC}=(8.0 \times 10^{-8} - 5.0 \times 10^{-6}) \text{ M}_{\odot}/\text{yr}$  for oxygen-rich AGB stars in the LMC from fitting their models to observations. A grain mixture primary composed of amorphous silicates with contributions from amorphous alumina and metallic iron fits the observed spectra well. Gullieuszik et al. (2012) found no significant mass-losing oxygen-rich source in a sample of 374 AGB stars in the LMC, a result that indicates the dust in the LMC is carbon-rich. Despite their small number, extreme carbon stars ( $x$ -AGB) dominate the dust return in both, the LMC and the SMC (Boyer et al., 2011), (Boyer et al., 2012). From a theoretical point of view, it is clear that the available elements Si, Mg and Al are less abundant in the MCs than in the Milky Way. Consequently, the formation of dust clusters necessary for silicate and alumina formation is less efficient. The question, whether the dust formation rate simply scales with the amount of available elements, and whether low metallicity elemental compositions have further consequences for dust formation. The metallicity in the dwarf galaxies LMC and SMC is not a constant value, but decreases from the galaxy center to the outer regions (Cioni, 2009). This result clearly indicates an AGB population of various masses and evolutionary stages in the MCs. In conclusion, the oxygen-rich AGB stars in the MCs are losing mass at a considerably lower rate in comparison to the Milky Way, but with similar dust grain compositions that include silicates and alumina.

## 3 Physical Model

### 3.1 Structure of the Envelope

Mira variable stars typically vary by 5 orders of visual magnitude during a period of about a year, but they vary much less in their bolometric luminosity, which is dominated by IR radiation. These observations indicate a periodic excitation mechanism acting predominantly in the visual range. The visual absorption lines show little velocity variation (Joy, 1954) thus indicating a rather stationary envelope, although mass-loss rates of  $10^{-6} - 10^{-5} M_{\odot}/\text{yr}$  and high amounts of dust are observed. These observations may seem contradictory at first, but can be interpreted as periodic shock waves travelling through the atmosphere of Mira variables.

The model used in this thesis is the pulsation model. This simple semi-analytical model of the inner wind has been developed by Cherchneff et al. (1992) and Willacy & Cherchneff (1998). The physics of the periodic shock waves are modelled in two stages based on the formalisms of Fox & Wood (1985) and Bertschinger & Chevalier (1985):

- a thin shock layer immediately behind the shock front
- an expansion layer in the post shock gas

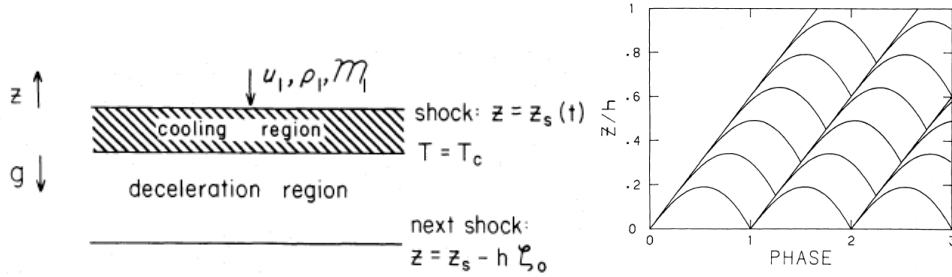


Figure 4: *Left*: The structure between two shocks in the Lagrangian frame (Bertschinger & Chevalier, 1985): The preshock gas ( $u_1, \rho_1, M_1$ ) enters the shock front and the thin internal relaxation layer until the gas has cooled to temperature  $T_c$ . After that, the gas adiabatically expands until the next shock arrives. *Right*: The straight lines correspond to the shocks travelling outwards in time, whereas the oscillations display the trajectories of the post-shock fluid elements

Moreover, the model has been used by Duari et al. (1999) for the study of the oxygen-rich Mira IK Tau, and by Cau (2002), Cherchneff (2011), Cherchneff (2012) to study IRC+10216.

Finally, Cherchneff (2006) studied the effect of C/O variation on the AGB by modelling a stellar surrogate similar to TX Cam. The study was also based on this pulsation-induced shock model.

This thesis extends the work of Duari et al. (1999) by

- increasing the computational domain from  $2.2 R_*$  to  $10 R_*$ .
- using updated stellar parameters from the most recent observations.
- introducing clusters and dust grains which are coupled to the gas phase.

In the plane-parallel limit (PPL), analytical solutions can be found for the post-shock expansion layer (Bertschinger & Chevalier, 1985), hereafter BC85. The analytical solution to the hydrodynamic equations (conservation of mass, momentum and energy) is based on three assumptions:

- Pure periodicity of fluid elements: The gas returns to its initial position after a full cycle. This implies no net mass-loss.
- Radiative shock waves: the shocked gas cools quickly ( $t_{cool} \ll P$ ). This implies a thin layer immediately behind the shock front.
- Excursions of fluid elements are adiabatic with a constant adiabatic index  $\gamma_a$

The first two assumptions are perfectly satisfied in sufficiently deep layers of the atmosphere in the PPL. The third assumption is an approximation as  $\gamma_a$  may vary with the Lagrangian coordinate (diatomic molecules are not always the prevalent gas phase component).

In the PPL, it is sufficient to determine the structure between two shocks in order to derive the complete envelope structure consisting of an infinite series of coexistent (equidistant) shocks. Given that fluid elements move over distances much smaller than the stellar radius in the PPL ( $z_{max} \ll R$ ), the gravitational acceleration,

$$g = \Gamma MR^{-2}, \quad (3)$$

is roughly constant.  $\Gamma$  denotes the gravitational constant,  $M$  the stellar mass, and  $R$  the stellar radius, respectively.

Also the isothermal sound speed for an ideal gas,

$$c_s = \sqrt{\frac{dp}{d\rho}} = \sqrt{\frac{KT_c}{\mu m_H}}, \quad (4)$$

is constant by the assumption of constant cooling temperature  $T_c$ , mean molecular weight  $\mu$ , and adiabatic index  $\gamma_a$ . From dimensional analysis, it follows that the constant period  $P$  (i.e. the time between two shocks) is proportional to  $\frac{c_s}{g}$  and  $\frac{u_1}{g}$ , where  $u_1$  is the preshock velocity. Since  $c_s, g$ , and  $P$  are constant, the preshock velocity  $u_1$  must be constant as well.

Despite the assumption of pure periodic trajectories, AGB stars are losing mass. In order to account for an outwards directed motion, the gas phase abundances at full phase are rescaled the local gas number density by assuming the gas layer moves from a position  $R$  to a position  $R + 0.5 R_*$ . (Duari et al., 1999), (Cherchneff, 2006), (Cherchneff, 2012). For the dust grains, which are responsible for the mass-loss, the situation is different. The dust-free model of Nowotny et al. (2010) shows pure periodic behaviour of the gas shells, while models with dust show a gradual outward motion (Bowen, 1988), as illustrated in Figure 5.

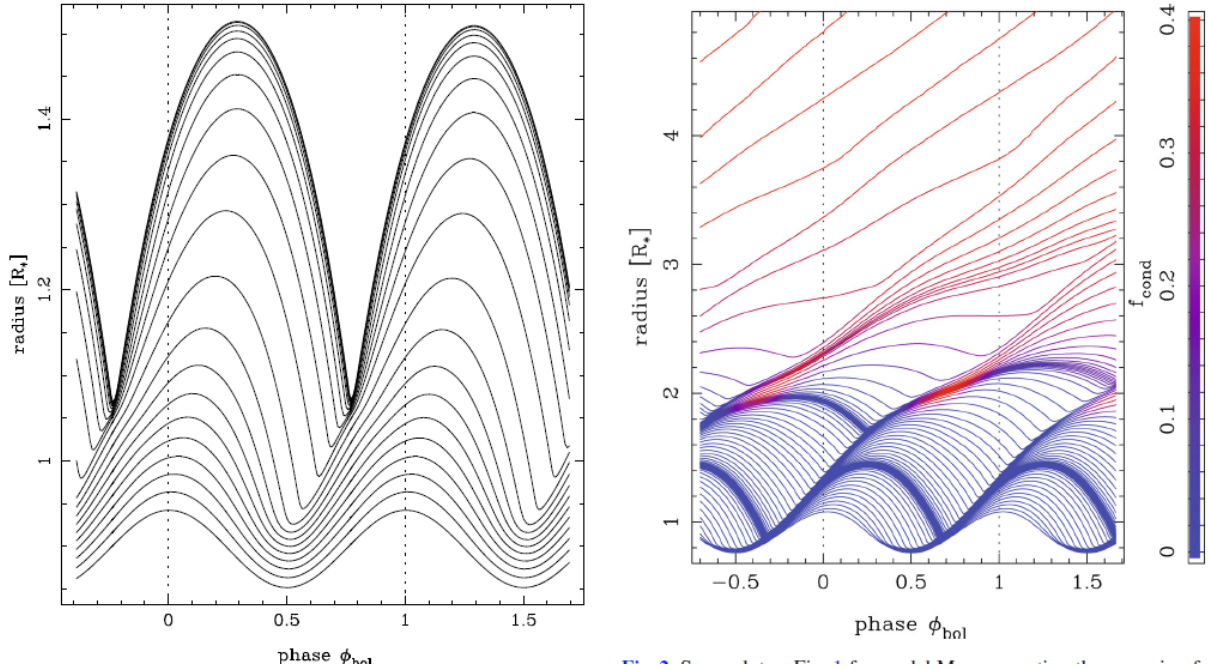


Figure 5: Results of the atmospheric models of Nowotny et al. (2010). The figures display the gas parcel trajectories in radial direction versus pulsation phase (time). *Left*: The dust-free model. The gas motion is purely periodic (no mass-loss). *Right*: The same model as on the left hand side but including dust. In this case a gradual outward motion is present (mass-loss).

More pulsations are therefore necessary in order to give the nascent grains enough time to grow and then levitate the gas layers to larger radii. The number of pulsations  $N_p$  for dust growth in a shell of thickness  $0.5 R_*$  can be approximated as follows:

$$N_p = \frac{0.5R_*}{v_D P}, \quad (5)$$

where  $P$  is the period and  $v_D$  is the drift velocity, a non-thermal velocity component causing Doppler line broadening, and accounting for mass-loss. In cool stars, large-scale motions are observed, which indicate drift velocities dominate over the thermal velocities. A drift velocity of  $1.5 \text{ km s}^{-1}$  is consistent with the results of Schöier et al. (2004) and corresponds to two pulsation periods per  $0.5 R_*$ . Closer to the star, the (outward directed) drift velocity is expected to be lower due to stronger gravity and higher densities. Six pulsations are necessary to cover a distance of  $0.5 R_*$ , if a drift velocity  $0.5 \text{ km s}^{-1}$  (Ramstedt et al., 2008) is presumed close to the star.

The thermodynamic conditions of the pre-shock gas as a function of the radial distance from the star are given by (Cherchneff et al. (1992)):

$$n(R) = n(R_0) \exp\left(\frac{-R_0(1-\gamma^2)}{H(R_0)(1-\alpha)} \left[1 - \left(\frac{R}{R_0}\right)^{\alpha-1}\right]\right) \quad (6)$$

and

$$T(R) = T_* \left(\frac{R}{R_0}\right)^{-\alpha} \quad (7)$$

where  $n$  is the number density,  $T$  the gas temperature,  $R_0=1 R_*$  the shock formation radius,  $H$  the scale height,  $\gamma = 0.89$  (for more details see Section 3.3), and  $\alpha = 0.6$ , respectively. The shock speed  $v_s$  is damped as it and scales with, owing to energy conservation. The resulting pre-shock gas conditions for  $n$  and  $T$  are listed in Figure 5 .

The model considered in this subsection is applied to a diatomic, molecular gas with a constant adiabatic index of  $\gamma_a = 1.4$  and has already been successful in explaining the inner envelope of IRC+10216 with a predominantly organic carbon-rich chemistry (Cherchneff et al., 1992), (Cau, 2002), (Cherchneff, 2011),(Cherchneff, 2012), envelopes of various chemical types including S-type stars (Cherchneff, 2006)) and for oxygen-rich stars (Duari et al., 1999) with an inorganic oxygen-rich chemistry.

## 3.2 Immediate Shock Layer

As previously mentioned, the shock layer behind the shock front is thin provided that the cooling time is much smaller than the period. BC85 assume that in this layer the gas cools radiatively down to temperature  $T_c$ , which marks the end point of the thin shock layer. BC85 did not treat radiative transfer in the shock layer as their model was hydrodynamical only, and thus the structure of the immediate layer was left undetermined (apart from being small compared with other spatial dimensions). The used calculation by BC85 starts at  $T_c$ , which is given by atomic and molecular physics and is assumed to be independent of the shock height.

In order to account for the relaxation processes of a shock-heated gas with  $T \geq T_c$  immediately behind the shock front the models of Fox & Wood (1985) are consulted. Their relaxation treatment is split into two parts differing in length scales and physical condition. internal relaxation and radiative recombination. In this framework, the internal relaxation zone is treated by the formalism of Fox & Wood (1985). In the internal relaxation zone (i.e. the thin shock layer), collisional dissociation of molecular hydrogen is the first process to occur, followed by processes involving excitation of H atoms by collisions with electrons. Electron collision from a high excitation level of H can lead to the ionisation of hydrogen. In the case of low shock speeds and shock temperatures, the thermal energy is taken by dissociation rather than by ionisation. Ions and ionic reactions are thus excluded from the chemical network and the cooling in the internal relaxation zone is provided by endothermic collisional dissociation reactions.

Instead of treating the immediate shock layer by solving complex multi-fluid radiative transfer equations, the immediate shock zone is treated a thin dissociation layer in the present framework. Most of the considered dissociation reactions are endothermic and have high energy barrier (owing to the binding energy of the molecular compounds). Thus, the thin shock layer is also called *chemical dissociation layer* or *chemical cooling layer*. As more than 99% of the gas consists of hydrogen and helium (see Table 6) and the latter is chemically inert, it is the dissociation of  $H_2$ , which dominates the cooling in the immediate shock layer. As the internal relaxation is confined to a geometrically thin region and occurs on a very short timescale, the set of differential equations describing the chemistry can

written as a function of the space variable  $x$ . The space coordinate  $x$  is then related to the time coordinate via the shock velocity. As a consequence, the narrow space extent of the immediate shock layer can be demonstrated, as done by (Willacy & Cherchneff, 1998), (Duari et al., 1999).

The dissociation length  $l_D$  is defined as

$$l_D = \frac{1}{k(H_2)n(H)} \frac{v_s}{n_j}, \quad (8)$$

where  $n(H)$  is the number density of atomic H in the shock,  $v_s$  the shock velocity, and  $n_j$  is the shock-induced jump in density.  $k(H_2)$  is the dominant dissociation rate of  $H_2$ , namely



and is given by

$$k(H_2) = 2.54 \times 10^{-8} \left( \frac{T}{300} \right) \exp\left( \frac{-52556}{T} \right). \quad (10)$$

For IK Tau and  $v_s = 32 \text{ km s}^{-1}$  the dissociation length at the photosphere is 0.16 cm, at  $3 R_*$   $l_D = 1.50 \times 10^6 \text{ cm}$  and at  $5 R_*$   $l_D = 1.16 \times 10^7 \text{ cm}$ . The trend of increasing dissociation lengths with larger radii reflects the model validity in the deep layers of the envelope and its failure at large radii. The reason for long dissociation lengths (and thus also larger immediate shock layers) is the inefficiency of the  $H_2$  dissociation through reaction 9 at lower temperatures and the low (hydrogen) number density in the outer layers.

The thermodynamic conditions immediately behind the shock front are given by the Rankine-Hugoniot jump conditions (see e.g. Tielens 2010), which express the conservation of mass, momentum and energy. In addition, an equation of state is necessary in order to relate pressure with energy. The resulting jumps in number density and temperature for a diatomic, ideal gas depend strongly on the Mach number  $M$ , which denotes the ratio of the velocity  $v$  relative to the local sound speed  $c_s$ . The resulting jumps in number density are

$$\frac{n_1}{n_0} = \left( \frac{\gamma_a - 1}{\gamma_a + 1} + \frac{2}{\gamma_a + 1} \frac{1}{M^2} \right)^{-1} \quad (11)$$

and for the temperature

$$\frac{T_1}{T_0} = \frac{(2\gamma_a M^2 - (\gamma_a - 1))((\gamma_a - 1)M^2 + 2)}{(\gamma_a + 1)^2 M^2}, \quad (12)$$

where subscript 0 refers to the preshock gas, subscript 1 to the shocked gas, and  $\gamma_a$  to the adiabatic index, respectively. For a diatomic, molecular gas the adiabatic index is  $\gamma_a = 1.4$ . Typical values for  $\frac{n_1}{n_0}$  are in the range of 4 - 6 and for  $\frac{T_1}{T_0}$  in the range of 4 - 20. The immediate post-shock conditions ( $T_1$  and  $n_1$ ) are relaxed to the initial values of the excursion,  $n_e$  and  $T_e$  (see Table 5). The dissociation time of  $H_2$  is less than 0.001 P for immediate post-shock conditions (Bowen, 1988). On the other hand, the time required

for returning to equilibrium  $t_{eq}$  exceeds a pulsation period  $P$  by far ( $t_{eq} > 100 P$ ). These timescales underline the necessity of a separate treatment for the two components of the post-shock gas, and the invalidity of TE in the inner envelope.

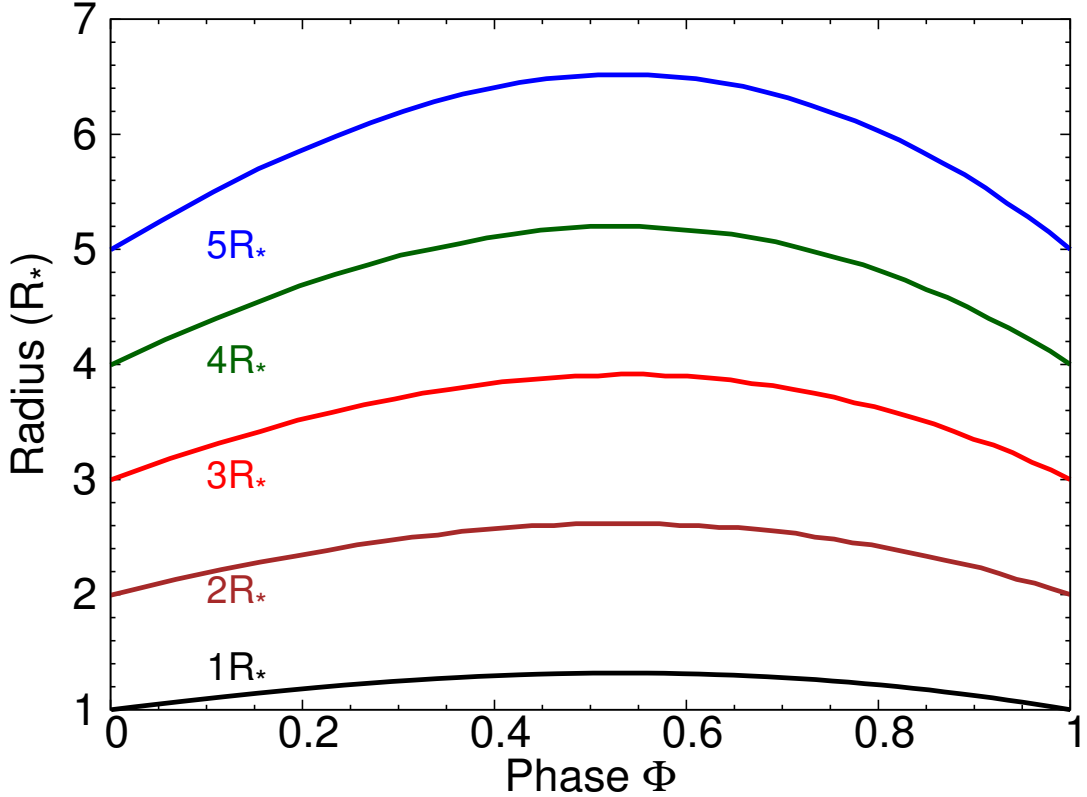


Figure 6: Adiabatic excursion of gas parcels at different radii versus pulsation phase for a photospheric shock speed of  $V_s^0 = 32 \text{ km s}^{-1}$  and sample star with  $R_* = 6 \times 10^{13} \text{ cm}$ . The motion of the gas is purely periodic.

### 3.3 Mass-loss, Densities and Velocities in the Wind

The mass-loss rates of the Mira variable IK Tau have been derived to be  $4.5 \times 10^{-6} M_{\odot}/\text{yr}$ ,  $8.0 \times 10^{-6} M_{\odot}/\text{yr}$  and  $1.0 \times 10^{-5} M_{\odot}/\text{yr}$  (Knapp & Morris, 1985), (Menten et al., 2010), (Schöier et al., 2013). Periods of high mass-loss are characterised by an enhanced wind density, and low number densities represent periods of low mass-loss.

The density correlates not only with mass-loss but also with the flow velocity: Gas velocities are directly linked to the density by the continuity equation. This fact is advantageous as velocities are easier to extract from spectroscopic line widths. The expansion velocity of IK Tau’s wind is  $22 \text{ km s}^{-1}$  (Omont et al., 1993) and  $18 \text{ km s}^{-1}$  (Menten et al., 2010), (Schöier et al., 2013). As the inner envelope is subject to periodic shock waves, the velocity structure of the wind is strongly fluctuating with respect to radial position and time. In the intermediate and outer envelope, the shock is strongly damped before it finally stalls. At this stage, gravity is negligibly weak, the dust has formed, the wind has reached its terminal velocity and flows continuously outwards.

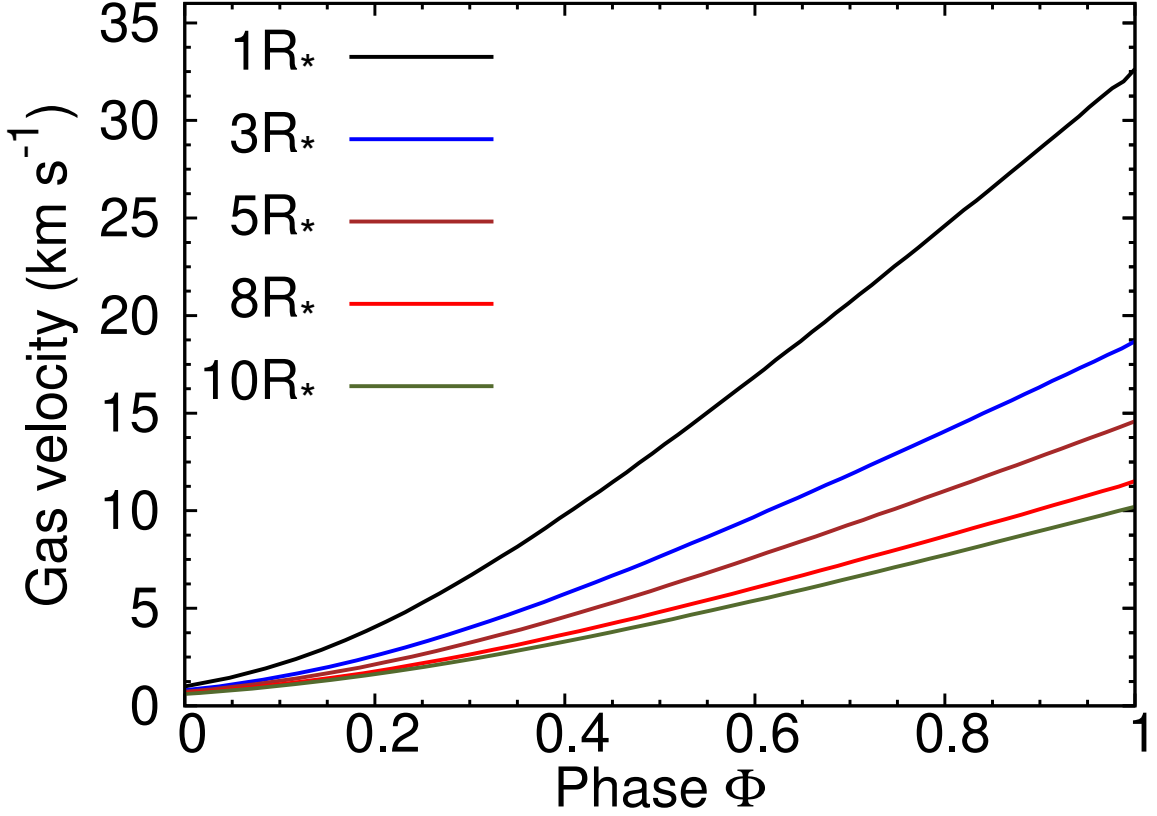


Figure 7: The post-shock gas velocity for a  $32 \text{ km s}^{-1}$  shock at several radii as function of time (pulsation phase). At full phase the gas velocity has reached the initial preshock value.

Decin et al. (2010a) showed by mapping of  $\text{H}_2\text{O}$  and  $\text{SiO}$  maser emission that the dusty wind reaches its terminal velocity of  $\sim 20 \text{ km s}^{-1}$  at around  $20 R_*$  (see Figure 10) and derives a mass-loss rate  $\dot{M}=8\times 10^{-6} M_\odot/\text{yr}$ . Assuming spherically symmetric mass loss (only in the radial direction), we are able to constrain the (mean) number density assuming mass conservation:

$$\dot{M} = 4\pi R^2 \rho V_\infty = 4\pi R^2 (n\mu m_H) V_\infty, \quad (13)$$

where  $\dot{M}$  is the mass-loss rate,  $R$  the radial distance,  $V_\infty$  the terminal velocity,  $\rho$  the mass density,  $n$  the number density, and  $\mu$  the mean molecular weight, and  $m_H$  the mass of the hydrogen atom, respectively. According to Decin et al. (2010a), the wind reaches its terminal velocity around  $20 R_*$ . Evaluating the model number density at  $20 R_*$ , according to mass conservation yields

$$n(R) = \frac{\dot{M}}{4\pi R^2 \mu m_H V_\infty} \quad (14)$$



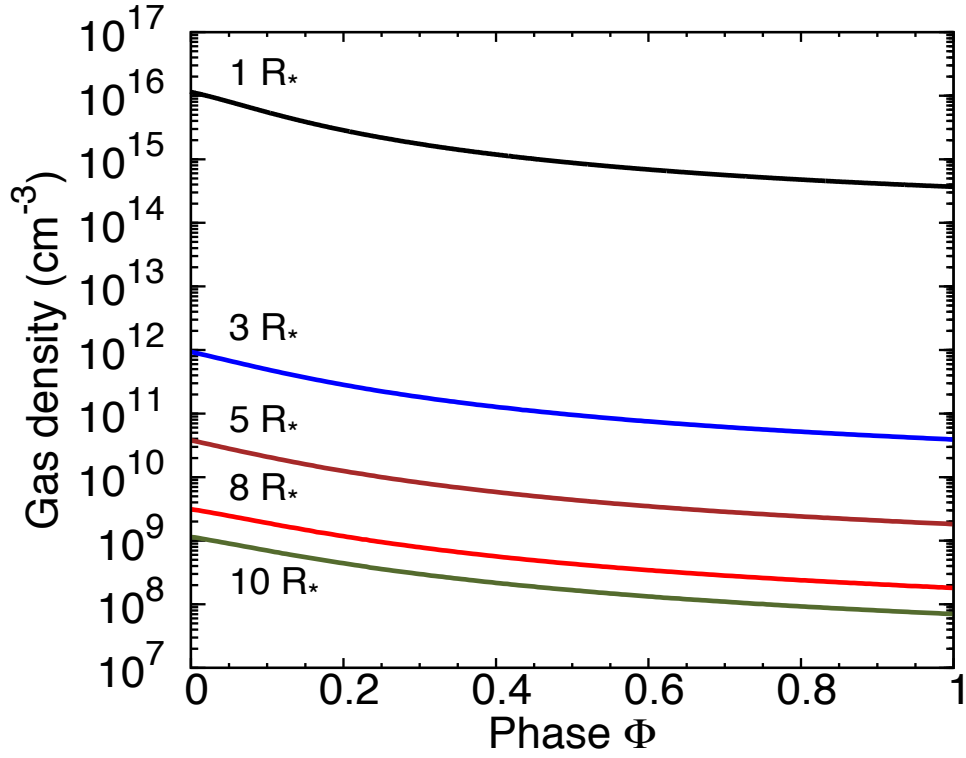


Figure 8: The post-shock gas density of for a  $32 \text{ km s}^{-1}$  shock at several radii as function of time (pulsation phase). At full phase the gas density has returns to the initial preshock value.

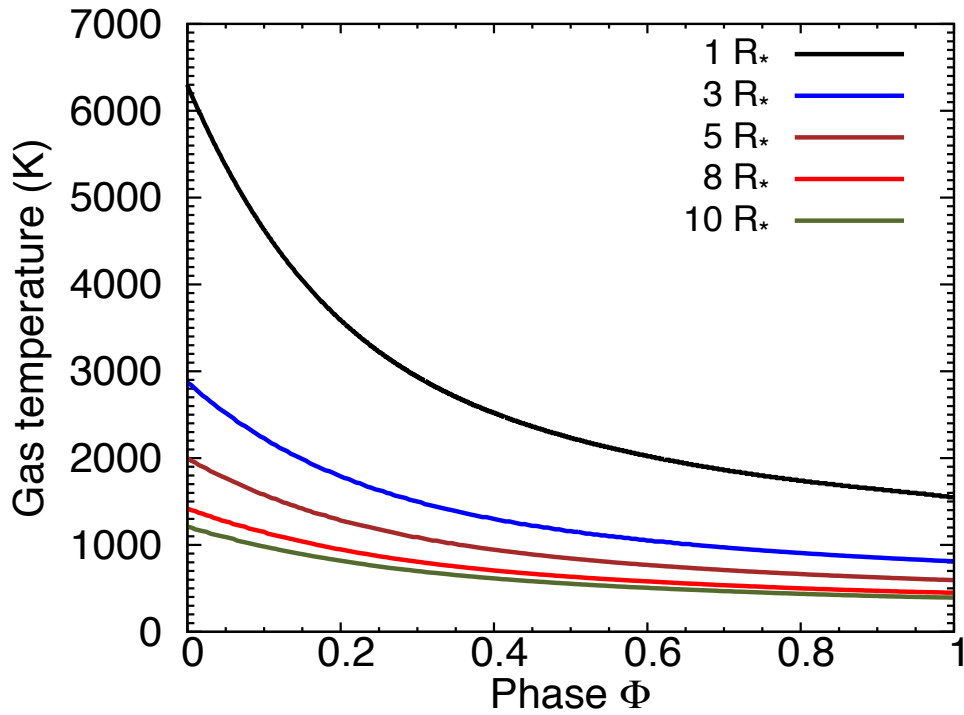


Figure 9: The post-shock gas temperature of IK Tau at several radii as function of time (pulsation phase).

$$n(20R_*) = \frac{\dot{M}}{4\pi(20R_*)^2\mu m_H V_\infty} = 2.7 \times 10^7 \text{ cm}^{-3} \quad (15)$$

Table 5: Kinetic temperatures and number densities and as function of the radial position in the preshock (subscript 0), immediate shock (subscript s) and post-shock (subscript e) gas. Shock speeds are given in  $\text{kms}^{-1}$ , number densities in  $\text{cm}^{-3}$ , and temperatures in K

R	preshock				shock front		excursion	
	$V_s$	M	$n_0$	$T_0$	$n_s$	$T_s$	$n_e$	$T_e$
1.0 $R_*$	32.0	9.8	3.62(14)	2200	2.06(15)	42824	1.16(16)	6295
1.5 $R_*$	26.1	9.0	7.77(12)	1725	4.39(13)	28793	2.23(14)	4741
2.0 $R_*$	22.6	8.5	7.25(11)	1451	4.07(12)	21712	1.92(13)	3858
2.5 $R_*$	20.2	8.1	1.38(11)	1270	7.69(11)	17473	3.43(12)	3277
3.0 $R_*$	18.5	7.8	3.95(10)	1138	2.19(11)	14638	9.36(11)	2874
3.5 $R_*$	17.1	7.6	1.47(10)	1037	8.11(10)	12630	3.32(11)	2568
4.0 $R_*$	16.0	7.4	6.54(09)	958	3.60(10)	11098	1.42(11)	2340
5.0 $R_*$	14.3	7.1	1.86(09)	838	1.01(10)	8930	3.79(10)	1997
6.0 $R_*$	13.1	6.8	7.20(08)	751	3.90(9)	7497	1.32(10)	1748
7.0 $R_*$	12.1	6.6	3.40(08)	684	1.83(9)	6460	5.99(9)	1574
8.0 $R_*$	11.3	6.4	1.85(08)	632	9.88(8)	5691	3.13(9)	1419
9.0 $R_*$	10.7	6.3	1.10(08)	589	5.88(8)	5082	1.82(9)	1307
10.0 $R_*$	10.1	6.2	7.11(07)	553	3.77(8)	4597	1.14(9)	1209

This is by a factor of  $\sim 4$  higher than the preshock number density at  $20 R_*$  in the present model. At  $8 R_*$ , which corresponds to  $2 \times 10^{14}$  cm, the wind has reached yet a velocity, which is greater than  $15 \text{ km s}^{-1}$ , as can be seen from Figure 10. At  $8 R_*$ , the number density reads

$$n(8R_*) = 1.7 \times 10^8 \text{ cm}^{-3} \quad (16)$$

This value is consistent with the model preshock density at  $8 R_*$  presented in Table 5. The equation holds for  $R \geq 8 R_*$ , when the wind has been fully accelerated and the pulsational shocks have sufficiently weakened. Inside  $8 R_*$ , a series of shocks is present in the atmosphere reflecting a highly complex density distribution, which cannot be described by means of a simple formalism (e.g. power-law).

From equation 14 follows that the quantity  $\dot{M}/v_e$  describes a normalised wind density with respect to R. This quantity is used to estimate molecular envelope sizes (see e.g. Schöier et al. 2013) and to derive a scaling law. Finally, molecular abundances can be obtained. For a given source and its characteristic parameters molecular abundances can be derived from the wind density and vice versa.

Alternatively, an initial preshock number density  $n_0$  at the shock formation radius can be estimated from a mass density  $\rho = 1 \times 10^{-10} \text{ g cm}^{-3}$  given in model B20 of Fox & Wood (1985):

$$n = \frac{\rho}{\mu m_H} \simeq 3.6 \times 10^{13} \text{ cm}^{-3} \quad (17)$$

where  $m_H$  denotes the mass of a hydrogen atom (i.e. an atomic mass unit).

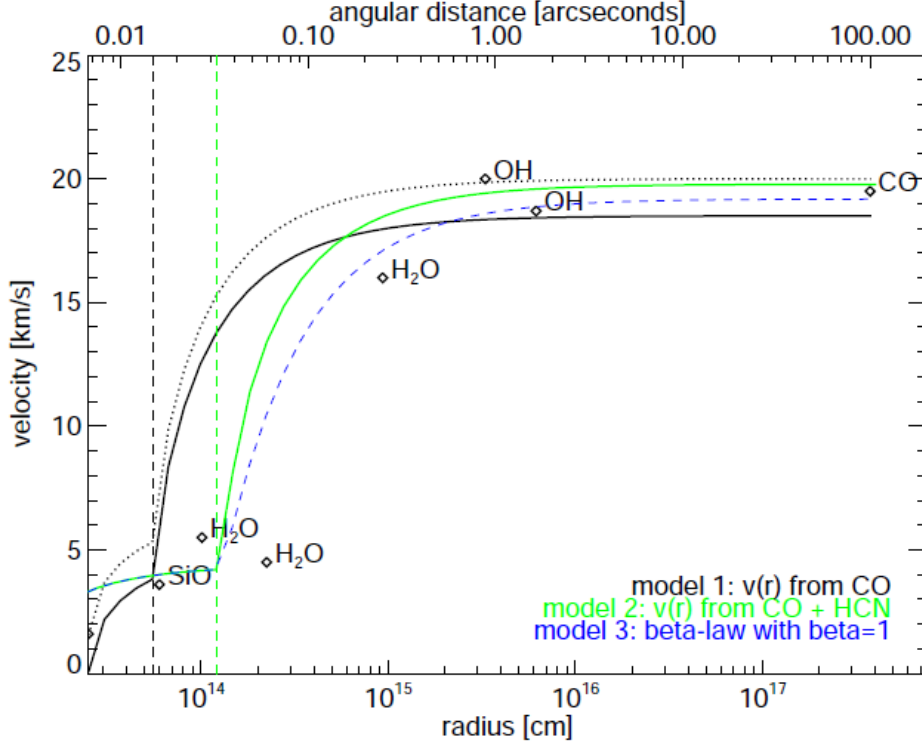


Figure 10: The velocity profile in the inner envelope as derived by Decin et al. (2010a) from CO, HCN and power-law line modelling.

This is by a factor of 10 lower than what is used in the pulsation model used in this thesis. Test runs with a density of  $3.6 \times 10^{13} \text{ cm}^{-3}$  led to a rapid conversion of molecular to atomic hydrogen. In order to obtain a density profile of IK Tau's inner wind, we introduce the scale height  $H$ , a characteristic length scale over which the pressure of the system changes significantly (by a factor  $1/e \approx 0.368$ ), (i.e. a large  $H$  means a slow decrease in pressure). As pressure and density are directly related by the equation of state of an ideal diatomic gas,  $H$  is also a measure of density variation along the radial distance. The gravitational pressure variation  $dP$  with respect height  $dh$  above the photosphere is given by

$$dP = \rho g dh = \rho \frac{\Gamma M_*}{R_*^2} dh, \quad (18)$$

where  $g$  denotes the gravitational acceleration and  $\Gamma$  the gravitational constant, respectively. The equation of state for a mole ( $= N_A$  particles) of molecular gas is

$$P = \frac{\rho}{\mu} RT = \frac{\rho}{\mu} N_A k_B T. \quad (19)$$

where  $k_B$  is the Boltzmann constant,  $R$  is the gas constant,  $M_*$  the mass and  $R_*$  the radius of the star, respectively. Eliminating  $\rho$ , integrating over  $dp$  and  $dh$ , respectively, solves the differential equation and gives the characteristic length scale  $H$ :

$$H = \frac{k_B T}{mg} = \frac{k_B T}{\mu m_H \Gamma \frac{M_*}{R_*^2}} = \frac{k_B T R_*^2 N_A}{M_* \Gamma \mu}. \quad (20)$$

Temperature, stellar mass, mean molecular weight  $\mu$ , and particularly radius determine the scale height at each radial distance from the star. Mira Variables generally have large scale heights according to their relatively low masses and very large radii. As a consequence, the mean gas number densities and pressures decrease slowly with distance from the star. These high gas number densities then favour molecule and cluster formation, and dust condensation. As our model is based on a diatomic molecular pre-shock gas with adiabatic index  $\gamma_a = 1.4$ , it is crucial for our calculations to guarantee the dominance of molecular hydrogen  $H_2$  in our computational zone between 1 and 8  $R_*$ . Molecular  $H_2$  is favoured over atomic H, if the gas density is above a critical value of roughly  $10^{10} \text{ cm}^{-3}$ .

In order to estimate the number density of the gas at the photosphere, information about the prevalent pressure and temperature is needed. The effective temperature can be extracted from the blackbody spectrum of the star. Photospheric pressures are very difficult to measure or to estimate. To afford condensation of dust grains within the inner envelope high pressures are required depending on dust composition, since grains form in regions of enhanced density (clumps, jets). Höfner (1999) examined different frequency-dependent molecular opacity models to settle pressure constraints and obtained pressures of  $0.1 - 10 \text{ dyne cm}^{-2}$ , which translate to number densities of  $3.62 \times 10^{11} - 3.62 \times 10^{13} \text{ cm}^{-3}$  at  $T = 2000 \text{ K}$ . In the models of Fox & Wood (1985), the role of gas densities is discussed. By comparing the resulting Balmer lines with observations, they concluded that their initial density of  $5 \times 10^{-11} \text{ g cm}^{-3}$  (which corresponds to  $3 \times 10^{13} \text{ cm}^{-3}$ ) is too high by a factor 10, indicating rather low photospheric densities.

The relation between mass-loss  $\dot{M}$ , terminal velocity  $v_\infty$ , and density profile has been established. In the circumstellar envelope, however, various types of velocities (flow, shock, drift, escape and terminal velocity) are present and we intend to discriminate among these types and relate them to each other.

The escape velocity  $v_{esc}$  results from equalising the kinetic energy and gravitational potential and is given by:

$$v_{esc} = \sqrt{\frac{2\Gamma M_*}{R}}. \quad (21)$$

At the photosphere of IK Tau ( $= 1 R_*$ ) this results in  $v_{esc} = 32.6 \text{ km s}^{-1}$ , which is slightly lower than the value of  $v_{esc}=35.4 \text{ km s}^{-1}$  derived by Duari et al. (1999), who used a smaller radius  $R_*$  for IK Tau. As a consequence, the ratio of shock and escape velocity would be  $\gamma=\Delta v/v_{esc}=0.98$ . This is slightly higher than the value of  $\gamma=0.89$  used in the previous models (Cherchneff et al., 1992), (Duari et al., 1999). In order to compare the results with these previous studies, the value of  $\gamma=0.89$  is maintained by adopting a stellar mass of  $1.2 M_\odot$  for IK Tau, consistent with the stellar evolution model  $M_*^{ini} = 1.5 M_\odot$  model of FRUITY. It should be noted, however, that IK Tau clearly deviates from the pulsation period - mass loss relation (Vassiliadis & Wood (1993)) used in the FRUITY models. For the pulsation

period of IK Tau (470 days) the mass loss rate is  $\sim 4$  times higher than expected from period mass loss relation. A current stellar mass of 1.0-1.2  $M_{\odot}$  for IK Tau is thus reasonable. When the shock forms, the instantaneous flow velocity  $v$  may be approximated to be an average value scaled to the local escape velocity  $v_{esc}$  and  $v$  can be expressed by  $\gamma v_{esc}$  (Willson & Bowen, 1984), (Cherchneff et al., 1992). Thus, the local flow velocity  $v$  close to the shock formation radius can be approximated the shock velocity.

The flow velocity also represents the (thermal) preshock velocity  $u_1$  (see Section 3). The velocity of the gas parcel (i.e. the flow velocity) changes its sign when the gas parcel has reached its maximum height in the excursion. Moreover, the flow velocity relates the Eulerian with the Lagrangian coordinate frame. The latter is used for the description of the gas parcel excursions.

In Section 3.3, the drift velocity  $v_D$  was introduced. It represents the net, outward directed flow of the gas and is assumed to be  $0.5 \text{ km s}^{-1}$  close to star and  $1.5 \text{ km s}^{-1}$  around  $4 R_*$ . Further out, the drift velocity transfers to the terminal velocity (see Figure 10). The terminal velocity  $v_{\infty}$ , however, relates to regions in the intermediate envelope ( $20 - 100 R_*$ ), where the wind has fully accelerated and is closely linked to the mass-loss phenomena (See Section 3.3).

### 3.4 Stellar Mass

The mass is the most crucial property of a star as it determines its life time, evolution and death (see Section 2). In general, masses of single, isolated stars are difficult to ascertain. There is the empiric mass-luminosity relation  $L \propto M^{3.5}$  (see e.g. Harwit 1988), but it holds only for hydrogen burning main-sequence stars and not for higher evolved giant stars. Another way of to determine stellar masses is via pulsation. If the star pulsates such as IK Tau, it satisfies the standard pulsation equation for Miras (Fox & Wood, 1982):

$$Q = P \left( \frac{M_*}{M_{\odot}} \right)^{\frac{1}{2}} \left( \frac{R_*}{R_{\odot}} \right)^{-\frac{3}{2}} = 0.09 \quad (22)$$

where  $P$  is the pulsation period in days,  $M_*$  the mass, and  $R_*$  the radius of the star, respectively. The pulsation period  $P$  and the average radial extension can be observed by knowing the distance to IK Tau and hence, the stellar mass can be obtained by applying the above equation. With  $P = 470$  days and  $R = 305 R_{\odot}$ , the stellar mass is roughly  $1 M_{\odot}$  (Duari et al., 1999). Recent observations (Decin et al., 2010a) give a larger radius  $R = 2.5 \times 10^{13} \text{ cm} = 360 R_{\odot}$  for IK Tau, which yields a stellar mass of  $M_*=1.7 M_{\odot}$ . The impact on our results by using a higher stellar mass of  $M_*=1.7 M_{\odot}$  are drastic. The lower scale heights and the resulting density drop lead to a rapid conversion of molecules to atoms. To illustrate the impact of stellar mass, we first consider the gravitational acceleration,  $g(r)$ ,

$$g(r) = \Gamma \frac{M_*}{(rR_*)^2}, \quad (23)$$

where  $M_*$  the stellar mass,  $R_*$  the stellar radius, and  $r$  (in stellar units) the distance

form the star, respectively. The gravitational acceleration  $g(r)$  not only determines the scale height, but also directly enters the momentum equation. According to equations 23 and 20, a high stellar mass / gravity significantly shortens the scale heights and the preshock gas densities (and hence, the number densities in the post-shock gas) decrease much faster with radius. Expressed in number densities, it reads  $n(3R_*) = 6.6 \times 10^8 \text{ cm}^{-3}$  and  $n(5R_*) = 3.7 \times 10^6 \text{ cm}^{-3}$ . For these specific number densities, which are rather rarefied conditions in circumstellar envelopes, atoms prevail and molecules lack in large parts. The precondition of a molecular gas with  $\gamma_a = 1.4$  is not satisfied for small scale heights and low densities, and thus breaks down. Moreover, at  $20 R_*$ , where the wind is fully accelerated, gas number densities of  $n \sim 200 \text{ cm}^{-3}$  could not account for the mass-loss of the order of  $10^{-6} - 10^{-5} M_\odot/\text{yr}$  in the  $1.7 M_*$  test model. Therefore, a stellar mass of  $1.7 M_\odot$  seems no to be appropriate for the purpose of the model.

Another issue concerning a higher star mass arises: In a model with mass-loss, more pulsations would be needed to overcome the gravitational well and to push the gas (and dust) outwards. In the model, the quasi-ballistic excursions of the gas parcel are hampered by the stronger G-field and, as a consequence, do not reach the heights of the  $1 M_\odot$  models (see Figure 11).

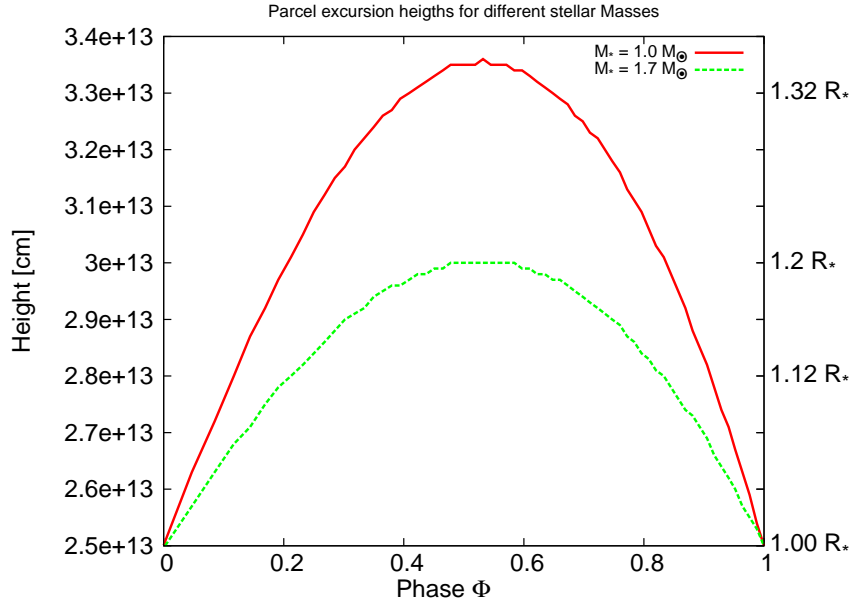


Figure 11: Shock-induced excursions of a post-shock gas parcel at  $1 R_*$ . As a consequence of the stronger G field the excursion of the  $M_*=1.7 M_\odot$  model does not reach the heights of the  $1 M_\odot$  model.

In the two different sets of evolutionary codes, we chose the initial mass of the model star to be around  $M_*^{ini} \sim 1.5 M_\odot$ . This is justified as stars are losing mass, particularly during their evolution along the AGB, and IK Tau has already evolved on the AGB. In the present

model, the stellar evolution code FRUITY is used for the element calculation. Following its stellar evolution, a C/O ratio of 0.75 is reached after about 3 of total 5 thermal pulses with subsequent dredge-up episodes. The elemental initial compositions are further discussed in Section 4.1

The  $M_*^{ini} = 1 M_\odot$  model of FRUITY at solar metallicity only experiences the first dredge-up and no further third dredge-up episodes. It is thus a low-mass red giant star not experiencing third dredge-up episodes, and not appropriate for our computations.

### 3.5 Pulsation

Stellar pulsations, present in a wide range of stars such as Cepheids and Miras, are fundamental in stellar physics. Historically, the pulsating cepheids with periods of the order of days are found to cross the so-called instability strip, which is a nearly vertical region in the Hertzsprung-Russel diagram. Later, a second instability strip, located on the right hand side of the Cepheids in the HRD, has been found (Gautschi, 1999). This second strip is populated by long period Mira variables. The origin of stellar pulsations is probably the unstable ionisation of hydrogen via the  $\kappa$ -mechanism in the interior of the star. In this context,  $\kappa$  represents the opacity inside the star, which depends on pressure, temperature, and wavelength. If the temperature and density increase for some reason, the opacity  $\kappa$  increases as well, owing to the free electrons emerging from ionisation processes. Hence, stellar photons accumulate and establish a ram pressure (i.e. radiation pressure on the stellar material). The driving occurs around 0.90-0.92  $R_*$  in the ionisation zone just below the photosphere (Bowen, 1988). The inertia of the stellar material and its restoring force thus lead to the oscillation / pulsation phenomenon.

Regardless of the exact mechanism responsible for stellar pulsation, it causes a periodical distortion of the star's hydrostatic equilibrium. Often the pulsation is assumed to be a simple sinusoidal variation of the photosphere. The most detailed models to date treat stellar pulsation as a moving piston with an amplitude  $\delta v$ , representing the velocity variation during one cycle. The piston is located just below the photosphere Mattsson et al. (2007), but a physically self-consistent way for modelling stellar pulsation does not yet exist.

In AGB stars, in particular in Mira variables, pulsations are strong enough to levitate stellar atmospheres which cool and enable the formation of molecules and dust in the regions above the photosphere. Mira stars pulsate in the fundamental mode and thus only in the radial direction with a well-defined pulsation period of several 100 days. The situation is different for semi-regular stars. Their pulsation periods are generally shorter and these stars are believed to pulsate in overtone modes. The grains are coupled to the gas and thus transfer momentum to the surrounding gas.

Therefore two requirements have to be satisfied: Firstly, periodic pulsations, which lead to the levitation of photospheric and atmospheric layers, providing cool and dense conditions within a reasonable timescale. Secondly, the formation and growth of dust grains in order to account for a large enough opacity source.

## 4 Chemistry

### 4.1 Initial Elemental Compositions

Elemental abundances are crucial inputs to the chemistry as molecular abundances are limited by the availability of the elements entering the chemical composition of the molecule. The element with the lesser abundance thus controls the maximum abundance a molecule can reach.

Sulphur oxide, SO, for example, can neither exceed the abundance of  $\sim 5 \times 10^{-4}$  (the maximum solar oxygen abundance) nor an abundance of  $\sim 1 \times 10^{-5}$  and is thus constraint to have an abundance below  $\sim 1 \times 10^{-5}$ . Therefore, the element with the smallest abundance, which enters the composition of a molecule, limits the final abundance the species can have. Not only the total mass of the system is conserved, but also the mass and the number of each element is preserved (*element conservation*). Element conservation applies for the computations presented here. Processes (cosmic rays,  $\beta$ -decays) which alter the proton number  $Z$  are consequently neglected.

In total 17 distinct elements from hydrogen up to iron are invoked in the chemistry which consists of 105 molecules. These elements include the elements (H,C,N,O,P and S), metals (Na, Mg, Al, Si, K, Ca, Ti and Fe) and halogens (F and Cl) as well as He which is chemically inert.

Following Habing & Olofsson (2003) the photospheres of AGB stars have solar-like compositions. We use the most recent and updated solar abundances from Asplund et al. (2009) with an corrected C/O ratio of 0.75 to account for the evolutionary stage in the case IK Tau (the actual solar C/O value is  $\sim 0.55$ ). The standard spectroscopic notation of elemental abundances uses a logarithmic scale and is given by

$$[i] = \log\left(\frac{N_i}{N_H}\right) + 12.0 \quad (24)$$

where  $i$  represents the element,  $N_i$  the number density or abundance of element  $i$ , and  $N_H$  the number density or abundance of hydrogen, respectively. For specific stars, star clusters and galaxies often the deviation from the standard solar composition is given by

$$[i/H] = \log\left(\frac{N_i}{N_H}\right)_* - \log\left(\frac{N_i}{N_H}\right)_\odot \quad (25)$$

where a positive number means an enhanced abundance of element  $i$  and a negative number a reduced abundance of element  $i$ , compared to the solar value.

Stellar evolution codes provide elemental yields at various times and for a range of stellar masses and metallicities in the AGB phase. In comparison to scaled solar compositions, the use of elemental abundances from evolutionary code is more accurate. However, theoretical uncertainties in the nuclear reaction rates, the treatment H-He intershell boundary, or the convective overshooting (see e.g. Cassisi 2005) may affect the elemental yields significantly.



Table 6: Solar abundances as derived by Asplund et al. (2009) in the fractional abundance representation (normalised to 1) and mass fractions of the elements.

Element	Z	A	Abundance	Mass fraction
H	1	1	0.921	0.737
He	2	4	0.078	0.251
C	6	12	$2.48 \times 10^{-4}$	$2.38 \times 10^{-3}$
N	7	14	$6.23 \times 10^{-5}$	$6.98 \times 10^{-4}$
O	8	16	$4.51 \times 10^{-4}$	$5.78 \times 10^{-3}$
F	9	19	$3.34 \times 10^{-8}$	$5.08 \times 10^{-7}$
Na	11	23	$1.60 \times 10^{-6}$	$2.95 \times 10^{-5}$
Mg	12	24.3	$3.67 \times 10^{-5}$	$7.04 \times 10^{-4}$
Al	13	27	$2.60 \times 10^{-6}$	$5.61 \times 10^{-5}$
Si	14	28.1	$2.98 \times 10^{-5}$	$2.95 \times 10^{-5}$
P	15	31	$2.37 \times 10^{-7}$	$5.87 \times 10^{-6}$
S	16	32.1	$1.21 \times 10^{-5}$	$3.11 \times 10^{-4}$
Cl	17	35.5	$2.91 \times 10^{-7}$	$8.16 \times 10^{-6}$
K	19	39.1	$9.87 \times 10^{-8}$	$3.08 \times 10^{-6}$
Ca	20	40.1	$2.01 \times 10^{-6}$	$6.45 \times 10^{-5}$
Ti	22	47.9	$8.21 \times 10^{-8}$	$3.15 \times 10^{-6}$
Fe	26	56	$2.91 \times 10^{-5}$	$1.31 \times 10^{-3}$

In this thesis, elemental compositions of two state-of-the-art stellar evolution codes are used and compared. They are the *Updates Yields from AGB models*, hereafter UYAGB (Karakas & Lattanzio, 2007), (Karakas, 2010), and *FUII network Repository of Updated Isotopic Tables & Yields*, hereafter FRUITY (Cristallo et al., 2011), (Straniero et al., 2014).

The main difference between these two isotopic databases is the treatment of the region where the burning shell fades into the convective envelope, the so called He intershell. FRUITY uses an exponential decay of the convective velocity in the unstable region (convective boundary), whereas UYAGB applies a sudden increase in the diffusion coefficient  $D$  at the convective boundary following Herwig et al. (1997).

Both models provide isotopic mass fractions, which are converted to number densities to compute the molecular equilibrium at the photosphere (see Section 4.3).

In contrast to UYAGB, FRUITY allows to follow the evolution on the AGB as they provide isotopic mass fractions as a function of time (number of experienced thermal pulses). In the case of the present model, the parameters are  $M_*^{ini} = (1.5-2) M_\odot$ ,  $Z = 0.003, 0.008, 0.014$  resulting in 5-16 thermal pulses, depending on the specific configuration. dredge-up episodes, respectively. As the C/O is rescaled to the value of 0.75 and dredge-ups mainly enhance the carbon abundance, our results are not severely affected by comparing the outcome of different third dredge-up episodes for a given stellar mass and metallicity.

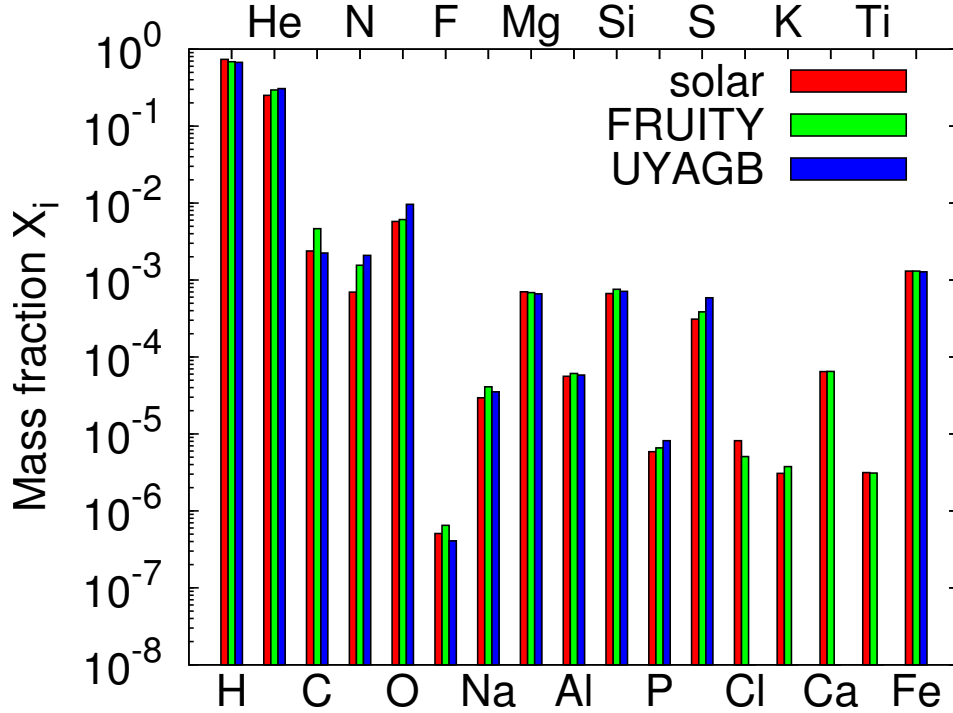


Figure 12: Elemental gas phase compositions of solar-like type and from the stellar evolution model FRUITY and UYAGB. The UYAGB model lack yields for Cl,K,Ca and Ti.

## 4.2 Metallicity

For decades the widely accepted and used literary value of the solar metallicity was  $Z_{\odot} = 1 - X_{\odot} - Y_{\odot} = 0.02$ . Recent investigation of the elemental composition of the sun (Asplund et al., 2009) revealed that its actual value is considerably lower  $Z_{\odot} \approx 0.014$ . In order to account for stars of subsolar metallicity the solar composition can be scaled by reducing the abundances for elements heavier than He. By doing so, however, metallicity effects on the stellar structure and stellar physics are neglected. Such effects comprise luminosity, effective temperature, mixing (Wachter et al., 2008). For example, the temperature at the bottom of the convective envelope  $T_{bce}$  increases with decreasing metallicity  $Z$ , which results in enhanced hoiy bottom burning (see e.g. Boothroyd & Sackmann 1991) and finally preventing that an AGB star turns carbon-rich. On the other hand, the selected metallicities are not too low that the assumed stellar structure would be drastically different.

For the computation presented here, the elemental abundances of FRUITY at different metallicities are used: the updated, solar  $Z=0.014$  case, the  $Z=0.008$  and  $Z=0.003$  cases, which account for AGBs in the LMC and the SMC, respectively. These initial compositions are based on a stellar-evolution code (starting from core H-burning on the main sequence ascending the red and asymptotic giant branches and ending as white dwarfs) and thus covering the complete AGB phase.

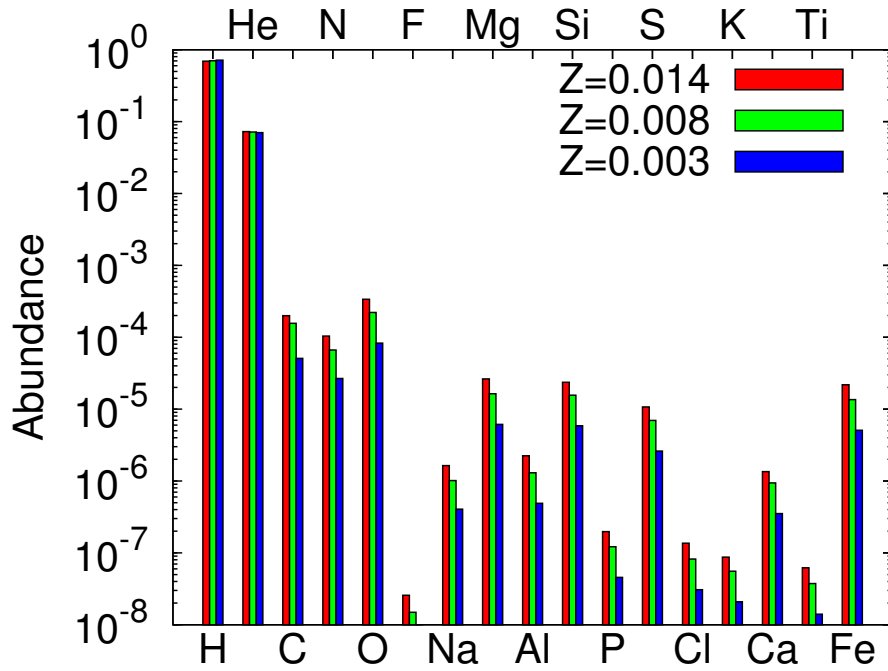


Figure 13: Elemental gas phase compositions at different metallicities accounting for stars in the Galaxy, the LMC and the SMC.

### 4.3 Thermodynamic Equilibrium

As pointed out this work relies on non-equilibrium chemistry and conditions. It is thus important to define the range of the validity of thermodynamic equilibrium (TE). TE holds, if

- Thermal equilibrium: All components of the gas have the same temperature  $T = T_{eq}$
- Chemical equilibrium: All forward and reverse reactions are balanced. For a given gas pressure and temperature, all components have a constant abundance (chemical potential  $\mu=0$ ).
- Mechanical equilibrium: No net motion (static system).
- Radiative equilibrium: The energy amount of incident radiation equals the energy of the emitted photons in the gas, resulting in no radiative heating / cooling of the molecules / elements.

are satisfied.

The molecular preshock abundances at the shock formation radius, which coincides for most cases with the photospheric radius, are estimated according to thermodynamic equilibrium. The idea is based on the minimisation of the Gibbs Free Energy (GFE) of formation of a gas phase mixture (White et al., 1958). Tsuji (1973) applied the method to the physical conditions of cool stellar atmospheres with various elemental compositions to derive

information on the chemical content of AGB envelopes, while (Cherchneff et al., 1992) has used TE to calculate the photospheric abundances of Polycyclic Aromatic Hydrocarbons in carbon stars.

The Gibbs free energy change  $\Delta G$  is defined as

$$\Delta G = \Delta H - T\Delta S \quad (26)$$

where  $\Delta H$  denotes the enthalpy,  $T$  the temperature and  $\Delta S$  the entropy, respectively.

The equilibrium constant  $K_{eq}$  can be expressed in terms of the Gibbs Free Energy change

$$K_{eq} = \exp\left(\frac{-\Delta G^0}{RT}\right) \quad (27)$$

where  $\Delta G^0$  is the Gibbs Free energy (GFE) of change at equilibrium.

It is assumed that molecules are of the general form  $X_l Y_m Z_n$  and are formed by its free constituent atoms  $X$ ,  $Y$  and  $Z$ . A fictitious pressure is attributed to each elemental species  $X$ ,  $Y$ , and  $Z$  (Cherchneff et al., 1992). *Fictitious* pressures correspond to pressure an element would have, if the gas were completely dissociated. Furthermore,  $\Delta G_r$  can be written in terms of the GFE of formation:

$$\Delta G_r^0 = \Delta G_f^0(X_l Y_m Z_n) - l\Delta G_f^0(X) - m\Delta G_f^0(Y) - n\Delta G_f^0(Z) \quad (28)$$

The above formulation has the great advantage that the values for  $\Delta G_f^0$  are tabulated for a large variety of molecules and atoms in the JANAF database (Chase, 1986). With the introduction of the *fictitious* pressure,  $K_{eq}$  can be written as follows.

$$K_{eq} = \frac{P(X_l Y_m Z_n)}{P(X)^l P(Y)^m P(Z)^n}, \quad (29)$$

where  $P(X_l Y_m Z_n)$ ,  $P(X)$ ,  $P(Y)$  and  $P(Z)$  are the partial pressures of the molecule  $X_l Y_m Z_n$ , atom  $X$ , atom  $Y$ , and atom  $Z$ , respectively. Following Tsuji (1973), the partial pressure of molecules can be parametrised according to the formula

$$\log(K_{eq}) = a_0 + a_1\Theta + a_2\Theta^2 + a_3\Theta^3 + a_4\Theta^4, \quad (30)$$

where the  $a_i$ 's are the fitting coefficients tabulated in Tsuji (1973),  $\Theta = 5040/T$  and  $T$  is temperature. In the case of a molecule not tabulated, or in case that improved thermochemical data are available, the JANAF tables (Chase, 1986) are used.

The partial equilibrium pressures can easily be converted to number densities by applying the ideal gas equation

$$P(X) = n(X)k_B T, \quad (31)$$

where  $n(X)$  is the number density of species  $X$ ,  $k_B$  the Boltzmann constant, and  $T$  the temperature.

Consequently, the equilibrium constant and the molecular equilibrium abundances depend on temperature, gas pressure, elemental composition, and the GFE of the gas.

Table 7: Molecular equilibrium abundances as a function of stellar temperature (top), photospheric density (middle), and C/O ratio (bottom).

TE abundances at $n_0 = 3.6 \times 10^{14} \text{ cm}^{-3}$ and C/O=0.75				
Molecule	T=1800 K	T=2200 K	T=2600 K	T=3000 K
H	3.46(-2)	3.82(-1)	8.52(-1)	9.16(-1)
H <sub>2</sub>	8.22(-1)	5.00(-1)	6.37(-2)	5.04(-3)
H <sub>2</sub> O	1.51(-4)	1.07(-4)	2.89(-6)	1.57(-8)
OH	4.29(-7)	1.16(-5)	9.12(-6)	9.72(-7)
CO	6.16(-4)	5.07(-4)	3.60(-4)	3.40(-4)
CO <sub>2</sub>	3.04(-8)	2.08(-8)	2.55(-9)	1.45(-10)
SiO	5.35(-5)	4.47(-5)	3.04(-5)	5.67(-6)
HCN	3.55(-12)	2.15(-12)	2.55(-12)	1.07(-11)

TE abundances at T=2200 K and C/O=0.75				
Molecule	$n_0/100$	$n_0/10$	$n_0$	$n_0 \times 10$
H	8.92(-1)	7.26(-1)	3.82(-1)	1.45(-1)
H <sub>2</sub>	2.72(-2)	1.81(-1)	5.00(-1)	7.20(-1)
H <sub>2</sub> O	7.78(-7)	3.12(-5)	1.07(-4)	1.38(-4)
OH	3.62(-6)	1.78(-5)	1.16(-5)	3.96(-6)
CO	3.48(-4)	4.00(-4)	5.07(-4)	5.82(-4)
CO <sub>2</sub>	1.91(-9)	1.32(-8)	2.08(-8)	2.15(-8)
SiO	3.05(-5)	3.51(-5)	4.47(-5)	5.10(-5)
HCN	2.12(-14)	1.12(-13)	2.15(-12)	3.51(-11)

TE abundances at $n_0 = 3.6 \times 10^{14} \text{ cm}^{-3}$ and T=2200 K				
Molecule	C/O=0.65	C/O=0.75	C/O=0.85	C/O=0.95
H	3.82(-1)	3.82(-1)	3.82(-1)	3.82(-1)
H <sub>2</sub>	5.00(-1)	5.00(-1)	5.00(-1)	5.00(-1)
H <sub>2</sub> O	1.65(-4)	1.07(-4)	4.87(-5)	3.20(-7)
OH	1.79(-5)	1.16(-5)	5.29(-6)	3.48(-8)
CO	4.40(-4)	5.07(-4)	5.75(-4)	6.43(-4)
CO <sub>2</sub>	2.79(-8)	2.08(-8)	1.08(-8)	7.91(-8)
SiO	4.47(-5)	4.47(-5)	4.46(-5)	3.34(-5)
HCN	1.21(-12)	2.15(-12)	5.33(-12)	9.07(-12)

In Table 7 several trends are observable and can be summarised as follows:

- Under rather cool and dense equilibrium conditions molecules such as H<sub>2</sub> prevail.
- In a hot and dilute equilibrium atoms dominate the gas phase.
- Carbon-bearing species are less abundant at low C/O ratios.

- With decreasing C/O ratios, equilibrium abundances increase for O-bearing molecules, except CO.
- The closer the C/O ratio to unity, the higher the CO fractional abundance.

## 4.4 Chemical-Kinetic Networks

Chemical kinetics is the field in physical chemistry concerned with chemical reactions and their rates at various thermodynamic gas conditions (temperatures and pressures). Every possible reaction is presumed to be reversible, and has a counterpart - its reverse reaction. Reverse reactions are crucial to the chemistry, as they balance the chemical network. If the gas density and temperature are constant over time, an equilibrium gas phase mixture is established. If the gas conditions of a dynamic equilibrium are disturbed, the position of equilibrium moves to partially reverse the change (Le Chatelier's principle) In non-equilibrium chemistry, the gas conditions change rapidly and the timescales are short. The types of chemical reactions are presented in Table 8.

Table 8: Reaction types used in the chemical network, their chemical formulation/representation and the gas condition, in which these reaction types are efficient.

Reaction type	Reaction	formulation	Gas conditions
<i>Unimolecular</i>			
Thermal decomposition	AB	$\rightarrow A + B$	High T
<i>Bimolecular</i>			
Neutral-exchange	AB + C	$\rightarrow A + CB$	T dependent
Collisional dissociation	AB + M	$\rightarrow A + B + M$	High T
Radiative association	A + B	$\rightarrow AB + \gamma$	T independent
<i>Termolecular</i>			
Termolecular formation	A + B + M	$\rightarrow AB + M$	(Very) high n
<i>Ionic</i>			
Dissociative recombination	AB <sup>+</sup> + e <sup>-</sup>	$\rightarrow A + B$	
Ion-neutral	AB <sup>+</sup> + C	$\rightarrow C^+ + AB$	
Charge-exchange	A <sup>+</sup> + B	$\rightarrow A + B^+$	
Photo-dissociation	AB + $\gamma$	$\rightarrow A + B$	

In the inner AGB envelopes, neither stellar and nor interstellar radiation is considered to ionise circumstellar material as pointed out in Section 3.2. Consequently, reaction types in the ionic section of Table 8 are not part of the chemical network used in this thesis. Neutral-exchange reactions occur in collisions that result in two product species. It is also possible that the collision between gas constituents leads to one product species in an excited state. In such a case, the excited state relaxes to the ground-state of the product species by the emission of radiation (i.e. radiative association). It is improbable, that a two-particle-collision leads directly to the ground-state of a single product species. Instead, it is more

likely that a third species M is involved in the collision (i.e. termolecular formation). M acts as a catalyst, as it is neither consumed nor produced in the reaction. In this case, the collision partner M controls the reaction kinetics. Termolecular formations are strongly density dependent as they require the simultaneous collision of three gas constituents in one event. The reverse process is called collisional dissociation and fragments molecules by the collision with M. It is an important reaction type as it breaks chemical bonds and can lead to the reformation/readjustment of molecules. Spontaneous unimolecular dissociations of molecules are unlikely to occur unless the molecule is unstable.

The majority of the reactions used in the network are two-body neutral-neutral reactions such as



The variation of species C and D due to the above reaction is expressed by the temporal derivative of the number density of species C,  $dn(C)/dt$ , and species D,  $dn(D)/dt$ , respectively:

$$\frac{dn(C)}{dt} = \frac{dn(D)}{dt} = kn(A)n(B) \quad (33)$$

where  $k$  is the reaction rate, and the expression  $kn(A)n(B)$  is the flux of species C, and B, respectively. The reaction rate  $k$  is given in the Arrhenius form (Arrhenius, 1899)

$$k = \alpha \left( \frac{T}{300} \right)^\beta \exp\left( \frac{\gamma}{T} \right) \quad (34)$$

with  $T$  is equal to the gas temperature. The parameters  $\alpha$ ,  $\beta$  and  $\gamma$  are empirical. The pre-exponential factor  $\alpha$  is a temperature-independent value of the order of  $10^{-9}$  -  $10^{-15}$   $\text{cm}^3\text{s}^{-1}$  for bimolecular reactions. Termolecular reactions, in contrast, take values of the order  $10^{-27}$  -  $10^{-33}$   $\text{cm}^6\text{s}^{-1}$ . The difference in value and units is founded as the flux always has units of  $\text{cm}^{-3}\text{s}^{-1}$  and for a termolecular reaction the flux is  $kn(A)n(B)n(M)$ .  $\beta$  controls the temperature dependence of the rate coefficient  $\alpha$ .  $\gamma = \frac{E_a}{R}$  represents the energy barrier or activation energy  $E_a$  in units of K and  $R$  denotes the gas constant.  $\beta$  and  $\gamma$  are crucial in circumstellar chemistry as the temperature (and also the density) varies over a broad range and several orders of magnitude, thus largely deviating from standard condition ( $T = 298$  K and  $p = 1$  atm).

In order to determine the abundance change of the  $i$ -th species with time all reactions which either form or destroy species  $i$  are gathered together:

$$\frac{dn_i}{dt} = \sum_{j,k} k_{jk}n_jn_k + \sum_{j,k} k_{jkm}n_jn_kn_m + \sum_l k_l n_l - n_i \sum_m k_{im}n_m - n_i \sum_n k(n) \quad (35)$$

The first three terms sum up all bimolecular, termolecular, and unimolecular reactions leading to the formation of species  $i$ . These three terms are referred to as gain term. The last

three terms subtract all bimolecular, termolecular, and unimolecular reactions consuming or destroying species  $i$  (loss term).  $M$  represents the collision partner, and therefore the prevalent species in the gas, or just the total gas number density, as used in the formalism here.

The total number of ordinary differential equations (ODEs) is set by the number of species. As the flux of species  $i$  depends not only on its number density  $n_i$ , but also on the number density of species  $j$ ,  $n_j$ , the set of ODEs is highly coupled and must be solved simultaneously.

Experimental reaction rates available in the literature are used. The National Institute of Standards and Technology (NIST) provides a reaction rate database that includes more than 38'000 separate reaction records for over 11'700 distinct reactant pairs (NIST, 2000). Furthermore, the UMIST Database For Astrochemistry (UDFA) containing more the 6000 distinct reactions is used (McElroy et al., 2013), as a complement to the NIST database if necessary, although the UDFA database is more useful for the modelling of low gas temperature environments, such as dense molecular clouds in the Interstellar Medium. For reactions for which no laboratory measurement exist at all, theoretically derived rates obtained with Rice-Ramsperger-Kassel-Marcus (RRKM) quantum calculations are used. The RRKM theory is a micro-canonical theory of transition states. Some reactions lack a rate expression. In such cases, educated guesses are made. Educated guesses are obtained by computing the enthalpies and the GFE of reaction, respectively, for given temperatures and pressures. Reactions with a negative change of the reaction enthalpy ( $\Delta H < 0$ ) are exothermic reactions, which release energy in the form of heat. Reactions with a positive change of the reaction enthalpy ( $\Delta H > 0$ ) are endothermic reactions, which consume energy in the form of heat and cools the ambient gas. Moreover, reactions, which occur spontaneously, are called exergonic and have a negative change of the GFE ( $\Delta G < 0$ ). Conversely, reactions with a positive change of the GFE ( $\Delta G > 0$ ) are called endergonic and do not proceed spontaneously. GFE and enthalpy are related by the entropic change (see Equation 26). For example, a relative high, flat and barrierless reaction rate is ascribed to an exotherm and exergonic process. In contrast, an endergonic and endothermic reaction is described by a low reaction rate with an activation barrier  $E_a$  that corresponds to roughly to  $\Delta G_R$ .

The GFE and the heats of reaction therefore render an idea of the reaction speed i.e. whether a reaction occurs fast and spontaneously, or has an activation energy barrier (activation temperature). Often only forward rates are known, and data about reverse process is lacking. In such a case, the reverse rate  $k_r$  can be estimated by the assumption of micro-reversability (Cherchneff et al., 1992),(Willacy & Cherchneff, 1998):

$$k_r = AT^n C^{\Delta\nu} \exp \frac{\Delta G_R - E_a}{RT} \quad (36)$$

where  $A$ ,  $n$  and  $E_a$  are the Arrhenius parameters of the forward rate,  $C = \frac{N_A 10^6}{RT}$ ,  $\Delta G_R$  the GFE of reaction, and  $\Delta\nu$  correspond to the change in reaction order. In the framework of this thesis, the micro-reversability is used to estimate the rate pre-factors  $A$  of some (backward) cluster reactions. However, micro-reversability relies on TE conditions and in this



thesis, reverse reactions are rather estimated by thermo-chemical considerations. Activation barriers for both, forward and reverse reaction, indicate that an intermediate compound is involved.

The chemical network used in the framework of this thesis contains 105 species and 430 reactions involving neutral-neutral, thermal fragmentation, collisional dissociation and radiative association reactions, respectively. Ions are excluded, as AGB stars are too cool to generate ionizing stellar UV photons, and the interstellar UV photons are not able to penetrate sufficiently deep in the circumstellar envelope. We use different cluster formation and destruction rates for  $R \geq 3.5 R_*$  and for  $R < 3.5 R_*$  as most of cluster formation processes become barrierless and exergonic for the conditions around  $3.5 R_*$ , (i.e. the GFE of reaction  $\Delta G_R^0$  changes its sign).

In the models with low photospheric densities ( $n_0 \sim 10^{13} \text{cm}^{-3}$ ) and low scale heights (SRb model), it may happen that atomic hydrogen becomes more abundant than molecular hydrogen ( $f(\text{H}) > f(\text{H}_2)$ ) and the periodic shock solution of BC85 breaks down.

In such a case the termolecular  $\text{H}_2$  formation processes, which are improbable to occur at low densities cannot compensate the  $\text{H}_2$  dissociations anymore.

In order to overcome this problem, which appears in the SRb and low density models, the  $\text{H}_2$  abundance is frozen by removing the  $\text{H} + \text{H} + \text{M} \leftrightarrow \text{H}_2 + \text{M}$  reactions at the radius where  $\text{H}_2$  stops to dominate (around 3-4  $R_*$ ).

The freezing is justified by observations as well as for chemical reasons. Observations of AGB inner envelopes suggest a molecular prevalence, rather than an atom-dominated gas (see e.g. Habing & Olofsson (2003)). A transition from  $f(\text{H}_2)/f(\text{H}) > 1$  to  $f(\text{H}_2)/f(\text{H}) < 1$  would drastically effect the complete chemistry.

## 4.5 Post-Shock Chemistry

As mentioned in Section 3, the post-shock structure is divided into two zones: the immediate shock zone and the adiabatic parcel excursion as seen in Figure 14, where the abundances of  $\text{H}_2$  and  $\text{H}$  are plotted against time. In the immediate shock zone  $\text{H}_2$  is essentially dissociated, whereas it reforms in the adiabatic parcel of the post-shock gas.

The complete chemical network was used to describe the chemistry in both zones. The network contains 105 species and 426 reactions, which translates in a set of 105 stiff, coupled, ordinary differential equations (ODEs). The form of the differential equation has been motivated and presented in the previous subsection. This subsection is concerned with the stiffness and the coupling of set of ODEs. In this context, stiffness accounts for the various and distinct timescales imposed by the reactions included in the network and the changes in gas parameters as well. On the one hand, stiffness constrains the time step to a small interval, on the other hand, it sets priorities to fast reactions. As post-shock gas temperature and density are changing with time, the dominant processes may change owing to different gas conditions, or changes in the reactant number densities, as illustrated in Figure 14. In every integration time step, the species fluxes are thus evaluated and the dominant reactions

Table 9: Chemical species and dust clusters included in the IK Tau chemical model.

Atoms	Molecules				
O	OH	H <sub>2</sub> O	O <sub>2</sub>	CO	CO <sub>2</sub>
C	CH	CS	CN	HCN	OCS
H	H <sub>2</sub>				
Si	SiO	SiO <sub>2</sub>	Si <sub>2</sub>	HSiO	
S	SH	H <sub>2</sub> S	SiS	SO	SO <sub>2</sub>
N	NH	NH <sub>2</sub>	NH <sub>3</sub>	N <sub>2</sub>	NO
P	PH	P <sub>2</sub>	PO	PN	
Mg	MgH	MgO	MgOH		
Fe	FeH	FeO	Fe <sub>2</sub>		
F	HF	F <sub>2</sub>			
Al	AlO	AlH	AlOH	Al <sub>2</sub>	AlCl
Na	NaH	NaCl			
Cl	HCl	Cl <sub>2</sub>	ClO		
Ca	CaO	CaOH	CaCl		
K	KH	KCl			
Ti	TiO	TiO <sub>2</sub>			
Dust clusters					
SiO <sub>2</sub>	Si <sub>2</sub> O <sub>2</sub>	Si <sub>2</sub> O <sub>3</sub>	Si <sub>3</sub> O <sub>3</sub>	Si <sub>4</sub> O <sub>4</sub>	
H <sub>2</sub> SiO	H <sub>2</sub> Si <sub>2</sub> O <sub>2</sub>	HSi <sub>2</sub> O <sub>3</sub>	H <sub>2</sub> Si <sub>2</sub> O <sub>3</sub>	H <sub>2</sub> Si <sub>2</sub> O <sub>4</sub>	
MgSi <sub>2</sub> O <sub>3</sub>	MgSi <sub>2</sub> O <sub>4</sub>	MgSi <sub>2</sub> O <sub>5</sub>	MgSi <sub>2</sub> O <sub>6</sub> H <sub>2</sub>	Mg <sub>2</sub> Si <sub>2</sub> O <sub>4</sub>	Mg <sub>2</sub> Si <sub>2</sub> O <sub>5</sub>
Mg <sub>2</sub> Si <sub>2</sub> O <sub>6</sub>	Mg <sub>3</sub> Si <sub>2</sub> O <sub>5</sub>	Mg <sub>3</sub> Si <sub>2</sub> O <sub>6</sub>	Mg <sub>3</sub> Si <sub>2</sub> O <sub>7</sub>	Mg <sub>3</sub> Si <sub>2</sub> O <sub>8</sub> H <sub>2</sub>	Mg <sub>4</sub> Si <sub>2</sub> O <sub>6</sub>
Mg <sub>2</sub> Si <sub>2</sub> O <sub>7</sub> H <sub>2</sub>	Mg <sub>4</sub> Si <sub>2</sub> O <sub>7</sub>	Mg <sub>4</sub> Si <sub>2</sub> O <sub>8</sub>			
Al <sub>2</sub> O	AlO <sub>2</sub>	Al <sub>2</sub> O <sub>2</sub>	Al <sub>2</sub> O <sub>3</sub>	Al <sub>4</sub> O <sub>6</sub>	
Al <sub>2</sub>	Si <sub>2</sub>	Fe <sub>2</sub>			

are identified. The Jacobian, pertaining to the set of coupled ODEs, is generated internally by the solver Livermore Solver for Ordinary Differential equations (LSODE) (Hindmarsh, 1980). LSODE makes use of backwards differentiation formulas to solve the stiff system of equations. The solver thus uses an implicit method to calculate the total species flux. Implicit methods have the advantage that they do not suffer from numerical instabilities appearing in explicit methods. However, implicit methods require matrix inversion at each integration step and can be computationally expensive, which is the case for our calculations, for which a  $105 \times 105$  non-sparse Jacobian matrix needs to be inverted.

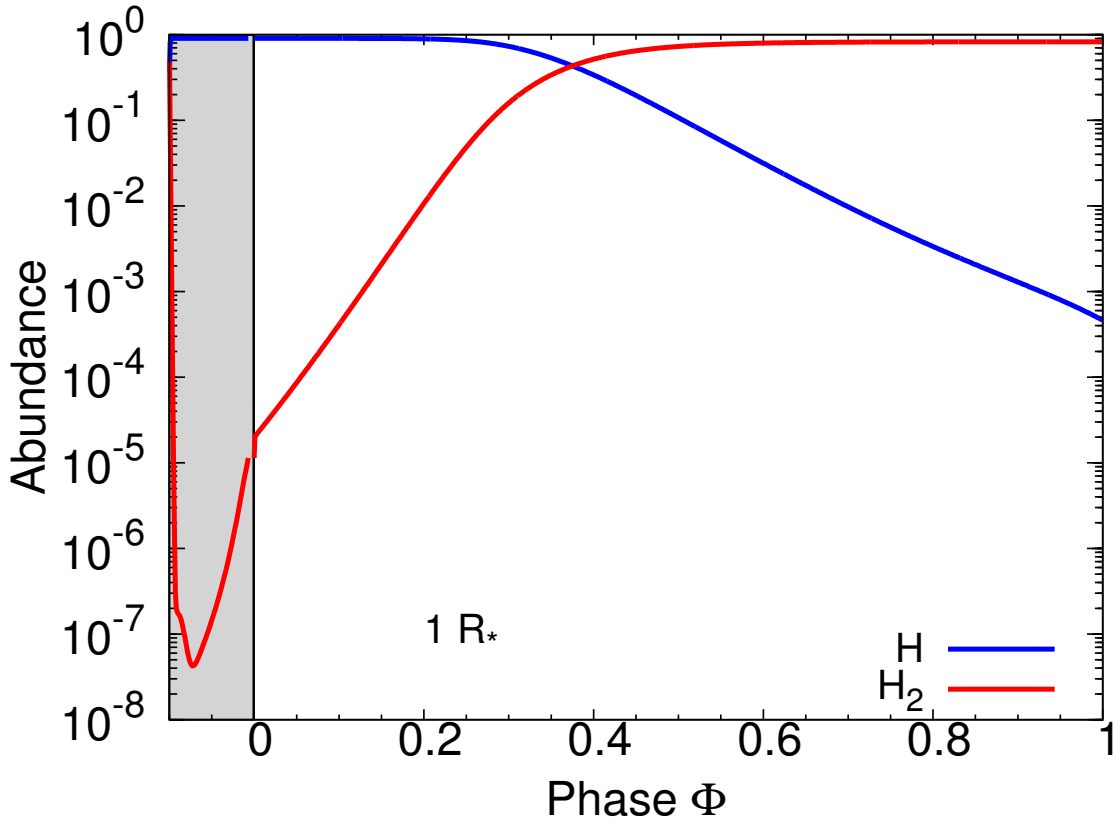


Figure 14: Abundances of atomic H and molecular H<sub>2</sub> at  $1R_*$  in the post-shock gas as function of the pulsation phase. The grey-shaded area corresponds to the immediate shock layer and the white region to the deceleration region.

## 4.6 Cluster Structures

Clusters are the molecular building blocks of dust grains. Hitherto dust formation in oxygen-rich AGB stars is assessed by Classical nucleations theory (CNT), by TE, or by a combination of both (Ferrarotti & Gail, 2006). But CNT fails in predicting structures and properties of chemical compounds with sizes below  $50\text{\AA}$ . In this regime, strong deviations are expected (and found) from bulk-like orientations and properties (Goumans & Bromley, 2012), (Woodley, 2011). Bulk properties and concepts are unappropriated to molecular

clusters, as they rely on periodic lattice structures with periodic potentials. In molecular clusters, however, there is lattice confinement and the atoms, that constitute a cluster, are often located at the cluster edge. Quantum confinement thus strongly affects the characteristics of nano-particles. It is thus reasonable and appropriate to concern this problem by a bottom-up approach.

Stable electronic structures are given by the solution of the time-independent Schrodinger equation, which only yields exact solutions for the hydrogen atom and the  $H_2^+$  ion with a well-defined  $\frac{1}{r}$ -potential. For many-body quantum systems like molecules and clusters, the ground-state wave function and energy can only be determined numerically. In this study, clusters of alumina  $(Al_2O_3)_n$ ,  $n = 1 - 4$ , silicates (enstatite  $(MgSiO_3)_n$ ,  $n = 1, 2$  and forsterite  $(Mg_2SiO_4)_n$ ,  $n = 1, 2$ ) are investigated. Such dust clusters are carriers of several interstellar bands (e.g. the  $9.7\mu m$ ) which are observed around oxygen-rich stars and are thus of astronomical importance.

We focus on obtaining the most stable isomers, i.e. the ground and first excited states. The search for the ground-state of a given cluster size and composition is a global optimisation problem. The bigger the number of atoms in the cluster, the greater is the number of possible arrangements. As the number of structural isomers scales exponentially with the number of constituent atoms, a cluster of ten atoms would have millions of distinct isomers. A complete quantum-mechanical density functional theory investigation of all possible structures would require an enormous amount of CPU hours and is nowadays limited to small cluster sizes. Density functional theory (DFT) is a procedure to determine the ground state of a quantum-mechanical many-electron-system. It is based on the position-dependent electron density and renders basic characteristics (i.e. structures, bonding lengths and energies) of molecules and solids.

In order to reduce the computational effort, stable candidate structures are assessed by a pre-selection method. Such candidate structures are obtained by a Monte-Carlo based search, in which only classical interactions and no quantum forces are evaluated and iterated. To efficiently explore the complex parameter space, initial structures are generated by applying simple inter-atomic potentials:

$$V(r_{ij}) = \frac{q_i q_j}{r_{ij}} + A \exp\left(-\frac{r_{ij}}{B}\right) - \frac{C}{r_{ij}^6}, \quad (37)$$

where  $q_i$  and  $q_j$  are the charges of atom  $i$  and  $j$ , respectively.  $r_{ij}$  is the relative distance between point charge  $i$  and  $j$ .  $A$ ,  $B$  and  $C$  are inter-atomic potential parameters specific to the atom species, which can be extensively found in the literature. The first term is the Coulomb interaction between cations ( $Al^{3+}$ ,  $Mg^{2+}$ ,  $Si^{4+}$ ) and anion ( $O^{2-}$ ) and is hence attractive. The last term accounts for the van-der-Waals interaction which is also attractive. To prevent a collapse/fusion of the two point charges into a singularity, the so called Born-Mayer (BM), term is included. Physically spoken, BM accounts for the fact that two atoms cannot reside in the same location (Pauli's exclusion principle). The BM term acts on short relative distances ( $r_{ij} \leq B$ ) and is repulsive. The second and third term in the above

equation are also referred to as the Buckingham potential. The values for A, B and C for the Al-O, O-O and Mg-O interaction are derived from bulk material and can be extensively found in the literature (Woodley, 2009).

Electric polarization is characterised by a non point-like charge distribution and affects the above potential. To account for polarisation, the point charge assumption is relaxed. The more realistic shell model in which point charges are split into two partial charges, is applied: one charge for the nucleus including the electrons of the *inner* shells and one charge accounting for the outer-shell electrons. For example, the  $O^{2-}$  inner charge is reduced by a factor of 0-20 % and assigned to the outer shell charge.

The Monte-Carlo Basin-Hopping (MCBH) global optimisation method involves inter-atomic or interionic pair potentials (given by equation 37), varying initial geometries, bond lengths, and containing boxes (maximal sizes of the clusters). According to these criteria, candidate structures are generated. As a result, millions of possible configurations have been reduced to hundreds. On average, the 50 most promising (low-lying and recurrent) clusters are further optimized with DFT at the B3LYP/6-311+G\* level, where B3LYP represent the used functional, 6-311+G\* denotes the underlying basis set, which consists of 6 basis functions including diffusive term and recoil of nuclei.

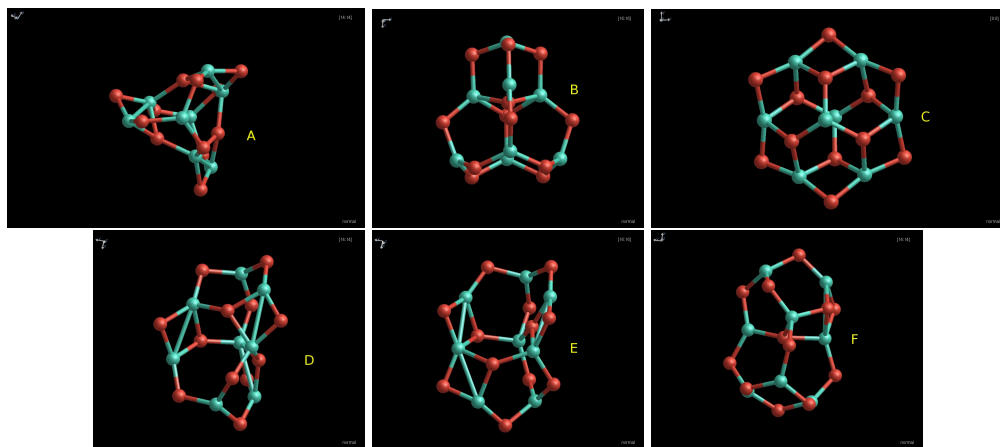


Figure 15: The six lowest-energy alumina tetramers  $Al_8O_{12}$  with energies relative to the ground state 0.00 (A), 0.12 (B), 0.19 (C), 0.26 (D), 0.27 (E) and 0.29eV (F).

Inspection of the previously generated initial structures on the quantum level yields electronic, thermal, vibrational, rotational and zero-point energies. The latter arise, as the cluster is considered as a quantum mechanical harmonic oscillator. Furthermore, frequencies of vibrational modes and rotational constants are obtained. The optical properties, i.e. the spectra of the vibrational transitions and their related intensities, differ from isomer to isomer. In the context of astronomical observations, the IR spectra not only tell us about the dust carrier itself, but also about its geometric structure. The latter also hints at possible formation pathways.

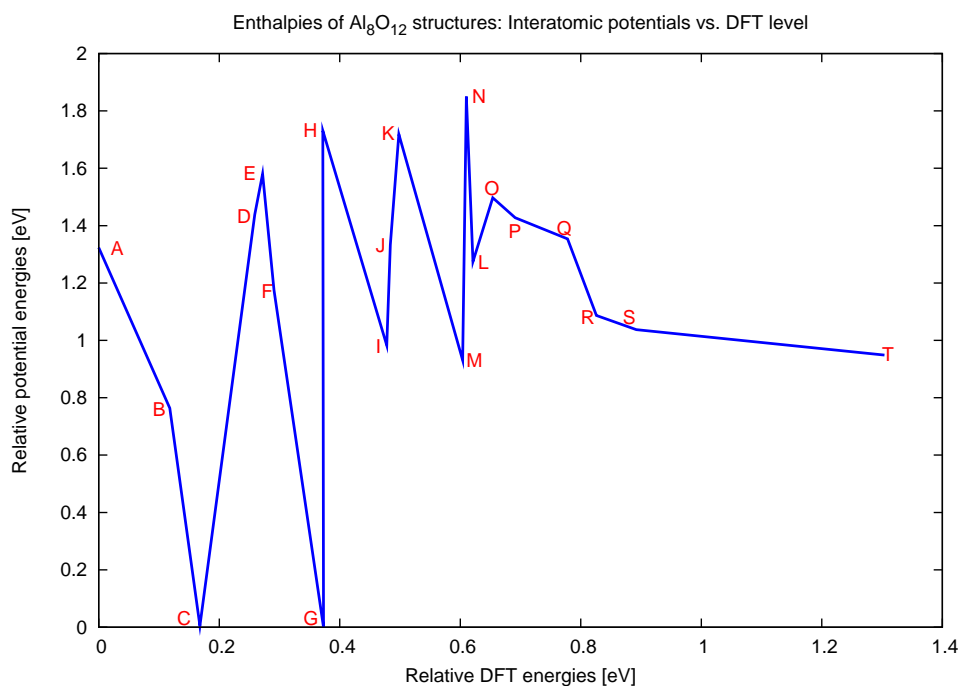


Figure 16: Comparison of inter-ionic potentials cluster energies and energies at the B3YLP density functional theory level for distinct  $Al_8O_{12}$  structures. Obviously the energetic order is not preserved. Nevertheless the Monte-Carlo-Basin-Hopping method with pairwise ionic potentials yields a good and complete set of initial structures. The capital letters  $A, B, ..$  denote distinct structures.

The DFT computations are performed for standard conditions ( $T = 298 \text{ K}$ ,  $p = 1 \text{ atm}$ ). However, rather hot ( $\sim 2000\text{K}$ ) and dilute conditions prevail in circumstellar environments. Furthermore, the astrophysically relevant thermodynamic energy, the GFE, which determines whether a chemical process is energetically favorable, differs significantly. The GFE can be split into an enthalpy part and an entropy part as done in equation 26. The latter can be large in condensation processes, as translational entropy of reaction is lost, which is only partially compensated by an increase in the rotational and vibrational entropy (Goumans & Bromley, 2012).

The GFE of the ground-state and low-lying clusters can be expressed in terms of the partition function (PF) and its derivatives. The partition function itself results from translational, electronic, vibrational and rotational motion contributions. Vibrational frequencies, rotational constants and split up energies are used to calculate the contribution from each component. For a given equilibrium pressure and temperature, the GFE of formation is finally determined.

The GFE results are used to derive trends for the cluster reactions of interest and for post-shock gas conditions. Therefore, reaction rate expression for specific cluster reactions and gas conditions can be assessed. In the following the more general cluster considera-

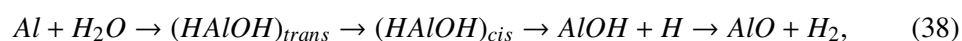
tions will be specified to alumina and silicate clusters.

## 4.7 Gas-Phase Nucleation

### Alumina

The gas phase molecules entering the formation of alumina clusters are AlO and AlOH. The radical AlO has been detected at millimetre (Tenenbaum & Ziurys, 2009), (near)-infrared (Banerjee et al., 2003) and optical wavelengths (Kamiński et al., 2013) in the red supergiant VY CMa and its observational abundance (relative to H<sub>2</sub>) is  $x(\text{AlO}) \sim 6 \times 10^{-9}$  (Tenenbaum & Ziurys, 2010). The abundance of AlOH is  $x(\text{AlOH}) \sim 1 \times 10^{-7}$  at a distance of  $22 R_*$  from the star (Tenenbaum & Ziurys, 2010). The authors argue that AlOH is likely formed just above the photosphere via TE chemistry and disappear due to dust condensation. This same arguments holds also for aluminum oxide as they find that the AlO emission is centered at the intrinsic stellar velocity and its derived rotational temperatures indicate an origin within  $20 R_*$ , i.e. the *inner* envelope. Furthermore, aluminium hydroxide AlOH is by a factor of 17 more abundant than AlO in VY CMa. The maximum abundance of AlCl has been evaluated to  $5 \times 10^{-8}$ . Recently Kaminski et al. (2013) confirmed the presence of AlCl by its rotational fingerprint in the spectra of VY CMa without specifying an abundance. Other than AlO, AlOH, and AlCl, no aluminum-bearing species in oxygen-rich envelopes has yet been detected. They may be not detectable, as most of AlO and AlOH goes into dust and thus little evidence for aluminum-related gas-phase chemistry is provided.

The gas-phase precursors of alumina dust are thus most likely AlO and AlOH. Both of these species are produced (among other reactions) during a complex 4 step reaction of elemental Al with H<sub>2</sub>O (water):



where  $(\text{HAlOH})_{\text{trans}}$  and  $(\text{HAlOH})_{\text{cis}}$  represent the the trans and cis stereoisomers of the intermediary molecular compound. This 4-step reaction was studied by Sharipov et al. (2011). In previous studies, it was often assumed that the Al+H<sub>2</sub>O reaction proceeds directly to AlO + H<sub>2</sub> depending on the branching ratio. The study of Sharipov et al. (2011) clearly demonstrated, that a direct reaction  $\text{Al} + \text{H}_2\text{O} \rightarrow \text{AlO} + \text{H}_2$  is impossible and that the reported rate  $\text{Al} + \text{H}_2\text{O} \rightarrow \text{products}$  measured by McClean et al. (1993) must be associated with the  $\text{Al} + \text{H}_2\text{O} \rightarrow \text{AlOH} + \text{H}$  reaction path only. The transition from trans to cis configuration is very fast and assumed to occur instantaneously. The process of direct HAlOH formation was found to be negligible at a pressure smaller than  $p = 100$  atm and thus quickly decomposes to AlOH+H, under circumstellar gas conditions.

Furthermore, Swihart et al. (2003) linked the molecules AlO and AlOH to the chlorine family by reactions with the species AlCl, AlH and HCl. The experimentally studied (and partially estimated) rates are use in the chemical network. Catoire et al. (2003) gave some reaction rates involving Al<sub>2</sub>O, AlO<sub>2</sub>, Al<sub>2</sub>O<sub>2</sub> and Al<sub>2</sub>O<sub>3</sub> clusters, which are important in-

intermediaries for alumina formation. Specifically, the thermal stability (i.e. energy barrier for the dissociation of these species) is given. According to their kinetic model,  $\text{AlO}_2$  is formed by the reactions  $\text{AlO} + \text{CO}_2$  and  $\text{AlO} + \text{O}_2$  thus water does not play a role for the  $\text{AlO}_2$  formation. Moreover, the  $\text{AlO}$  formation itself seem to proceed via  $\text{CO}_2$ ,  $\text{O}_2$  as well. In conclusion, it can be stated that  $\text{AlOH}$  formation processes are related to water, whereas other mechanisms are responsible for the  $\text{AlO}$  and  $\text{AlO}_2$  formation. In addition to these studies, theoretical investigations have been conducted towards  $\text{Al}_x\text{O}_y$ ,  $x,y=1-4$  (Patzer et al., 2005). This thesis confirms the structures and energies of these clusters by reproducing the clusters on the same level of DFT calculations.

In the past decades, experimental and theoretical efforts towards pure aluminum clusters or so called pure Al superatoms have been undertaken. As the binding energy per atom increases with cluster size  $n$  (up to a certain size) the clustering of Al atoms is an energetically favourable process. Therefore, the formation of the smallest of these clusters,  $\text{Al}_2$ , is included in the chemical-kinetic network and the temperature-dependent, termolecular formation rate is taken from Li & Truhlar (2008).

The 20 lowest-energy alumina clusters reported by Li & Cheng (2012) have been well reproduced by up to a size of  $n = 4$  and represented in Figure 15).

## Silicates

For silicates (here: enstatite and forsterite), the situation is different than for alumina. Silicates are made of at least three distinct atomic species (O, Mg, and Si) and are mostly ternary oxides. Stable gaseous silicate monomers do not exist and thus cannot nucleate.

Furthermore, extensive computational studies show that pure (homomolecular)  $\text{SiO}$  nucleation to  $(\text{SiO})_n$ ,  $n=3,4,5,\dots$  is unlikely under hydrogen-rich gas conditions. Once  $(\text{SiO})_n$  reaches a certain size, the clusters decompose to pure silicon  $(\text{Si})_n$  and silica  $(\text{SiO}_2)_n$  (Cherchneff & Dwek, 2010).

A formalism comprising multiple gas phase species (heteromolecularity) and multiple nucleation steps are required to describe cluster formation. In addition, only very exothermic reactions ( $\Delta H_r \ll 0$ ) can occur. The reason lies in the huge entropy loss during the nucleation processes heavily impacting the GFE of reaction:

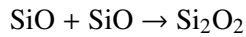
$$\Delta G_r = \Delta H_r - T\Delta S_r \quad (39)$$

where  $T\Delta S_r$  is of the order of 200-300 kJ/mole for a typical cluster reaction.

For silicate clusters in AGB stars a heteromolecular nucleation and growing scheme has been proposed by Goumans & Bromley (2012) (see Figure 17). This scheme involves the oxidation and metal inclusion of clusters and starts from the gas phase molecules  $\text{SiO}$ ,  $\text{H}_2\text{O}$ , and  $\text{Mg}$ , which are part of the detailed chemistry used in this thesis. This allows a direct implementation of the steps as illustrated in Figure 17 in the chemical network. In the following steps 1-7 will be described and in detail:

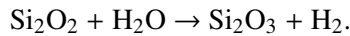


1. The first step is the dimerisation of the SiO molecule:



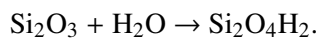
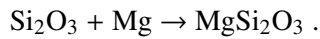
This process is energetically uphill and represents a bottleneck in the enstatite dimer formation. Moreover, the dimerisation may occur rather by collisions with the ambient gas ( $\text{SiO} + \text{SiO} \rightarrow \text{Si}_2\text{O}_2 + \text{M}$ ) than by radiative association. The termolecular formation rate,  $k_f = 1 \times 10^{-33} \exp(2858.0K/T)$ , is very slow. Therefore, collisional dimerisation is a three-body process, which is only relevant at high densities. Both dimerisation processes are implemented in the chemistry. Reactions leading to Mg-SiO or  $\text{SiO}_2$  are even less probable owing to even higher energy barriers of the order of 100 kJ/mole.

2. Once the SiO dimer,  $\text{Si}_2\text{O}_2$ , has formed, the oxidation by  $\text{H}_2\text{O}$ , which is available from the gas phase, occurs:



It is also possible that the adduct,  $\text{H}_2\text{Si}_2\text{O}_3$ , forms without ejecting  $\text{H}_2$ . This adduct will be important (see below). The metallic Mg inclusion however requires a large amount of energy and can be neglected.

3. In this subsequent step a branching in the enstatite / forsterite formation pathway occurs: One branch involves a Mg incorporation, the other branch an oxidation by  $\text{H}_2\text{O}$ . Goumans & Bromley (2012) revealed that generally oxidations before Mg incorporations are favoured. However, clusters can also be overoxidised by water and form hydroxyl groups:



Note that the calculation of the thermochemistry (i.e. the GFE potentials) depend on pressures and temperatures, respectively. Goumans & Bromley (2012) performed  $T = 1000$  K and  $p = 0.1$  Pa. In the pulsation model applied here the gas experience a large range of pressures and temperatures. The thermochemical potentials thus need to be evaluated not only at one T and P, but at several gas conditions representing distinct envelope positions.

The SiO dimerisation is the initial step in the silicate cluster formation, . The termolecular formation of the dimer  $2 \text{SiO} + \text{M} \rightarrow \text{Si}_2\text{O}_2 + \text{M}$  is only efficient at high densities. It is thus expected to occur close to the star and at early phases where high densities prevail. On the other hand the termolecular rate has a negative temperature dependence (i.e. the rate decrease with increasing temperature) (Zachariah & Tsang, 1993). The SiO dimerisation is therefore inefficient at high temperatures. Consequently, close to the star the reaction is hampered by high temperatures and further out by too low number densities and silicates cannot form. However, observation clearly prove the presence of silicates in oxygen-rich AGB envelopes.

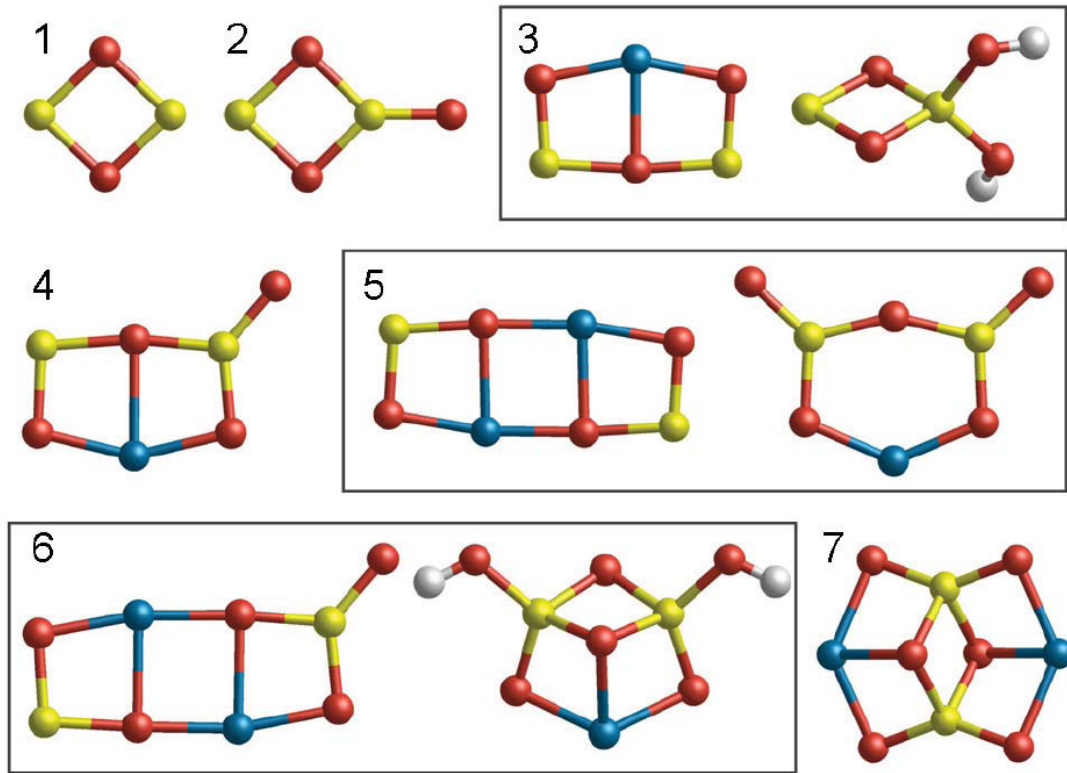
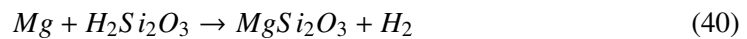


Figure 17: Silicate cluster nucleation scheme according to Goumans & Bromley (2012). The color code of the atoms are the following: Si: yellow, O: red, Mg: blue, H: white. The numbers correspond to the step numbers from  $2 \text{ SiO} \rightarrow \text{Mg}_2\text{Si}_2\text{O}_6$ .

The inclusion of silaformyl radicals and silanone in the cluster formation pathway provides a solution to this problem. Silaformyl radicals are molecules with the functional group Si-O-H and the general form  $\text{Si}_x\text{O}_y\text{H}_z$  with  $x, y, z = 1, 2, 3, \dots$ . A silanone is the silicate analogue to a ketone and is characterised by a double bonding between Si and O atoms (Si=O). and have been investigated by Zachariah & Tsang (1995).

The authors investigated the formation of silica,  $\text{SiO}_2$ , in a hydrogen-rich environment, and found that silanone and silyformyl radicals are crucial intermediaries of the formation process.

In the chemical reaction network used here the species  $\text{HSiO}$ ,  $\text{H}_2\text{SiO}$ ,  $\text{H}_2\text{Si}_2\text{O}_2$ ,  $\text{H}_2\text{Si}_2\text{O}_3$  are included. The corresponding reactions are listed in Table silaformyl. The formation reactions are barrierless and thus have no temperature dependence. These species implicitly contain the dimer  $\text{Si}_2\text{O}_2$  and  $\text{Si}_2\text{O}_3$  in its hydrogenated form (namely  $\text{H}_2\text{Si}_2\text{O}_2$  and  $\text{H}_2\text{Si}_2\text{O}_3$ ). The molecular structures of  $\text{H}_2\text{Si}_2\text{O}_2$  and  $\text{H}_2\text{Si}_2\text{O}_3$  contain a small ring, analogue to  $\text{Si}_2\text{O}_2$  and  $\text{Si}_2\text{O}_3$ ) The latter species are coupled to the nucleation scheme of Goumans & Bromley (2012) by the reaction



which is described by the parameters  $\alpha = 1. \times 10^{-10} \text{ cm}^3\text{s}^{-1}$ ,  $\beta = 0$  and  $\gamma = 3000 \text{ K}$ . This single reaction (and its backward reaction) suffices to connect the new scheme and the

Table 10: Chemical reactions that enter the formation of silaformyl radicals and silanone adapted from Zachariah & Tsang (1995).

R1	SiO	+	H	$\leftrightarrow$	HSiO	
R2	SiO	+	H <sub>2</sub>	$\leftrightarrow$	HSiO	+ H
R3	HSiO	+	H	$\leftrightarrow$	H <sub>2</sub> SiO	
R4	HSiO	+	H <sub>2</sub>	$\leftrightarrow$	H <sub>2</sub> SiO	+ H
R5	H <sub>2</sub> SiO	+	H <sub>2</sub> SiO	$\leftrightarrow$	H <sub>2</sub> Si <sub>2</sub> O <sub>2</sub>	+ H <sub>2</sub>
R5	H <sub>2</sub> Si <sub>2</sub> O <sub>2</sub>	+	H <sub>2</sub> O	$\leftrightarrow$	H <sub>2</sub> Si <sub>2</sub> O <sub>3</sub>	+ H <sub>2</sub>

heteromolecular silicate nucleation scheme. This new nucleation route through silaformyl radical and silanone formation is based on the overabundance of hydrogen in AGB stars and its potential reaction with SiO. Furthermore, these molecules are isovalent to the formyl radical, HCO, and formaldehyde, H<sub>2</sub>CO. These species have been detected in carbon stars (Ford et al., 2004).

bypass not only avoids the dimersation bottleneck but also account for the fact that hydrogen overwhelmingly abundant in AGB atmospheres and may reaction with silicon oxides. In addition, silaformyls are isovalent to the species HCO and H<sub>2</sub>CO which have been detected in carbon-rich envelopes.

## 4.8 Coalescence and Condensation

The condensation formalism used in this thesis is based on the work of Saunders & Plane (2006) and Sarangi & Cherchneff (2014) and was initially developed to describe the condensation nuclei, responsible for cloud formation, light absorption and scattering, in the Earth's atmosphere. In the present model, the formation of the solid phase is coupled to the gas-phase chemistry and estimated at each integration time step over pulsations. In the present models, dimers of forsterite, Mg<sub>4</sub>Si<sub>2</sub>O<sub>8</sub>, and alumina, Al<sub>4</sub>O<sub>6</sub>, act as condensation nuclei, and consider both, the coalescence and coagulation of these dimers, to form dust grains. In a free-molecular regime, defined by the grain mean-free path in the gas being much larger than the grain size, the formalism is based on a Brownian formalism, which accounts for the scattering, collision, and coalescence of the grains through Brownian motion. Grains size distributions are then derived for silicates of forsterite and enstatite stoichiometry, and alumina.

The computational domain in this formalism refers to various sizes of the spherical grains, describing the time variation of the grain number densities. The discretisation is thus made over bins, which contain dust grains with a specific volume  $V$ . The time variation of the number density  $n$  of a grain with the specific volume(size)  $V$  is described by the integro-differential equation given by (Jacobson, 2005; Sarangi & Cherchneff, 2014):

$$\frac{dn_V(t)}{dt} = 0.5 \int_{V_0}^V \beta_{V-\bar{V},\bar{V}} n_{V-\bar{V}} n_{\bar{V}} d\bar{V} - n_V \int_{V_0}^{\infty} \beta_{V,\bar{V}} n_{\bar{V}} d\bar{V} \quad (41)$$

where  $V$  and  $V - \bar{V}$  are the volumes of the two coagulating clusters / grains,  $V$  the volume of the new, coagulated particle is the number density of grain with volume,  $n$  the number density of grains with volume  $V, V - \bar{V}$  or  $\bar{V}$ , and  $\beta$  the rate coefficient of the two colliding clusters / grains.

This master equation resembles the ODEs describing the time variation of gas phase species number densities, as seen in Section 4.4. The temporal change of a certain number density (in this case it is the number density of a dust grain with a finite volume) is described by a gain term minus a loss term. The factor one half appears in the gain term to avoid doubly counting contributions (i.e. grain A coagulates with grain B is the same as grain B coagulates with grain A). The rate coefficient, sometimes also called *collision kernel*, is a complex expression, which accounts for physical processes such as Brownian diffusion, gravitational collection, turbulent motions, and Van-der-Waals forces. The mentioned mean-free path assumption is satisfied in circumstellar envelopes, as the mean free path  $\lambda_{mfp}$ , which is inversely proportional to the number density, is way larger than a typical grain size.

In order to derive radii and volumes of the various dust grains, the first bin with the smallest grain volumes, i.e. the dimers, are considered. The grain radius of the largest dimers considered determine the volume and the mass of grains in the first bin. For doing this, we assume a uniform density of the bulk material for dust clusters. For alumina grains, a bulk density of  $3.95 \text{ g cm}^{-3}$  is used, while for forsterite, the bulk density is a bit lower ( $3.00 \text{ g cm}^{-3}$ ). As a consequence the alumina grain volumes and radii are smaller than the corresponding forsterite grains. The grain radius  $r_{gr}$  of the first bin containing only dimers is then:

$$r_{gr} = \sqrt[3]{\frac{3V_{gr}}{4\pi}} = \sqrt[3]{\frac{3m_{gr}}{4\pi\rho}} = \left\{ \begin{array}{ll} 2.74\text{\AA} & \text{for alumina} \\ 3.33\text{\AA} & \text{for forsterite} \end{array} \right\} \quad (42)$$

where  $m_{gr}$  is the mass of the grain,  $V_{gr}$  the volume of the grain, and  $\rho$  the bulk density of the material.

## 5 Results for IK Tau

### 5.1 Initial Photospheric Abundances

For initial elemental compositions in IK Tau, a photospheric C/O ratio 0.75 was adopted in order to compare the photospheric TE abundances with the results of Duari et al. (1999). However, the exact C/O ratio is unknown. From observations, the C/O ratio could be deduced, however, it would require the knowledge of every gaseous and dust component and their respective abundances. Therefore, theoretical input is used. The photospheric temperature used in this thesis is  $T_* = 2200$  K and thus 100 K higher than in Duari et al. (1999). On the other hand the density is by a factor of 10 smaller in this study ( $n_0=3.6 \times 10^{14}$ ). The differences arise mainly because of the distinct gas conditions (temperatures and densities) rather than elemental conditions and are mostly evened out in the post-shock non-equilibrium chemistry.

Table 11: Comparison of photospheric TE abundances at  $n_0=3.6 \times 10^{15}$  and  $T=2100$  K for a solar elemental composition (used by Duari et al. (1999)) and the photospheric TE abundance at  $n_0=3.6 \times 10^{14} \text{ cm}^{-3}$  and  $T=2200$  K for the FRUITY composition used in this thesis.

Species	TE (Duari 99)	TE (this study)
H	6.65(-2)	3.76(-1)
H <sub>2</sub>	6.52(-1)	4.83(-1)
Si	1.03(-8)	3.30(-8)
S	1.37(-5)	1.93(-5)
CS	1.32(-10)	9.41(-12)
SH	6.49(-6)	1.36(-6)
H <sub>2</sub> S	1.03(-6)	3.9(-8)
N <sub>2</sub>	8.05(-5)	1.01(-4)
HCN	4.37(-11)	3.07(-12)
CN	1.73(-13)	1.11(-13)
NH <sub>3</sub>	1.20(-10)	5.54(-12)
O	1.63(-7)	5.90(-6)
OH	2.3(-6)	1.11(-5)
H <sub>2</sub> O	1.86(-4)	1.01(-4)
CO	6.95(-4)	4.91(-4)
CO <sub>2</sub>	4.09(-8)	1.97(-8)
O <sub>2</sub>	1.99(-11)	5.20(-10)
SiO	4.28(-5)	4.57(-5)
NO	1.04(-9)	7.51(-9)
SO	2.18(-8)	2.10(-8)
OCS	5.37(-9)	5.97(-11)

## 5.2 Post-Shock Chemistry

In the immediate shock layer described in Section 3.2 molecules are dissociated by collisions with the ambient gas. This is in particular true for shocks close the photosphere ( $R=1-2 R_*$ ) and for  $H_2$ ,  $H_2O$  and  $CO$ . At  $3 R_*$  the shock strength has decreased significantly and the immediate shock layer hardly affects the molecular abundances. In Figure 19, fractional abundances are shown as a function of distance behind the shock front at  $1 R_*$ .

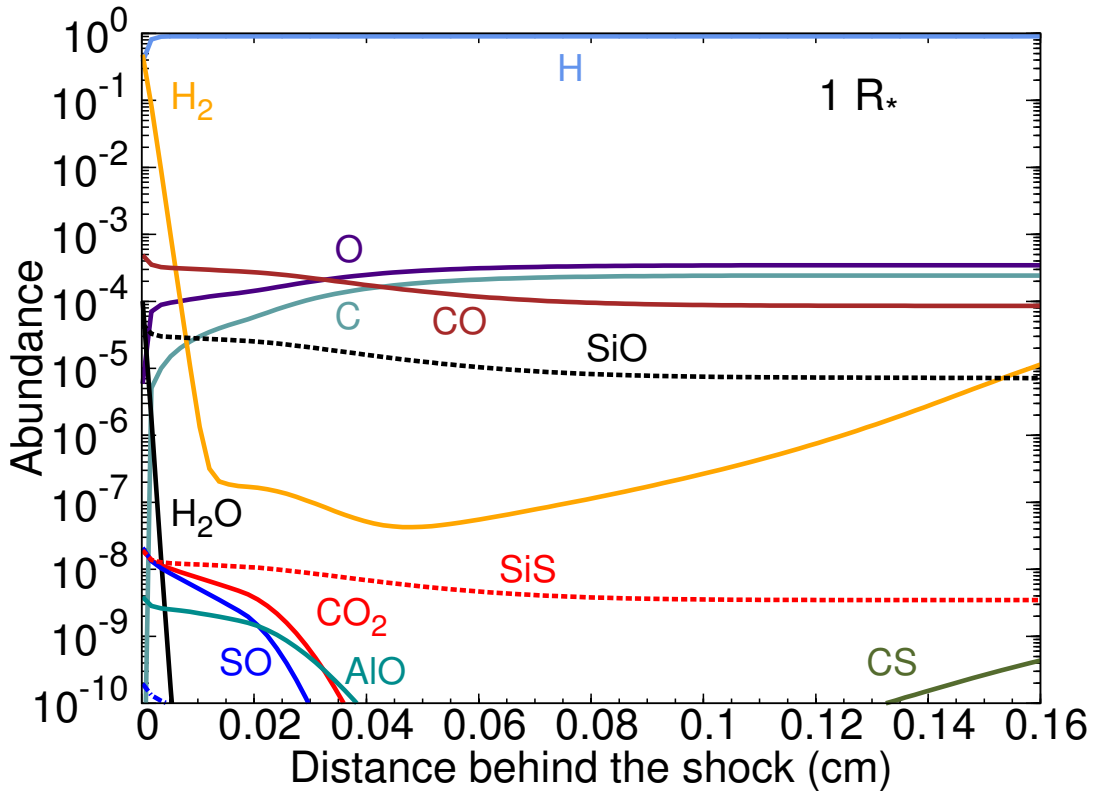


Figure 18: Abundances in the immediate shock layer at the photosphere ( $1 R_*$ ).

In Figures 18 and 19, the fractional abundances of the prevalent species in the immediate shock zone at  $1 R_*$  and  $3 R_*$  are shown. Figure 18 demonstrates, that the dissociation of the molecules occurs very early, where the gas conditions are given by the Rankine-Hugoniot jump conditions. The post-shock distances, over which  $H_2$  dissociation occurs, is very small. Such short dissociation lengths have already been highlighted in the models of Willacy & Cherchneff (1998) for the case of the carbon star IRC+10216.

As a consequence, the abundances of the elements rapidly increase in the beginning of the immediate shock layer. SiS, however, is almost unaffected in the immediate shock layer, and remains thus on almost constant abundance. SiO shows also little variation in the shock front. At  $3 R_*$ , the shock speed has decreased, and the molecular abundances stay on a roughly constant level. Only the elemental H, C, and O slightly increase in the beginning of the immediate shock zone.

In the parcels, where the gas cool adiabatically, the timescales are larger than in the immediate shock layer and the chemistry is very active. Figures 20 and 21 show the model

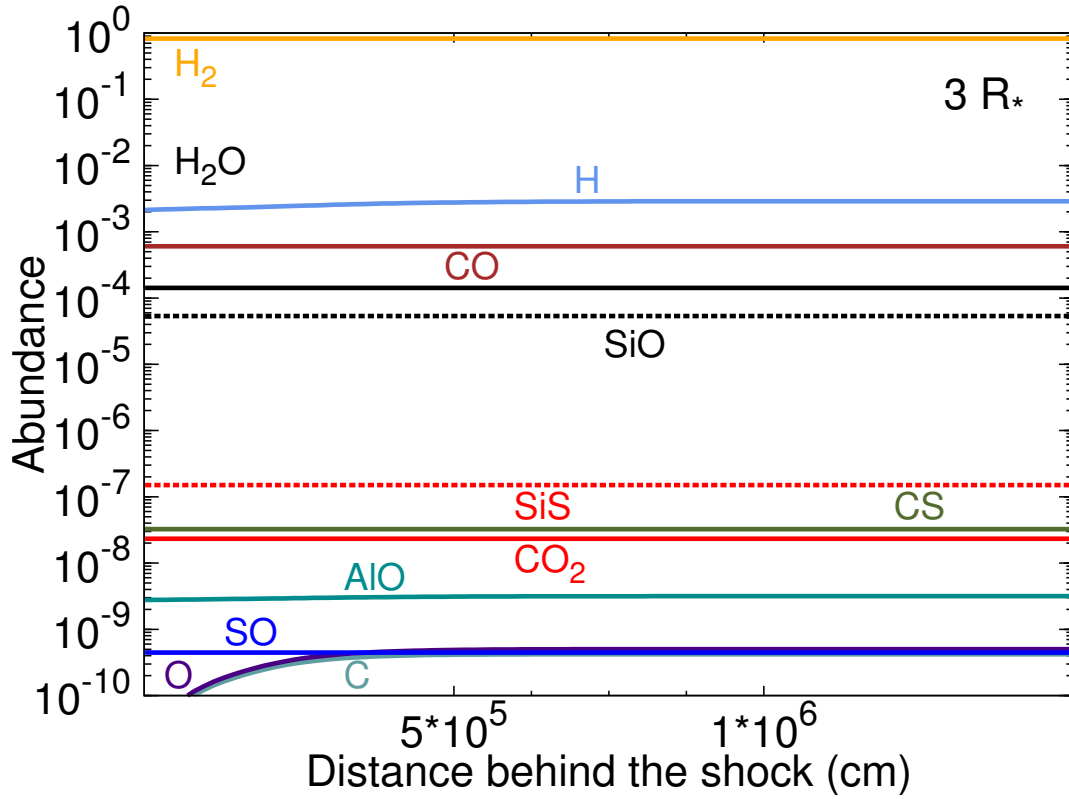


Figure 19: Abundances in the immediate shock layer at  $3 R_*$ .

results in the parcels at  $1 R_*$  and  $3 R_*$ .

The post-shock gas density and temperature decrease exponentially (see Figures 9 and 8) and molecules reform or recombine to form new molecular species.

Some species depend strongly on the post-shock chemistry thus varying their abundance significantly over a pulsation phase.  $H_2O$ , for example is dissociated to  $OH$  at early phases of the post-shock gas, but at later times  $H_2O$  reforms again (see Figure 21). The responsible reaction couple is



The forward rate has an energy barrier of  $E_a/R = 1660$  K, where  $R$  is the gas constant, and the backward reaction a barrier of  $E_a/R = 9720$  K. However, the backward rate has a pre-exponential factor  $A$  a 5 times higher than the forward rate (see Equation arrhenius). This implies that the backward reaction rate is higher at early phase and its suppression at late phase. In contrast, the forward rate is hampered at early phase and more efficient at late phase.

The same argument holds for  $AlOH$ ,  $AlO$  or  $CO_2$ .  $CO_2$  forms predominantly by the reaction



This reaction has a activation barrier of only  $E_a/R = 2630$  K. Its reverse reaction has a

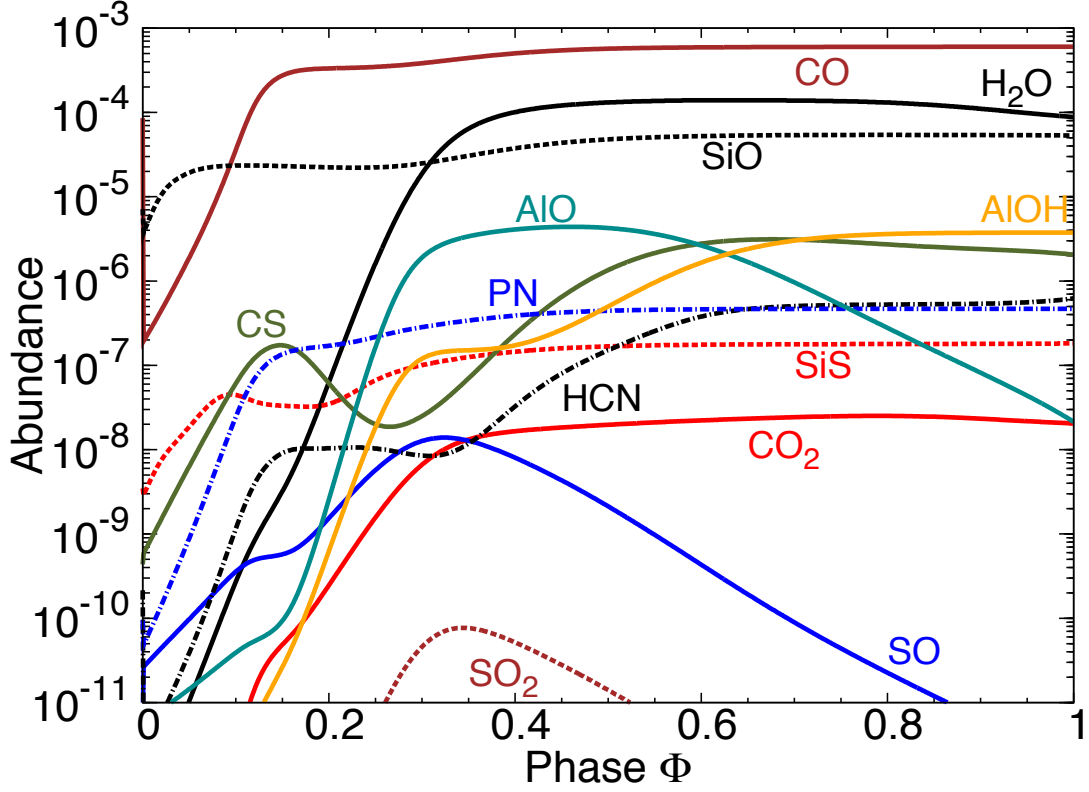


Figure 20: Abundances of the prevalent molecules in the parcel excursion at the photosphere ( $1R_*$ ).

pre-exponential rate factor a hundred times larger, but an activation barrier of  $E_a/R = 13230$  K. As a consequence the CO and OH are produced at early phase and high temperatures and  $\text{CO}_2 + \text{H}$  form at later phase where temperatures decrease and strongly suppress the reverse reaction.

The effect of shocks is less pronounced for CO or SiO, though it is important to the complete chemistry. Other molecules are not much affected by the passage of shocks (PN, SiS). These species experience not such complex chemistries owing to the following reasons. Their chemistry is not well characterised due to the lack of laboratory experiments and theoretical investigations. Moreover, these species are not that strongly coupled to the hydrogen chemistry, which is crucial in AGB envelopes. In the case of phosphorus species, it is the poorly characterised chemistry (see Section 5.4).

The majority of the molecule reform in the cooling post-shock gas and thus their abundances increase. This is the case for CO,  $\text{H}_2\text{O}$ , SiO, AIOH, HCN, PN and SiS. However, some species (AIO, SO,  $\text{SO}_2$ , CS) start to reform, but their abundance decrease again for phases  $\Phi > 0.5$ . The reasons for such an abundance curve will be explained in the following. The abundance of AIO decreases at the end of the parcels, owing to AIOH formation and alumina dust formation, SO and  $\text{SO}_2$ , which are strongly coupled (see Section 5.3), are predominantly formed by the following reaction





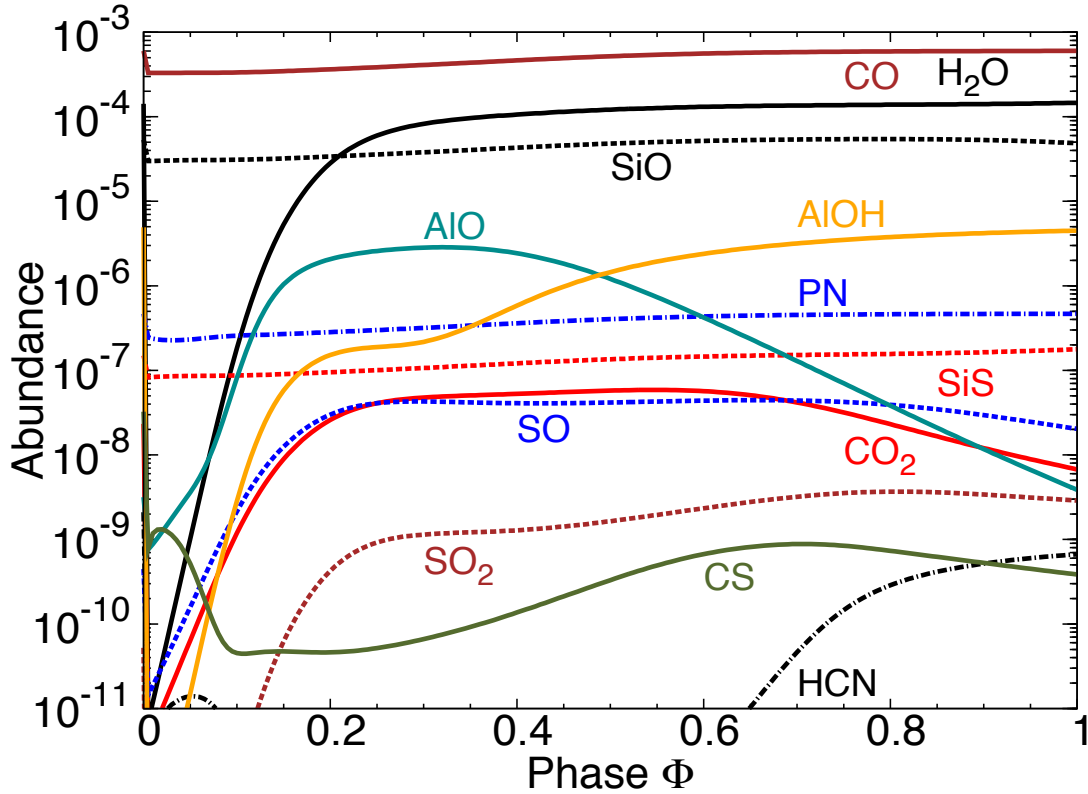


Figure 21: Abundances of the prevalent molecules in the parcel excursion at  $3R_*$ .

and a reaction involving  $SO + H$  (which is not the reverse reaction) is responsible for the decrease of the sulphur oxides at late phases:



The abundance CS, being subject to carbon and sulphur chemistry, shows an unusual curve in the parcels, as can be seen in Figures exIKtau1 and excursionIKtau. This means that, CS is involved in a complex chemistry, which cannot be reduced to a few dominant processes. The decrease of CS at late phase is marginal, and is related to the increase of CN and HCN.

In Table 12, the prevalent molecules, which have been observed around IK Tau, are listed. Furthermore, the model abundances close to the star ( $1 R_*$ ) and at  $6 R_*$  are compared to the most recent observations. The model abundances at  $6 R_*$  are considered as characteristic inner wind abundances, as a significant amount of dust has already formed, but the wind is not fully accelerated yet. To illustrate the reproduction and predictions of molecules in the present model, Figures 22 and 23 represent the model finding graphically. The modelled CO abundance is by a factor of 5-7 higher compared to observations, albeit it is lower than the TE abundance (see 12). In previous investigations, the modelled CO abundances are systematically higher than the observationally derived abundance, in particular for high C/O ratios (Duari et al., 1999),(Cherchneff, 2006). On the other hand, observational CO abundances are often presumed in order to account for mas-loss rates and wind

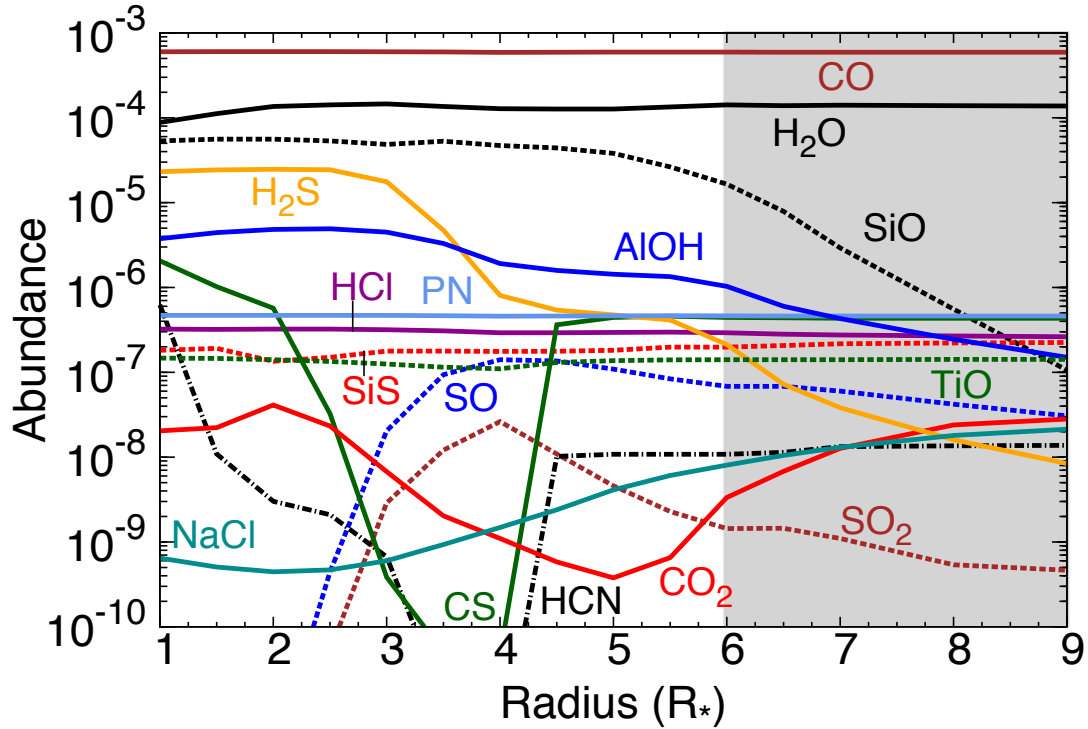


Figure 22: Abundances of the prevalent molecules versus radius

dynamics, and to derive abundances of other species than CO. H<sub>2</sub>O agrees well (within a factor of 2) with the most recent observations. Water is an important oxidation agent for silicate and alumina cluster formation. Despite the participation of water in cluster formation, its modelled abundance does not vary greatly with respect to R - see Figure 22. H<sub>2</sub>O is thus considered as a parent species. Furthermore, the model results for H<sub>2</sub>O are in good agreement with the models of Duari et al. (1999), Cherchneff (2006).

SiO shows a strong decrease in abundance with respect to R, which is related to silicate cluster and dust formation. In comparison to observations, the SiO model abundance fits best in the region, where the silicates are still forming (6-7 R<sub>\*</sub>). This is not the case in the models of Duari et al. (1999) and Cherchneff (2006), where the SiO abundance stays on values of the order 10<sup>-5</sup> with respect to R. However, these models did not consider cluster and dust formation. The model and observed abundances of the sulphur bearing species (SO, SO<sub>2</sub>, CS, SiS, H<sub>2</sub>S and SH) are discussed in detail in Section 5.3.

Moreover, Table tab6 lists also molecules, which have been detected in other oxygen-rich AGB stars. Beneath these species are the titanium oxides TiO and TiO<sub>2</sub>. These molecules have been detected around VY Canis Majoris and have a lower abundance than our model predicts. In this study, the reactions, that describe TiO and TiO<sub>2</sub> formation and destruction processes, are adopted from Plane (2013) and involves



whereas the forward reaction is exothermic, but is suppressed at high temperatures, owing to a negative Arrhenius parameter  $\beta$ , and the reverse reaction has an activation barrier of

Table 12: Predicted abundances (with respect to H<sub>2</sub>) of selected species. TE abundances are given at r<sub>s</sub> and modelled abundances are listed for r<sub>s</sub> and 6 R<sub>\*</sub>. Most recent abundances (with respect to H<sub>2</sub>) derived from observations are listed when available, with the corresponding reference.

Species	TE at r <sub>s</sub>	Modelled at r <sub>s</sub>	Modelled at 6 R <sub>*</sub>	Observed	Reference
CO	1.0 × 10 <sup>-3</sup>	7.3 × 10 <sup>-4</sup>	7.4 × 10 <sup>-4</sup>	1.0 × 10 <sup>-4</sup>	Decin et al. (2010b)
				1.5 × 10 <sup>-4</sup>	Kim et al. (2010)
H <sub>2</sub> O	2.1 × 10 <sup>-4</sup>	1.1 × 10 <sup>-4</sup>	1.8 × 10 <sup>-4</sup>	6.6 × 10 <sup>-5</sup>	Decin et al. (2010b)
SiO	9.5 × 10 <sup>-5</sup>	6.4 × 10 <sup>-5</sup>	1.9 × 10 <sup>-5</sup>	8.0 × 10 <sup>-6</sup>	Decin et al. (2010b)
				5.1 × 10 <sup>-6</sup>	
				- 1.3 × 10 <sup>-5</sup>	Kim et al. (2010)
SiS	4.0 × 10 <sup>-8</sup>	2.2 × 10 <sup>-7</sup>	2.7 × 10 <sup>-7</sup>	1.1 × 10 <sup>-5</sup>	Decin et al. (2010a)
				3.1 × 10 <sup>-7</sup>	
				- 1.3 × 10 <sup>-6</sup>	Kim et al. (2010)
SO	4.4 × 10 <sup>-8</sup>	2.1 × 10 <sup>-12</sup>	7.30 × 10 <sup>-8</sup>	1.0 × 10 <sup>-7</sup>	Schöier et al. (2007)
				2.7 × 10 <sup>-7</sup>	
				- 7.8 × 10 <sup>-7</sup>	Kim et al. (2010)
SO <sub>2</sub>	1.4 × 10 <sup>-11</sup>	1.8 × 10 <sup>-14</sup>	4.3 × 10 <sup>-9</sup>	4.0 × 10 <sup>-7</sup>	Decin et al. (2010b)
				2.0 × 10 <sup>-6</sup>	
				4.2 × 10 <sup>-6</sup>	
				- 1.4 × 10 <sup>-5</sup>	Kim et al. (2010)
				1.7 × 10 <sup>-8</sup>	
HCN	6.4 × 10 <sup>-12</sup>	7.7 × 10 <sup>-7</sup>	5.0 × 10 <sup>-8</sup>	- 3.7 × 10 <sup>-7</sup> <sup>2</sup>	Yamamura et al. (1999)
				1.3 × 10 <sup>-7</sup>	Schöier et al. (2013)
				4.4 × 10 <sup>-7</sup>	Decin et al. (2010b)
				4.3 × 10 <sup>-7</sup>	
				- 1.4 × 10 <sup>-6</sup>	Kim et al. (2010)
CS	2.0 × 10 <sup>-11</sup>	2.5 × 10 <sup>-6</sup>	5.6 × 10 <sup>-7</sup>	8.0 × 10 <sup>-8</sup>	Decin et al. (2010a)
				8.1 × 10 <sup>-8</sup>	
				- 3.0 × 10 <sup>-7</sup>	Kim et al. (2010)
PN	4.0 × 10 <sup>-10</sup>	5.7 × 10 <sup>-7</sup>	5.8 × 10 <sup>-7</sup>	3.0 × 10 <sup>-7</sup>	De Beck et al. (2013)
PO	1.0 × 10 <sup>-7</sup>	3.3 × 10 <sup>-10</sup>	2.0 × 10 <sup>-10</sup>	5.0 × 10 <sup>-8</sup>	
				- 6.0 × 10 <sup>-7</sup>	De Beck et al. (2013)
NaCl	3.7 × 10 <sup>-12</sup>	7.8 × 10 <sup>-10</sup>	1.0 × 10 <sup>-8</sup>	4.0 × 10 <sup>-9</sup>	Milam et al. (2007)
NH <sub>3</sub>	1.1 × 10 <sup>-11</sup>	2.8 × 10 <sup>-9</sup>	1.5 × 10 <sup>-19</sup>	(1 – 3) × 10 <sup>-6</sup>	Menten et al. (2010)
CO <sub>2</sub>	4.1 × 10 <sup>-8</sup>	2.5 × 10 <sup>-8</sup>	4.4 × 10 <sup>-9</sup>	5.9 × 10 <sup>-8</sup> <sup>3</sup>	Markwick & Millar (2000)
				- 4 × 10 <sup>-8</sup> <sup>4</sup>	Yamamura et al. (1999)
AlO	8.0 × 10 <sup>-9</sup>	2.6 × 10 <sup>-8</sup>	1.6 × 10 <sup>-10</sup>	3.4 × 10 <sup>-8</sup> <sup>5</sup>	Kamiński et al. (2013)
AlOH	4.5 × 10 <sup>-9</sup>	4.5 × 10 <sup>-6</sup>	1.5 × 10 <sup>-6</sup>	1.0 × 10 <sup>-7</sup> <sup>6</sup>	Tenenbaum & Ziurys (2010)
TiO	2.4 × 10 <sup>-7</sup>	1.8 × 10 <sup>-7</sup>	1.8 × 10 <sup>-7</sup>	5.0 × 10 <sup>-9</sup> <sup>7</sup>	Kamiński et al. (2013)
TiO <sub>2</sub>	1.3 × 10 <sup>-12</sup>	6.2 × 10 <sup>-10</sup>	4.8 × 10 <sup>-9</sup>	6.3 × 10 <sup>-10</sup> <sup>8</sup>	Kamiński et al. (2013)
HCl	3.5 × 10 <sup>-7</sup>	3.9 × 10 <sup>-7</sup>	3.7 × 10 <sup>-7</sup>	1.0 × 10 <sup>-8</sup> <sup>9</sup>	Yamamura et al. (2000)
AlCl	1.6 × 10 <sup>-10</sup>	3.8 × 10 <sup>-12</sup>	2.2 × 10 <sup>-10</sup>	< 5 × 10 <sup>-8</sup> <sup>10</sup>	Tenenbaum & Ziurys (2010)
SH	2.8 × 10 <sup>-6</sup>	1.3 × 10 <sup>-7</sup>	2.3 × 10 <sup>-8</sup>	2.0 × 10 <sup>-7</sup> <sup>11</sup>	Yamamura et al. (2000)
H <sub>2</sub> S	8.1 × 10 <sup>-8</sup>	2.8 × 10 <sup>-5</sup>	1.0 × 10 <sup>-8</sup>	< 2.0 × 10 <sup>-6</sup> <sup>12</sup>	Yamamura et al. (2000)

$E_a/R = 15570$  K. In the chemical network of Plane (2013), nucleation routes towards metal titanates and silicates have been explored. The author found that sufficient large clusters ( $> 20$  Å in radius) form and may act as condensation nuclei. In the present model, test runs with the complete chemistry, involving all reactions for metal titanates and silicates, were performed. However, we could not confirm the formation of such clusters. Moreover, a comparison to the models of Duari et al. (1999) and Cherchneff (2006) is not feasible, as these models do not include titanium species.

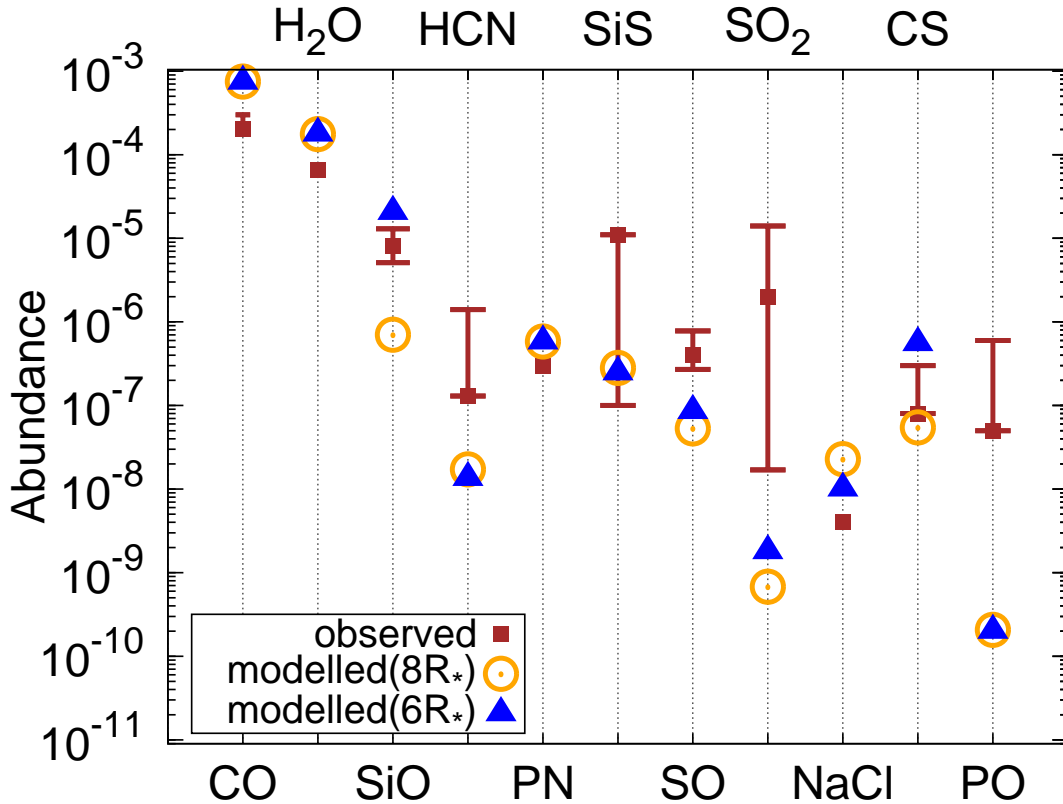


Figure 23: Comparison of modelled abundances (with respect to H<sub>2</sub> at 6 R<sub>\*</sub> and 8 R<sub>\*</sub>) with the most recent observations.

Furthermore, the aluminum-bearing species AlO, AlOH and AlCl have been observed around the red supergiant VY Canis Majoris, as can be seen in Table 12. AlOH and AlO participate directly in cluster and dust formation, The large abundance of AlOH in the inner wind may induce the formation of molecular species not considered in the present study, such as dimers of HAlOH. Again, a comparison to the models of Duari et al. (1999) and Cherchneff (2006) is lacking, as these models do not account for Al-bearing species.

HCl was observed in the S type AGB star R Andromeda and the given abundance is by an order of magnitude lower than in the present model. However, HCl has not been detected in IK Tau and the model predicts, that HCl is the most abundant chlorine-bearing molecule, followed by NaCl and atomic Cl. The species ClO, Cl<sub>2</sub>, and CaCl are at least 3 order of magnitude less abundant and play thus a minor role in the inner winds of Mira variables. As member of the chlorine family HCl is linked to salt (NaCl) by several reactions involving

the species NaH. Moreover, HCl is part of the large and dominant hydrogen chemistry.

### 5.3 Sulphur Chemistry

Sulphur is relatively abundant and has the ability to form a variety of molecules, many of which are volatile (Omont et al., 1993). Due to its electronic structure, which is similar to oxygen, molecules like CS, H<sub>2</sub>S, SiS - as counterparts to CO, H<sub>2</sub>O and SiO - are expected in oxygen-rich AGB atmospheres. Omont et al. (1993) investigated sulphur-bearing molecules in 14 distinct OH/IR sources and found H<sub>2</sub>S and SO<sub>2</sub> emission lines in most of the envelopes. These observations were performed at millimetre wavelength and relate to the intermediate and outer envelope of AGB stars. In TE H<sub>2</sub>S is the dominant sulphur-bearing species at temperatures below 1800 K (Tsuji, 1973). However, equilibrium conditions are not satisfied at all in the AGB atmospheres as previously pointed out. In the post-AGB stars and in the PN phase, the observed sulphur abundances are unexplained low, indicating a depletion mechanism during the AGB phase (Shingles & Karakas, 2013). Sulphur may deplete on the surface of grains. In the chemical network, the sulphur-bearing species H<sub>2</sub>S, SH, SO, SO<sub>2</sub>, SiS, and CS are considered. Except SO<sub>2</sub>, the observational abundances of the listed species are reproduced by our model within a reasonable level of confidence. The sulphur chemistry is thus related to the hydrogen, oxygen, carbon, and silicon chemistry, respectively. These chemistries are crucial for the understanding of the inner envelope chemistry as they describe the most abundant molecules H<sub>2</sub>, CO, H<sub>2</sub>O and SiO. Moreover, the sulphur chemistry may indirectly affect dust formation through SiS. These facts all demonstrate the complexity of the sulphur-related chemistry. In the forthcoming subsection the sulphur chemistry and its constituents are described.

#### Sulphur dioxide

Scalo & Slavsky (1980) were the first who discussed sulphur species in the chemistry of oxygen-rich circumstellar envelopes and proposed at the following formation reaction:



This reaction is barrierless and also the dominant formation channel in the chemical network used in this thesis. Other SO<sub>2</sub> formation reactions involve the radiative association of SO+O, the termolecular rate of SO+O+M and the formation via OCS+OH. However, the rather low reaction rates and the low O, O<sub>2</sub>, and OCS abundances lead to minor contributions in the SO<sub>2</sub> formation. The modelled SO<sub>2</sub> abundance at 6 R<sub>\*</sub> is  $x(\text{SO}_2) = 1.8 \times 10^{-9}$ , which indicates that the molecule does not efficiently form by reaction 48. Velilla Prieto et al. (2013) performed an abundance analysis around IK Tau and obtained an fractional SO<sub>2</sub> abundance of  $3.5 \times 10^{-7}$  which is a factor of  $\sim 3$  lower than  $1 \times 10^{-6}$ , the value derived by Decin et al. (2010a). However, the high abundance of  $x(\text{SO}_2) = 1 \times 10^{-6}$  relates to emission lines originating in the region 50 -200 R<sub>\*</sub>. This is outside the inner envelope,

and thus

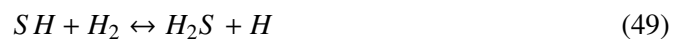
In the rotational level population diagram (i.e. Boltzmann diagram) of Velilla Prieto et al. (2013), two different rotational temperatures can be found, indicating two distinct temperature components. Therefore, not all rotational level populations are in TE and abundances. From Ir observations, Yamamura et al. (1999) derived fractional abundances of  $1.7 \times 10^{-8}$  -  $3.7 \times 10^{-7}$  in the oxygen-rich AGB T Cep within  $6 R_*$ . This is in agreement with the modelled SO<sub>2</sub> abundance at  $4 R_*$ ,  $x(\text{SO}_2) = 3.3 \times 10^{-8}$ .

Fu et al. (2012) observed SO<sub>2</sub> in the red supergiant VY Canis Majoris and found rotational lines with fast velocities of 28 to 42 km s<sup>-1</sup> in three distinct loci in the envelope indicating a distance far from the star. In addition, they found that OH maser and SO emission are spatially strongly correlated with SO<sub>2</sub> lines. Reaction 48 is thus a potential formation process of SO<sub>2</sub>. The observations indicate a transition radius, where  $x(\text{SO}) = x(\text{SO}_2)$ . However, it should be noted that VY CMa is a (o-rich) red supergiant with a highly complex wind (O’Gorman et al., 2015).

## Hydrogen Sulphide

The mercapto radical, SH, is the first molecule formed from S atoms in oxygen-rich giants and TE around 2000 K (Yamamura et al., 2000). The authors find SH in a thin shell located at  $1.0 - 1.1 R_*$  and estimate its abundance relative to H<sub>2</sub> as  $x(\text{SH}) = 10^{-7}$  in the S-type star R Andromeda. In oxygen-rich star atmospheres, SH should be quite abundant according to TE calculations. In addition, it is not expected that SH has a much different abundance in S-type stars and in O-rich stars, as neither S nor H is enhanced or reduced in S-type stars compared to M-type stars.

Omont et al. (1993) detected transition lines of H<sub>2</sub>S at 168.8 GHz and 216.7 GHz in red giant stars including IK Tau. Assuming TE and  $T < 1800$  K H<sub>2</sub>S is the dominant sulphur bearing molecule. The authors were concerned with the question whether H<sub>2</sub>S was the *parent* species of the oxides SO and SO<sub>2</sub> present in the intermediate envelope or whether it was atomic S. The authors could not provide a clear answer and concluded that the H<sub>2</sub>S abundance is extremely dependent on the available atomic hydrogen and its synthesis occurs on grains. Moreover, the rotational temperatures and narrow emission lines of H<sub>2</sub>S indicate a location in the inner layers of the envelope, where the wind not yet has been fully accelerated. Analogue to water and the hydroxyl radical, SH and H<sub>2</sub>S are strongly coupled by the reaction



These observations agree well with the model for IK Tau, as can be seen from Figure 22. SH and H<sub>2</sub>S dominate the sulphur chemistry at gas layers close the star. Around  $3 - 4 R_*$  the sulphur-bearing CS and the oxides SO and SO<sub>2</sub> are formed at the cost of H<sub>2</sub>S and SH.

## Carbon Sulphide

Carbon sulphide, CS, is one of the unexpected carbon-bearing molecule surrounding IK Tau. Particularly close to the photosphere and after  $4 R_*$ , the model is predicting its presence as can be seen in Figure 22.

The modelled abundance of CS relative to  $H_2$  is  $x(\text{CS}) = 5.6 \times 10^{-7}$ , which is a bit higher than the recently measured value of  $x(\text{CS}) = 8 \times 10^{-8}$  (Decin et al., 2010b), but still in good agreement. The present model agrees with the models of Duari et al. (1999) and Cherchneff (2006), which find similar high CS abundances of the range  $10^{-6} - 10^{-5}$  in the region close to the star ( $1-2 R_*$ ), albeit the TE abundance of CS is very low ( $\sim 10^{-11}$ ), as can be seen in Table 12. The presence of CS close to the star is thus a result of shock-induced chemistry. At larger radii ( $R > 2 R_*$ ), the CS abundances decrease in all models. However, in Cherchneff (2006) the decrease in CS is much less pronounced than in the present model. In Duari et al. (1999), no abundances for  $R > 2.2 R_*$  are available. The difference at larger radii can be attributed to the different scale heights used in the models. For example, the preshock density at  $3 R_*$  in Cherchneff (2006) is a factor of  $\sim 50$  higher than in the present model.

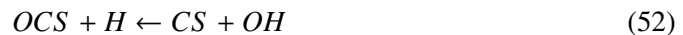
In between there is a gap which will be explained in the following. The photospheric TE abundance of CS is very low ( $f(\text{CS}) = 9.4 \times 10^{-12}$ ). In the first parcel excursion at  $1 R_*$ , the CS abundance increases drastically due to the reaction



SH is abundant close to star (see previous paragraph) and atomic C is available owing to collisional dissociation of CO (and other carbonaceous molecules) in the preceding shock. Another reaction which acts predominantly at later phase ( $\Phi > 0.1$ ) and explains the striking correlation between the abundances of HCN and CS sets in:



The rates are high and almost barrierless in both directions and thus act throughout the inner envelope. thus coupling CS and CN closely. CN, in turn, is closely linked to its hydrogenated form, HCN, by the reaction  $H_2 + CN \leftrightarrow HCN + H$ . At later phase ( $\Phi > 0.3$ ) the dominant formation channel for CS is:



Here, the carbonyl oxide (OCS) comes into play. OCS or COS has been detected around IK Tau, although the results are preliminary and still need to be confirmed (Sanchez Contreras et al., 2011). To explain observed CS abundance it is thus essential to have OCS included in the chemical network. OCS itself is formed by the free S and the abundant CO molecule. The reaction channel  $S + CO \rightarrow CS + O$  is very improbable as it involves the breaking of the strong CO bond and a subsequent atomic rearrangement. Reaction 52 remains the main contributor to CS formation in the subsequent excursions at larger radii ( $R >$

1  $R_*$ ). However, having a barrier of  $E_a/R \sim 13'000$  K the contribution to the CS formation becomes weaker as further the distance from the star. Moreover, reaction 52 cannot not overcome the reaction



which has a high ( $A = 2.5 \cdot 10^{-10} \text{ cm}^3 \text{ s}^{-1}$ ) and almost barrierless ( $E_a/R \sim 780$  K) rate. It is responsible for the decrease in CS around 2-4  $R_*$ . At these radii the freed S is converted partially in sulphur oxides SO and SO<sub>2</sub>. In addition, there are also major contribution from SH and H<sub>2</sub>S. Responsible for the sudden increase of the CS abundance after 4  $R_*$  are reactions 52 and 53, and the increase of HCN which is strongly linked to CS (see above).

### Silicon Sulphide SiS

The SiS abundance depends on the photospheric C/O ratio which is confirmed observationally (Schöier et al., 2007) as well as from the theoretical point of view (Cherchneff, 2006). At first glance, this is unexpected as this radicalic molecule does neither contains carbon nor oxygen atoms. On the other hand SiS is linked to the sulphur and the silicon chemistry, and the latter is crucial for the formation of SiO and silicates dust grains. SiO and silicates play no (or a minor) role in carbon-rich environments and thus more silicon to form SiS is available in this case.

The chemistry of SiS is poorly characterised. Its termolecular formation (Si+S+M) and the reverse collisional dissociation (SiS+M) predominantly act close to the star owing to high densities and temperatures. Moreover the reaction Si + CS which efficiently forms SiS and its reverse are part of the network. This reaction has a fairly high activation temperature ( $E_a/R = 35'000$  K) and thus also acts close to the photosphere where still high temperatures prevail.

The modelled SiS abundance stays on a approximately constant level of  $\sim 2 \times 10^{-7}$ , which agrees with the most recent observations (see Figure 22 and 23). These results reflect on one hand the not well characterised SiS chemistry and on the other hand the independence of the SiS abundance on the wind density (Schöier et al., 2007). In Cherchneff (2006), the SiS abundance has an abundance of  $1.7 \times 10^{-6}$  at 1  $R_*$  and decreases to values below  $10^{-8}$  at 4  $R_*$ . In Duari et al. (1999), the decrease of the SiS abundance is more drastic and result in  $x(\text{SiS}) = 3.8 \times 10^{-10}$ . The decrease in the SiS abundance can be attributed to the reaction



which is not part of the present network, as S<sub>2</sub> is not considered.



## Molecular line observation

In the framework of this thesis observations of SiS at OSO (Onsala Space Observatory) and IRAM (Institut de Radioastronomie Millimetrique) have been carried out. The observations of SiS ( $J=12 \rightarrow 11$ ) were performed in 12 distinct galactic S-type sources. Some of them showed a tentative signal. Unfortunately, up to date the observational results have not been fully analysed. As part of the present thesis, some basic concepts of molecular observations will be briefly discussed in the this subsection.

In order to observe circumstellar molecular lines, the ground-based telescope is brought into a position, where the telescope is oriented to a strong emission source (e.g. Uranus). As the Earth is rotating, the angle to the source is shifting, and the telescope orientates accordingly, in order to still point to the same source. The pointing source should fulfil the condition of a high enough altitude (i.e. the telescope antenna cannot point in the ground). This orientation procedure is referred to as pointing. In addition, the pointed source has to be focussed. Focussing is concerned with the optical depth between observer and source and needs to be adjusted, if weather changes or day / night tendencies.

Pointing and focussing are the essential to ground-based astronomical observations, and are prerequisites for the quality. Once pointing and focussing are done satisfactorily, the observing run can start. As the observational raw data exhibit rather scattered and erratic behaviour, weak signals/lines may be blended/hided (e.g. by strongly oscillating, high amplitude distortions). Such variations can be eliminated by subtracting spectra from each other. The final spectrum is a difference of several spectra containing the desired signal and reference spectra. This is realized by switching between two phases (provided, that the switching is faster than atmospheric fluctuations or receiver instabilities):

- beam switching: fast beam switching in the same frequency band results in very good baselines.
- position switching: slow switching ( $\sim 1 \text{ min}^{-1}$ ) used for regions with large source extents.
- frequency switching: best observing mode with respect to the signal-to-noise ratio, provided that signal and reference frequencies fall within the same band of the spectrometer.

For the final spectra, the beam switching method was predominantly used, owing to its speed and the atmospheric changes during the observing run.

The AGB sources must have a high enough galactic altitude during observation, as the significance of the lines strongly depends on the distance of light traveled through the atmosphere. This is implicitly expressed in the system temperature  $T_{sys}$ :

$$T_{sys} = \left[ T_{rec} + T_{gpu} + T_{tm} \left( 1 - \exp\left(-\frac{\tau_0}{\sin(\theta)}\right) \right) \right] \exp\left(\frac{\tau_0}{\sin(\theta)}\right) \quad (55)$$

where  $T_{sys}$  is the temperature of the system,  $T_{rec}$  the receiver temperature,  $T_{gpu}$  the ground pick-up temperature (some 20 K),  $T_{tm}$  the effective atmospheric temperature,  $\tau_0$

the atmospheric zenith opacity, and  $\theta$  the elevation angle, respectively. All these quantities are given by the environment of the telescope, except the elevation angle  $\theta$ , which depends on the time-dependent location of the source. The lower the system temperature,  $T_{sys}$ , the higher is the signal-to-noise ratio of the observations, and the better is the quality of the observed spectra.  $T_{sys}$  is minimal, if the elevation  $\theta$  corresponds to 90 degrees, and  $T_{sys}$  is maximal, if  $\theta$  corresponds to 0 degrees.

Unfortunately, the observational data has not yet been fully reduced and analysed. Thus, the resulting spectra cannot be presented in this thesis.

## 5.4 Nitrogen and Phosphorus Chemistry

In the previous subsection the close relation of HCN, CN and CS was clarified and discussed. Beside the cyanide molecules CN and HCN nitrogen oxides (NO, NO<sub>2</sub>) and hydrides (NH, NH<sub>2</sub>, NH<sub>3</sub>), and molecular nitrogen (N<sub>2</sub>) are part of the chemical network. Most of the nitrogen around AGB stars (this is also valid for carbon-rich giants) is in the form of molecular nitrogen N<sub>2</sub> due to its high dissociation energy (9.8 eV  $\approx$  114'000 K) and its triple bond. The high binding energy of N<sub>2</sub> lead to a similar situation as for CO and hampers the release of free atoms at low temperatures. Furthermore, N<sub>2</sub> has no dipole character as its constituent atoms are identical (see e.g. Habing & Olofsson 2003) thus it is difficult to measure accurate N<sub>2</sub> abundance and depletion patterns. N<sub>2</sub> has an equilibrium abundance of 1.e-4. Owing to the high stability of molecular nitrogen reactions depleting N<sub>2</sub> have high activation barriers of 30'000 -100'000 K. Most of the reverse reactions are barrier-less and thus N<sub>2</sub> is not destroyed.

Ammonia (NH<sub>3</sub>) has been the first polyatomic molecule detected in the interstellar medium (Cheung et al., 1968). Due to possible orientations of the nuclear hydrogen spins, two different species of NH<sub>3</sub> exist that do not transform into each other, ortho-NH<sub>3</sub> and para-NH<sub>3</sub>. The ortho-to-para ratio is assumed to be 1, appropriate for NH<sub>3</sub> formation under high temperatures (Menten et al., 2010). Menten et al. (2010) investigated several oxygen-rich AGB stars with Herschel and looked for their ammonia content. For IK Tau, the authors deduced an NH<sub>3</sub> abundance, relative to H<sub>2</sub>, of  $(1 - 3) \times 10^{-6}$  within a shell of 200 R<sub>\*</sub>. In the present model, very small amounts of NH<sub>3</sub> from the gas phase in the inner wind, as seen from Table 12.

However, these data indicate a formation region with gas number densities of  $\sim 10^6 \text{ cm}^{-3}$  and gas temperatures in the range 10 - 100 K, typical of the intermediate envelope. Therefore, NH<sub>3</sub> molecules that cannot form in the shocked inner wind from the gas phase. Thus, NH<sub>3</sub> could well be synthesised on the surface of dust grains in the intermediate envelope.

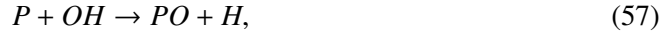
Recent observations by De Beck et al. (2013) give relatively high amounts PN and PO around IK Tau (within 40 R<sub>\*</sub>):  $x(\text{PN}) = 3 \times 10^{-7}$  and  $x(\text{PO}) = (0.5-6) \times 10^{-7}$ . The authors report no detection of HCP, PH<sub>3</sub>, CP and PS, which have been previously observed in the carbon-rich AGB IRC+10216 (see e.g. Agúndez et al. 2008 and references therein).

From equilibrium calculation at the photosphere, atomic P, PS and PO should be the major carrier of phosphor. PH, PH<sub>3</sub>, PN and P<sub>2</sub> play a minor role in equilibrium chemistry. Note that the thermo-chemical data for PN, PH and PH<sub>3</sub> has been recently revised (Lodders, 1999). The phosphorous chemistry is very poorly characterised and rates are estimated. In order to derive reaction rates for the phosphorous chemistry, often the isovalence P/N, both having five valence electrons, is used, although its validity has been questioned (Cherchneff, 2012). PS has not been observed in circumstellar environments so far. The revised thermochemical data for PH<sub>3</sub>, PH and PN from Lodders (1999) is included in our equilibrium calculation, but does hardly affect the yields of these species, as non-equilibrium processes dominate the phosphorus chemistry. An illustrative example is PN. Its photospheric equilibrium abundance at in IK Tau is  $x(\text{PN})_{TE} = 2.0 \times 10^{-10}$ , but already in the first parcel, PN adopts a value of  $x(\text{PN})_{1R_*} = 4 \times 10^{-7}$  and stays on this abundance within the used computational domain (1 - 10R<sub>\*</sub>). This is also consistent with observations by De Beck et al. (2013).

For PO, the present model underestimates the observed abundance by three orders of magnitude. The dominant formation process for PN is the reaction is



while PO essentially forms from the reaction



and



The rates of reactions have been estimated from the N/P isovalence and have not been measured or theoretically assessed. However, the formation of PO is linked to that of PN. Then, the slight over-estimate of the depletion of P atoms in PN as shown by our modelled value may result in lowering the PO abundance. We thus attribute the discrepancy between modelled and observed PO abundances to a poorly characterised chemistry but notice that the isovalence principal gives a satisfactory match for PN.

## 5.5 Clusters and Dust Grains

The formation of clusters has been extensively discussed in Section 4.6 and we present in the present section results on dust grain size distributions and masses. We first discuss results for alumina dust and later present results for silicates.

## 5.6 Alumina

Notably, in model for Mira variables, the condensation efficiency, (i.e. the percentage of dimers, which condenses) is high (more 99 % for both stars and both condensates, alumina

and forsterite). Therefore, dust grains form, if the corresponding clusters are available and abundant. Alumina dimers form close to the star at late phase as can be seen in Figure 24. The formation of dust grains is coupled to the gas-phase chemistry and estimated at each integration time step over pulsations. Results on grain size distributions for both alumina and silicate grains are presented, and the derived dust-to-gas mass ratio are listed in Table 13.

Table 13: Comparison of the dust-to-gas mass ratios for IK Tau, TX Cam, and IK Tau in the  $\times 10$  density case.

	IK Tau (1 $M_{\odot}$ )	TXCam (1 $M_{\odot}$ )	IK Tau (density $\times 10$ )
1 $R_*$	<i>Alumina</i>		
$\Phi = 0.6$	$2.1 \times 10^{-9}$	$2.8 \times 10^{-18}$	$8.8 \times 10^{-6}$
$\Phi = 0.8$	$4.1 \times 10^{-7}$	$6.5 \times 10^{-10}$	$6.0 \times 10^{-5}$
$\Phi = 1.0$	$3.3 \times 10^{-6}$	$8.1 \times 10^{-8}$	$6.9 \times 10^{-5}$
	<i>Forsterite</i>		
3.5 $R_*$	$1.3 \times 10^{-4}$	$6.4 \times 10^{-6}$	$4.7 \times 10^{-4}$
4 $R_*$	$4.6 \times 10^{-4}$	$1.6 \times 10^{-5}$	$1.1 \times 10^{-3}$
5 $R_*$	$7.3 \times 10^{-4}$	$2.5 \times 10^{-5}$	$3.0 \times 10^{-3}$
6 $R_*$	$1.0 \times 10^{-3}$	$4.1 \times 10^{-5}$	$5.1 \times 10^{-3}$
7 $R_*$	$1.4 \times 10^{-3}$	$5.8 \times 10^{-5}$	$6.1 \times 10^{-3}$
8 $R_*$	$1.7 \times 10^{-3}$	$7.8 \times 10^{-5}$	$6.7 \times 10^{-3}$

The clusters of alumina dust chiefly form in the post-shock gas at 1  $R_*$ , and their corresponding abundances are illustrated in Figure 24. The formation of  $\text{Al}_2\text{O}_3$  involves the dimerisation of AIO through trimolecular recombination, while AIO forms from the reaction of Al with OH in the first place. The dimerisation of  $\text{Al}_2\text{O}_3$  is also described by trimolecular recombination to form the  $\text{Al}_2\text{O}_3$  dimer,  $(\text{Al}_2\text{O}_3)_2$ , which has a binding energy of 15.7 eV  $\sim$  182 000 K (Li & Cheng, 2012), and can thus withstand the high temperatures of the post-shock gas. This dimer is considered as the seed cluster that will further condense into alumina grains.

Over one oscillation resulting from the first shock at 1  $R_*$ , only a small amount of alumina dimers form to reach an abundance of  $1 \times 10^{-10}$  at  $\Phi = 1$ . A large fraction of Al stays in the form of molecular rings (e.g.,  $\text{Al}_2\text{O}_2$  and  $\text{Al}_2\text{O}_3$ ). Because the dimerisation of AIO and  $\text{Al}_2\text{O}_3$  is trimolecular, cluster formation occurs over a reduced range of radii in the inner wind and the formation of  $\text{Al}_2\text{O}_3$  cluster ceases after 2  $R_*$ .

The grain size distributions for alumina are presented in Figure 25 as a function of radius and pulsation number. For the first pulsation  $\Phi = 1$  at 1  $R_*$ , the distribution peaks at grains in the size range 50 - 200 Å, despite the small fraction of  $\text{Al}_2\text{O}_3$  clusters available. However, the post-shock gas densities are very high at 1  $R_*$ , as seen from Table 1, and the clusters coagulate and condense with high efficiency and lead to the formation of  $\text{Al}_2\text{O}_3$  grains of medium size. At each shock passage, molecules in the shocked photosphere are destroyed and reformed, while alumina grains are not. For a gas drift velocity of 0.5 km  $\text{s}^{-1}$ , the gas layer at 1  $R_*$  takes 12 pulsations to reach 2  $R_*$ . We thus consider the build-

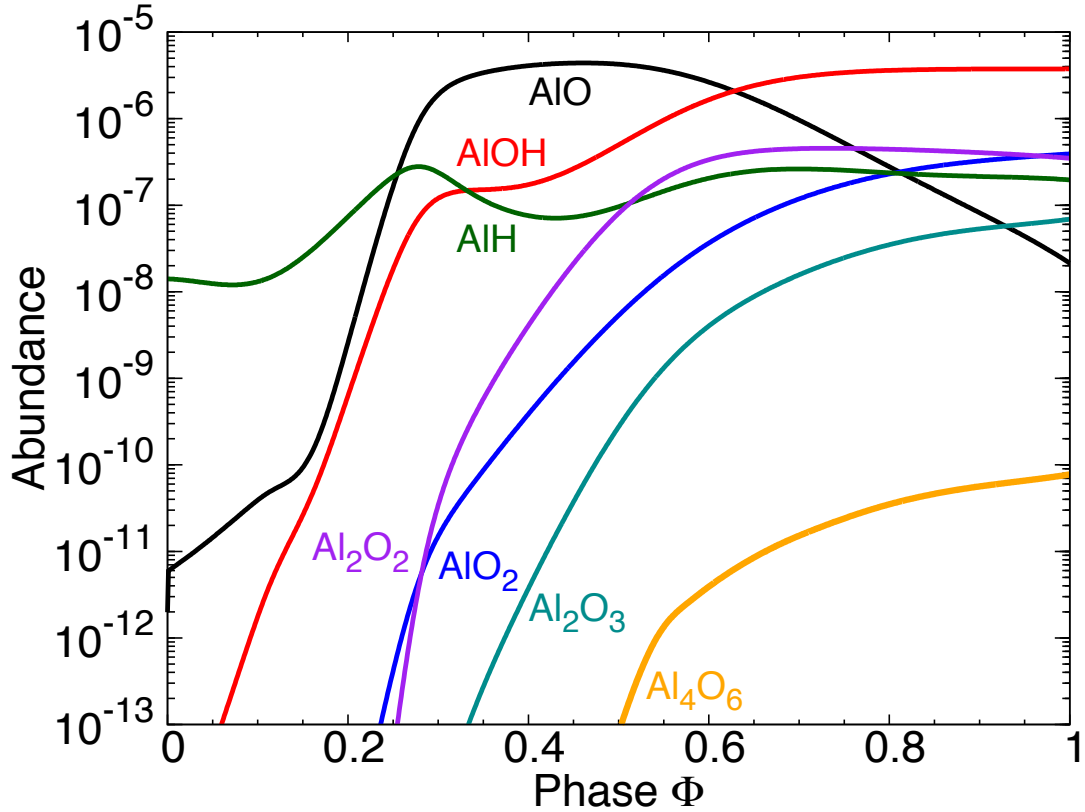


Figure 24: Alumina-related fractional cluster abundances as a function of pulsation phase in the first parcel excursion at  $1 R_*$ , where alumina starts forming.

up of dust grains over a number of 12 pulsations for the standard gas conditions. We see from Figure 25 that the grain size distributions are skewed towards large grain sizes. At  $2 R_*$ , the distribution comprises two dust grain components peaking at  $500 \text{ \AA}$  and  $0.5 \mu\text{m}$ , respectively. All small grains produced in the first oscillation at the shocked photosphere have effectively condensed in very large grains after 12 pulsations. The distribution does not change at  $r > 2 R_*$ , owing to a shortage of growing agents as all alumina clusters have been included in dust grains. The mass of alumina dust produced remains modest and the dust-to-gas mass ratio varies from  $3.3 \times 10^{-6}$  at  $1 R_*$  and  $\Phi = 1$  to  $3.3 \times 10^{-5}$  at  $2 R_*$ , as seen from Table 13.

## 5.7 Silicates

Small clusters of silicates form further out of the shocked, stellar photosphere, as seen in Figure 26, where abundances of key molecules involved in the nucleation of silicates and of small clusters are shown as a function of radius. The silaformyl radical,  $\text{HSiO}$ , and silanone,  $\text{H}_2\text{SiO}$ , start to efficiently form at  $r > 1.5 R_*$  because at shorter radii, the reverses of reactions in Table 10 are favoured and the destruction of these nucleating species ensues.

The synthesis of dimers of forsterite stoichiometry starts at radii greater than  $3 R_*$ , and the abundances of the prevalent clusters involved in the nucleation phase are shown in

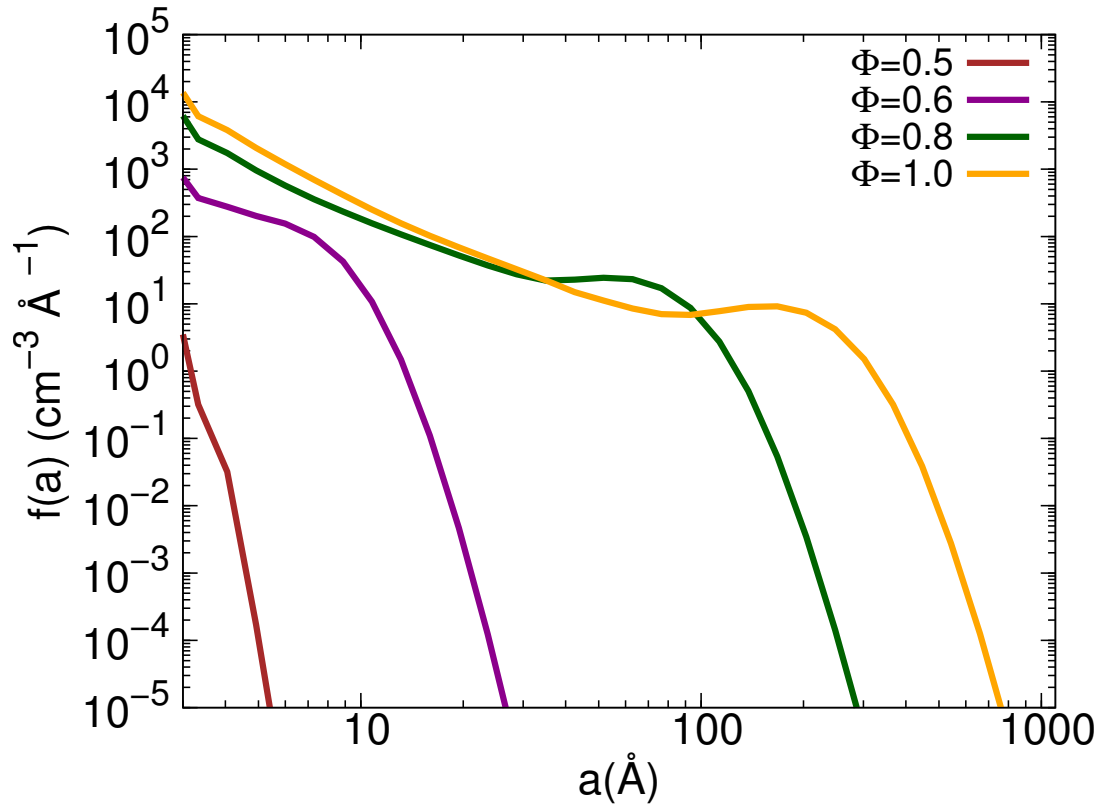


Figure 25: Alumina grain size distributions as function of the pulsation phase (time) at  $1 R_*$ .

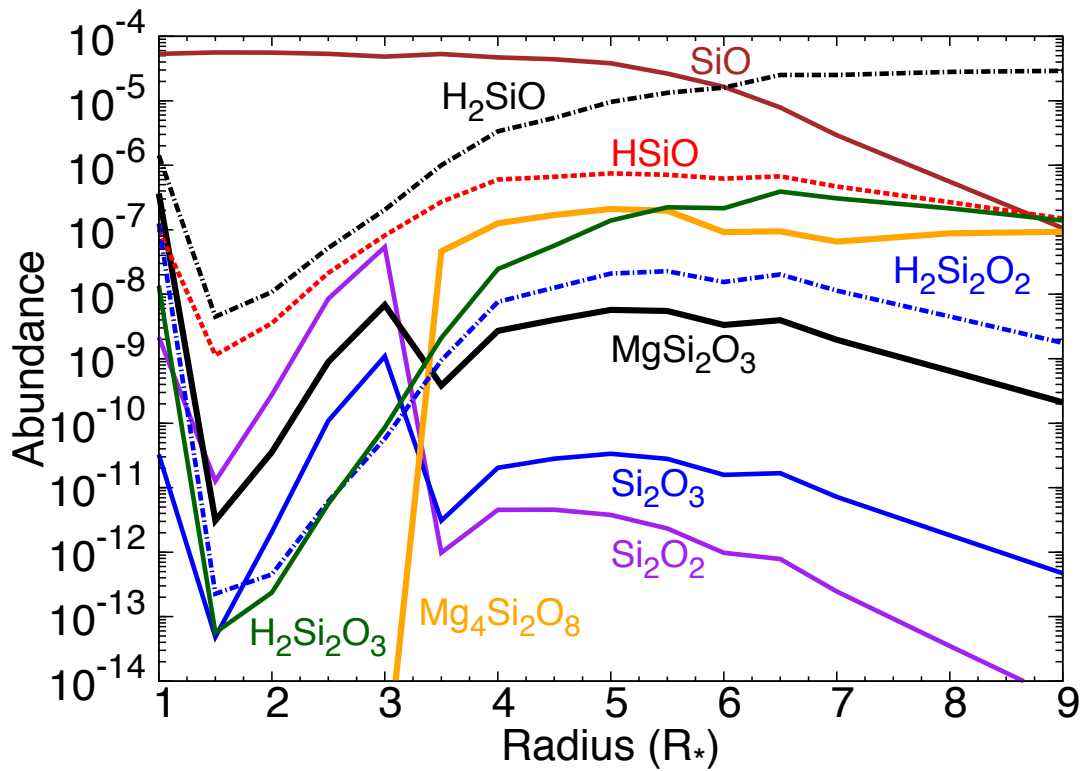


Figure 26: Silicate cluster abundances as a function of the radius. Silicate clusters start forming at  $3.5 R_*$ .

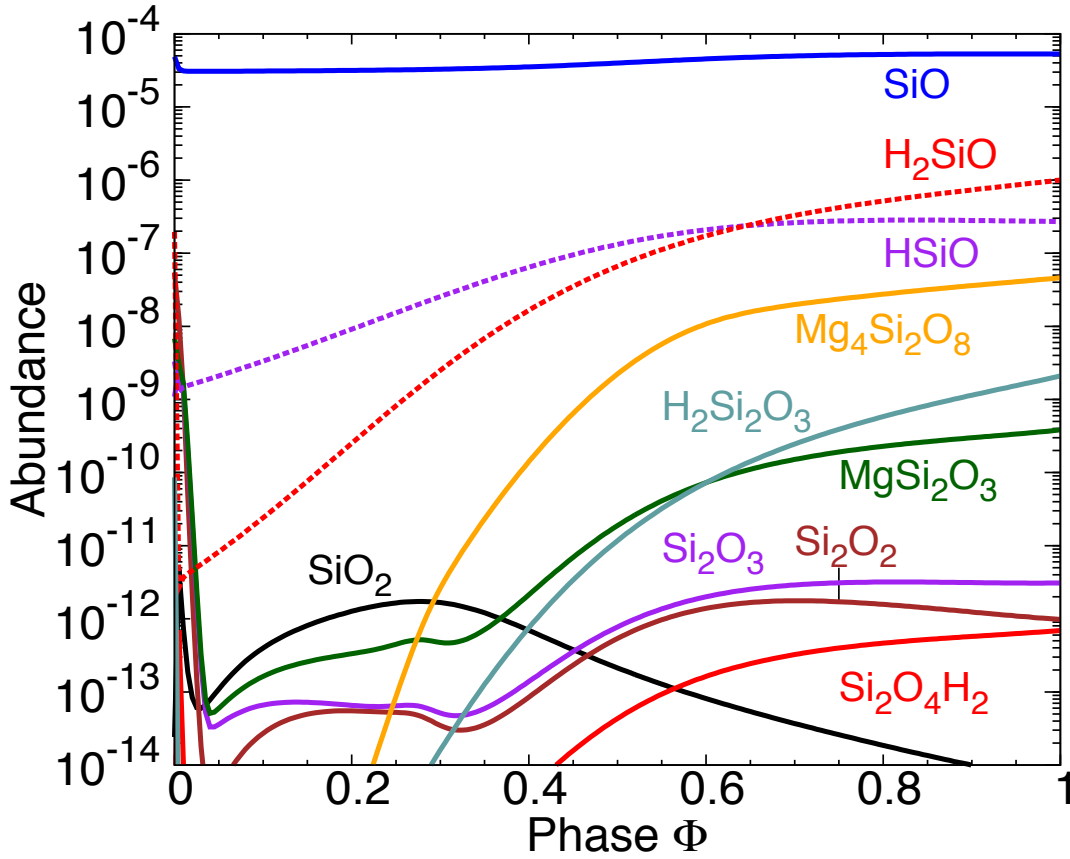


Figure 27: Silicate cluster abundances in the parcel excursion at  $3.5 R_*$  where forsterite starts forming

Figure 27 for the excursion at  $r = 3.5 R_*$ . The gas temperature at which all intermediate clusters are effectively converted in silicate dimers is  $\sim 1200$  K in the post-shock gas, whereas the gas number density is  $\sim 4.5 \times 10^{10} \text{ cm}^{-3}$ .

The build up of silicate dust takes place from  $3.5 R_*$  onwards, over several stellar pulsations. For the presumed gas drift velocity of  $1.5 \text{ km s}^{-1}$ , it takes 2 pulsations to travel a distance of  $0.5 R_*$ . Therefore, 10 pulsations are necessary to move from  $3.5 R_*$  to  $6 R_*$ , where the growth of silicate grains slows down and almost reach completeness at  $8 R_*$ . Figure 28 shows the silicate grain size distributions at various radii and pulsation numbers. We see that the size distribution has a tail of large grains that peaks around  $50 \text{ \AA}$  at  $3.5 R_*$ , and reaches  $\sim 200 \text{ \AA}$ , at  $r \geq 6 R_*$ . The dust-to- gas mass ratio listed in Table 13 reaches  $1.0 \times 10^{-3}$  at  $6 R_*$ , and the ratio keeps increasing for  $10 R_*$ , to reach  $\sim 2 \times 10^{-3}$ . These values agree with dust-to-gas mass ratios derived from observations of O-rich Mira stars. Based on the derived gas-to-dust mass ratios, we estimate that  $\sim 24\%$  of the elemental silicon abundance is depleted in silicate grains at  $6 R_*$ .

Because the growth of silicate grains takes place between  $3 R_*$  and  $6 R_*$  and slows down from  $6 R_*$  onward, the wind acceleration, which is triggered by radiation pressure on dust grains, should start developing as soon as enough dust grains form in the radius range  $3.5 - 4 R_*$ , and increase when the grain sizes are large enough to reach full regime, i.e., at  $r \geq 6 R_*$ . This acceleration will result in the freezing of molecular abundances after  $r >$

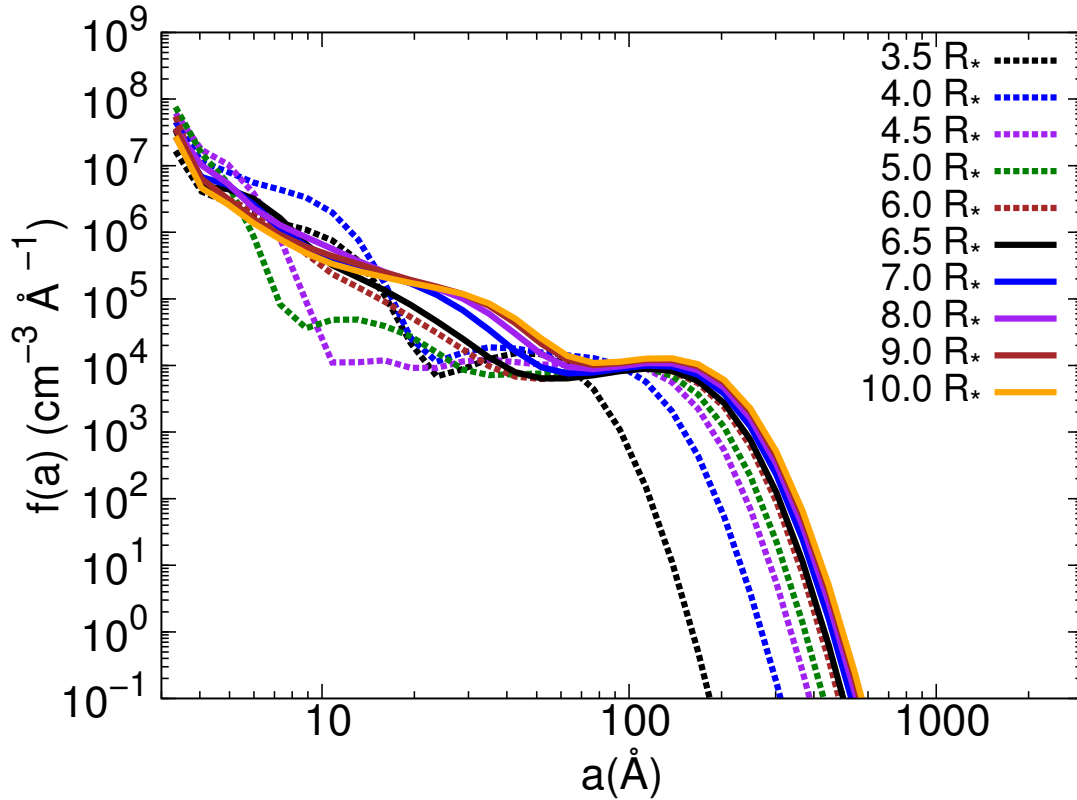


Figure 28: Forsterite grain size distributions as function of the radius / number of excursions in the pulsation model.

6  $R_*$ . This is the underlying reason for comparing modelled abundances at 6 - 8  $R_*$  with observations.

## 5.8 A High Gas Number Density Case

Despite the fact that the present standard model for IK Tau provides satisfactory dust-to-gas mass ratios for silicates compared to values derived from observations, the grains in which most of the silicate mass is concentrated have an average size on the low end (i.e.,  $\sim 200$  Å). We thus test the impact of the gas number density on the synthesis of clusters and dust grains, by giving a special attention to grain size. We increase the gas number density at the photosphere by a factor of ten and keep all photospheric parameters and shock description as before.

This increment in number density is certainly too high to properly describe the IK Tau. However, such a number density enhancement may characterise inhomogeneities in the inner wind. In Figures 29 and 30, the grain size distributions for alumina and silicates are shown at 6  $R_*$ . We see that a denser gas produces much larger grains. For alumina, most of the dust mass resides in large grains. The two peaks at  $\sim 180$  Å and  $\sim 0.4$   $\mu\text{m}$  in Figure 29 are now shifted to  $0.3$   $\mu\text{m}$  and  $4$   $\mu\text{m}$ , and the gas-to-dust mass ratio has increased by a factor of  $\sim 23$  compared to the standard case, as seen in Table 13. In both cases, the grains are large enough to possibly start triggering a wind via Mie scattering on large grains very



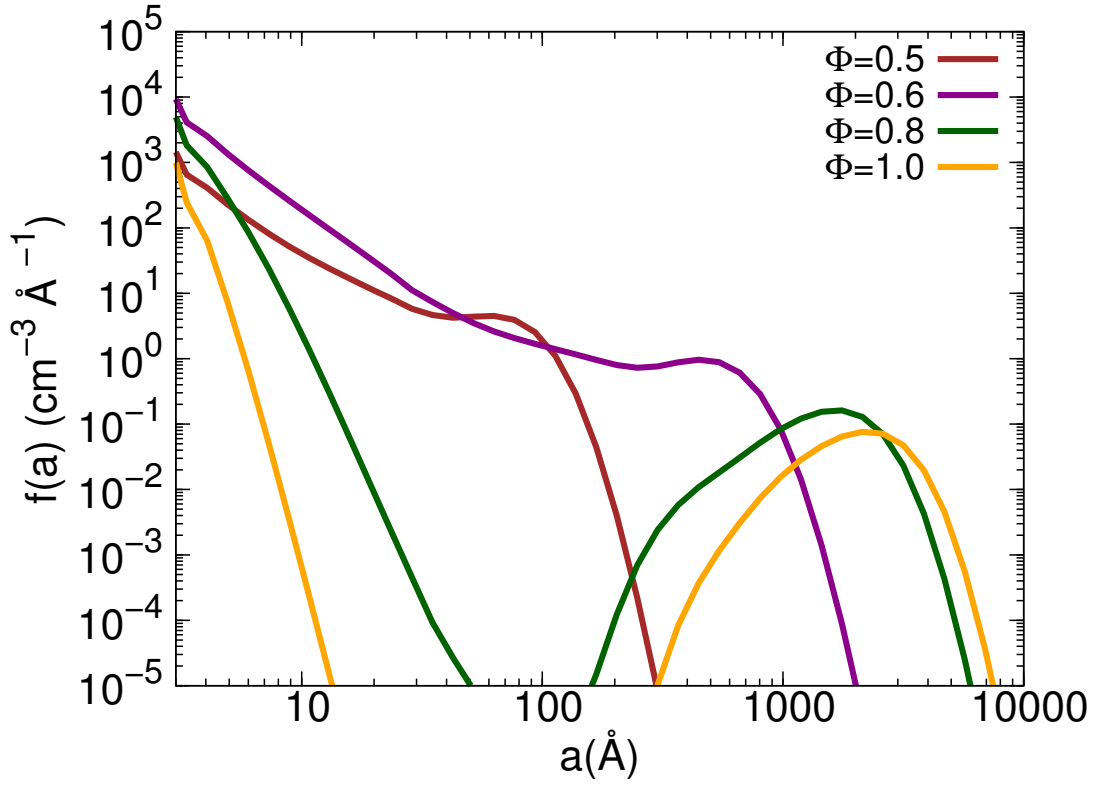


Figure 29: Alumina grain size distributions as function of the pulsation phase (time) at  $1 R_*$  in the  $\times 10$  density case.

close to the star (Höfner, 2008).

As for alumina, the silicate grains reach an average size of  $0.1 \mu\text{m}$  at  $6 R_*$ , with a dust-to-gas mass ratio of  $5 \times 10^{-3}$  at  $6 R_*$  as displayed in Figure 30. Because silicates form at larger radii than alumina, the impact of increasing the gas number density on the grain size is weaker than for alumina, which forms in very dense layers at  $r \leq 2 R_*$ . However, any inhomogeneity in the inner wind will result in the efficient synthesis of a population of large grains for both materials, and contribute to gas drag and wind acceleration close to the star.

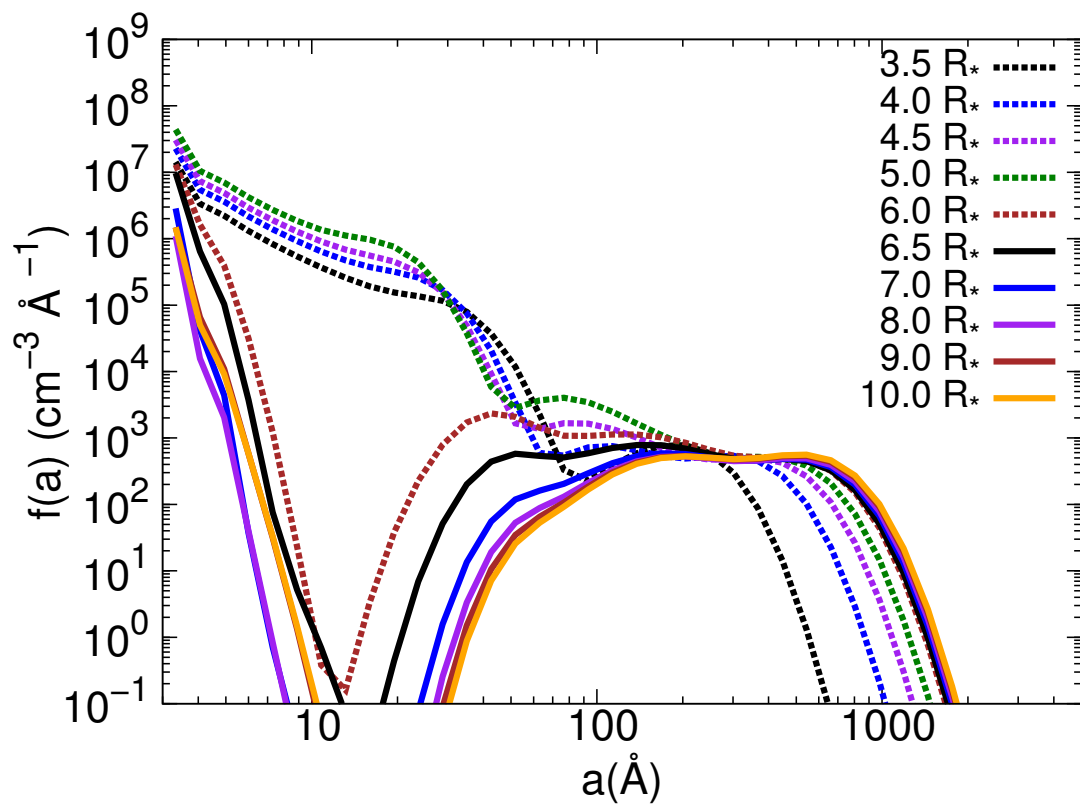


Figure 30: Forsterite grain size distributions as function of the radius / number of excursions in the  $\times 10$  density case.

## 6 Results for Semi-regular Variables

For the SRV of type SRb, stellar parameters of L<sup>2</sup> Puppis were used as input for modelling. Owing to its high temperature ( $T_* = 3380\text{K}$ ), its short period ( $P=140$  days), and its very low mass-loss-rate ( $\sim 10^{-9} M_\odot/\text{yr}$ ), it belongs to the blue group of SRV characterised by Kerschbaum & Hron (1992). In addition, the mass of L<sup>2</sup> Pup is high and its radius small leading to a small pressure and density scale heights.

The SRV model parameters for type SRa - a mixture of SRbs and intrinsic Miras - were chosen according to the star W Hydrae. This star is classified as a SRV of type SRa, although it has been questioned, as its visual amplitude ( $m_V=3.9$ ) exceeds the Galactic Catalogue of Variable Stars (GCVS) limit (Uttenthaler et al., 2011; Hinkle et al., 1997). From its light variation and period-luminosity relation, W Hya is classified as Mira variable. However, the velocity variation during one cycle clearly indicates that W Hya belong to the class of SRVs.

Other SRa sources lack either reliable stellar quantities or molecular observations. In addition, objects like WHya could represent a group of stars evolving from the SRV stage to the Mira stage (Hinkle et al., 1997) thus representing a SRV of the red group. For these reasons, the focus is on W Hya, which has been recently studied with Herschel (Khouri et al., 2014a,b)

### 6.1 Initial Photospheric Abundances

The C/O ratio is increasing with the age of a low-mass AGB star. As SRVs represent an evolutionary stage preceding the Mira Variable phase, SRVs should have a C/O ratio smaller than Miras. As C/O ratios are difficult to assess observationally (see discussion in Section 5.1, the TE calculation of SRV photospheres relies on theoretical stellar evolution models. For the SRb case, a C/O ratio of 0.5 is adopted, which corresponds almost exactly to the FRUITY evolutionary model with  $M_*^{ini} = 2 M_\odot$ ,  $Z = Z_\odot$  and TDU episode 3 over a total of 9 thermal pulsing episodes. This is consistent with the mass of L<sup>2</sup> Pup ( $1.7 M_\odot$ ) and with the early evolutionary stage on the AGB. For the SRa source, a C/O ratio of 0.65 represents also the  $M_*^{ini} = 2 M_\odot$ ,  $Z = Z_\odot$  model, but at the subsequent TDU 4 (of nine). This is consistent with the evolutionary phase of SRa variables and with the suggestion by Khouri et al. (2014a) for the initial mass of W Hydrae.

In the TE calculation, not only the C/O ratio impacts the molecular equilibrium abundances, but also the higher photospheric temperatures (compared to the Mira case). Particularly in the SRb case where  $T_* = 3380$  K, the equilibrium is shifted towards atoms rather than molecules (see Table 14). Despite the fact that the C/O ratio is lower in the SRb model (C/O=0.5) than in the SRa case (C/O=0.65), oxygen-bearing molecules such as H<sub>2</sub>O or SO are more abundant in SRa case at TE. As the photospheric (preshock) densities are the same for both types of modelled stars, it is the mainly photospheric temperature causing the differences in TE abundances.

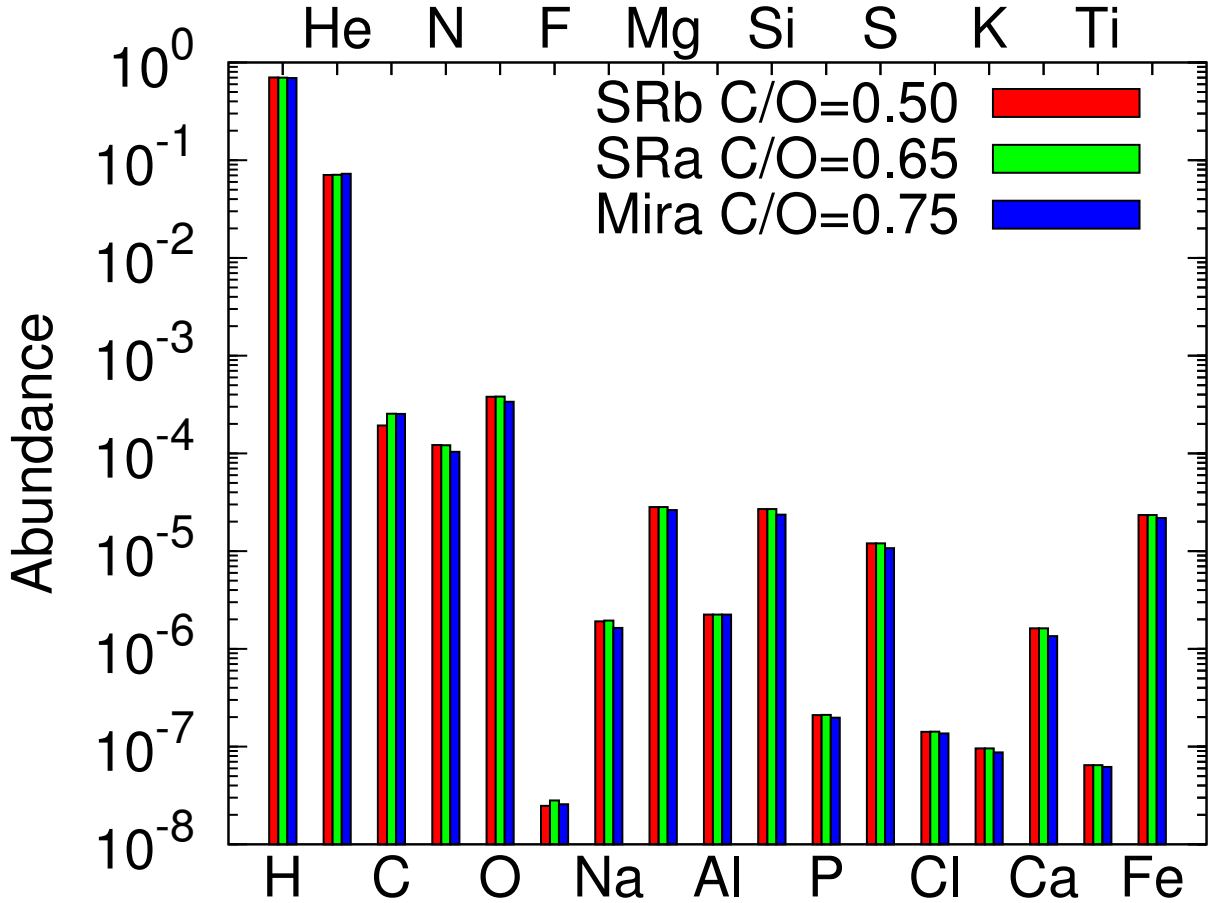


Figure 31: Elemental abundances (model input) for the SRb, the SRa and the Mira case. All of the cases are characterised by a distinct C/O ratio.

Table 14: Photospheric TE abundances for the SRb and the SRa case.

TE abundance	SRb star	SRa star
H	9.07(-1)	7.78(-1)
H <sub>2</sub>	7.01(-4)	1.19(-1)
H <sub>2</sub> O	5.72(-10)	1.87(-5)
CO	2.44(-4)	3.59(-4)
CO <sub>2</sub>	2.51(-11)	9.25(-9)
HCN	1.61(-11)	1.56(-12)
CS	1.61(-11)	3.63(-12)
SiO	5.20(-7)	3.87(-5)
SiS	1.32(-10)	2.53(-9)
SO	4.17(-11)	1.20(-8)
SO <sub>2</sub>	1.98(-17)	2.05(-12)

## 6.2 Post-Shock Chemistry

Despite their low TE abundances, molecules form in the cooling post-shock gas at  $1 R_*$  of the SRb model. Nevertheless, the newly formed molecules convert to atoms again, when moving to larger radii. This happens owing to short scale heights (see Equation 20) leading to a rapid decrease in gas densities. The validity of the model is constraint to radii smaller

than  $2.4 R_*$ . Inside  $2.4 R_*$ , high temperatures prevail for the SRb case, which affects the chemistry.

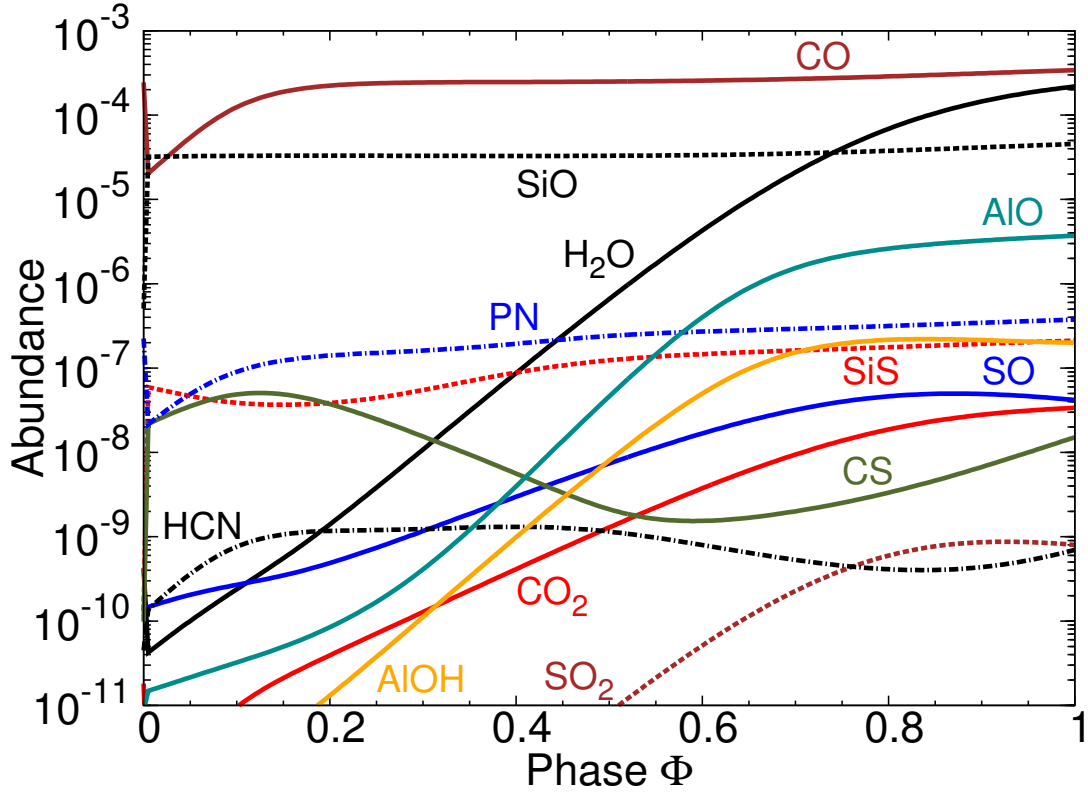


Figure 32: Modelled SRb abundances of the prevalent molecules as a function of pulsation phase  $\Phi$  in the parcel excursion at  $1R_*$ .

In Figure 32, the abundances of the prevalent species in the first excursion at  $1 R_*$  is shown for the SRb case. In comparison with the Mira case, most of the molecules reform at later phase, which can be explained, on the one hand, by the shorter pulsation period  $P=140$  days, and on the other hand, by the higher gas temperatures in the post-shock gas. In the case of aluminum-bearing species, AlO is more abundant than AlOH for the full parcel excursion. Firstly, AlO is not depleted in alumina dust, and secondly, at the high post shock temperatures, the AlO formation is favoured over AlOH formation. Albeit the temperatures are high, the carbon-bearing species HCN,  $\text{CO}_2$  and CS are less abundant compared to the Mira case, which can be attributed to the low C/O ratio of 0.5.

Already for  $r \geq 1.5R_*$ , the gas is predominantly atomic, as can be seen in Figure 33. Therefore, this model is constrained to a gas shell very close to the star, at  $1 R_*$ . Test runs with a frozen  $\text{H}/\text{H}_2$ -ratio for  $r \geq 1.5 R_*$  were performed, in order to derive trends for molecular abundances and the alumina dust production. In this test case, the molecular abundances of the prevalent species illustrated in Figure 33 stay roughly constant and the alumina dust formation remained inefficient.

In the SRa model, the situation is different. Larger scale heights and lower gas temperatures prevail, and thus the inner wind is not constrained to a thin shell, like in the SRb case.

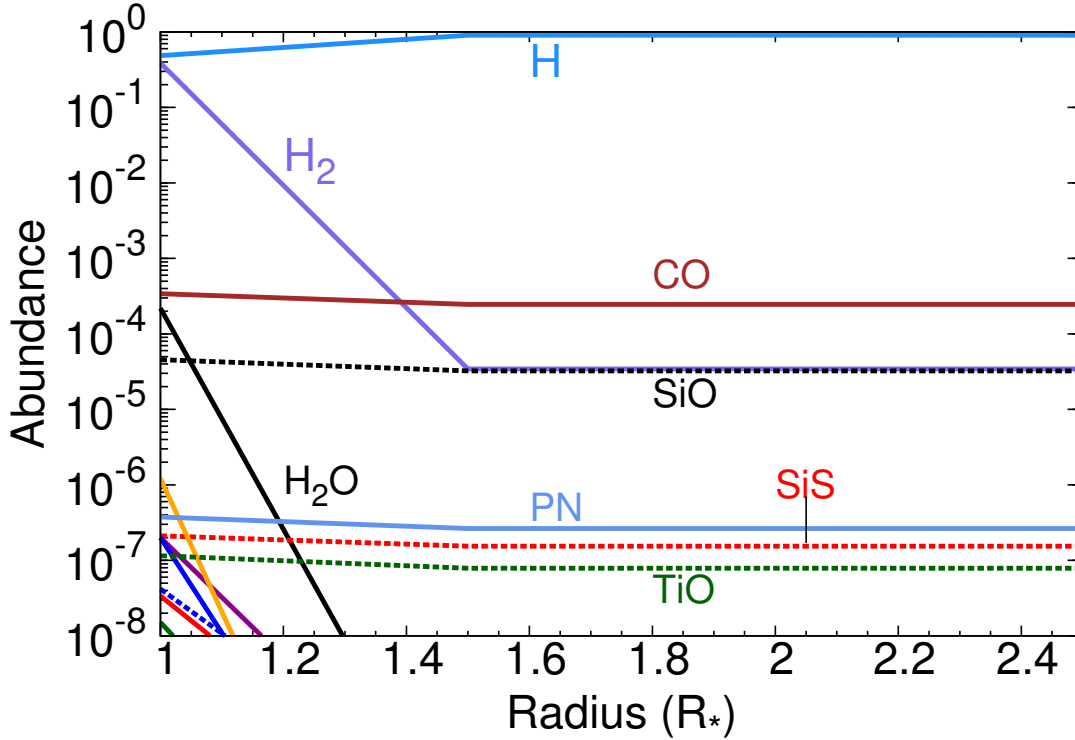


Figure 33: Modelled SRb abundances versus radial position in the range 1 - 2.4  $R_*$ .

The low expansion velocity of WHya ( $v_\infty = 7.5 \text{ km s}^{-1}$ ) (Khouri et al., 2014a) and a rather small pulsation amplitude ( $\Delta V = 11 \text{ km s}^{-1}$ ) (Hinkle et al., 1997) suggest a lower shock velocity than in IK Tau. Here, shock velocities of 10 and 20  $\text{km s}^{-1}$  were chosen.

The post-shock gas at 1  $R_*$  is shown in Figure 34. Apparently, the dissociation of CO is not very efficient at the beginning of the excursion, which can be explained by the low shock speed of 10  $\text{km s}^{-1}$  used in the SRa model. Moreover, trends in the molecular abundances, similar to those for Mira stars, are observed. AlOH forms at the expense of AlO at late phase, and the carbon-bearing species HCN,  $\text{CO}_2$  and CS do form. The sulphur oxide molecules SO and  $\text{SO}_2$  start to reform at early phase, but their abundance decreases again at late phase, owing to CS formation.

A 20  $\text{km s}^{-1}$  shock in the SRa model would result in a transition from molecular to atomic dominated gas around 2.5  $R_*$ . Owing to the above velocity and amplitude, a 10  $\text{km s}^{-1}$  shock seems to be more appropriate. The results for the semi-regular SRa with a 10  $\text{km s}^{-1}$  shock are presented in Figure 35. CO and  $\text{H}_2$  form in similar amount as in the Mira models. SiO is not depleted, as no silicate grains form (see Section 6.3). The carbon-bearing species HCN and CS decrease around 1.5 - 2  $R_*$ , whereas  $\text{CO}_2$  increases in this region. Moreover, SO and  $\text{SO}_2$  form and  $\text{H}_2$  is partially destroyed in the same region around 1.5 - 2  $R_*$ . The other prevalent molecules exhibit rather constant abundances with respect to the radial position.

In Figure 36, the observational values of the few detected species CO,  $\text{H}_2\text{O}$  and SiO are presented along with our modelled molecular abundances. In addition, HCN is plotted, as in the recent Herschel survey of the SRa star W Hya (Khouri et al., 2014b), HCN lines

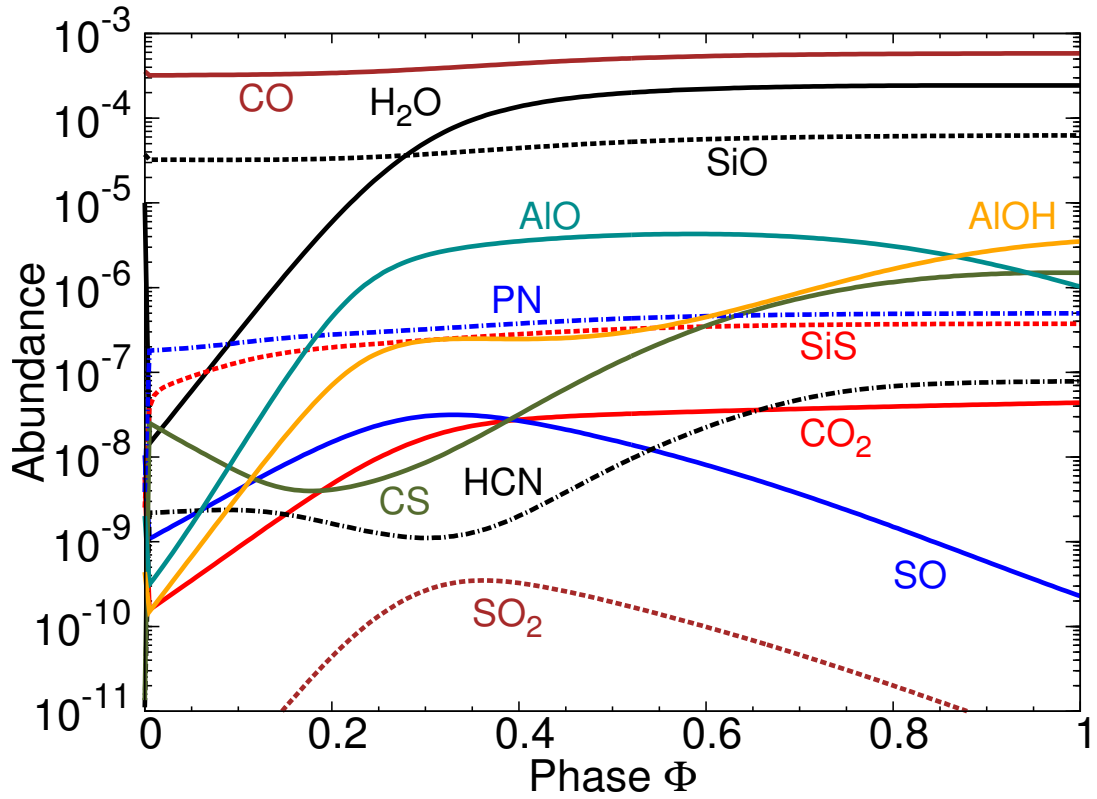


Figure 34: Modelled SRA abundances versus pulsation phase  $\Phi$  at  $1 R_*$  in the  $10 \text{ km s}^{-1}$  shock.

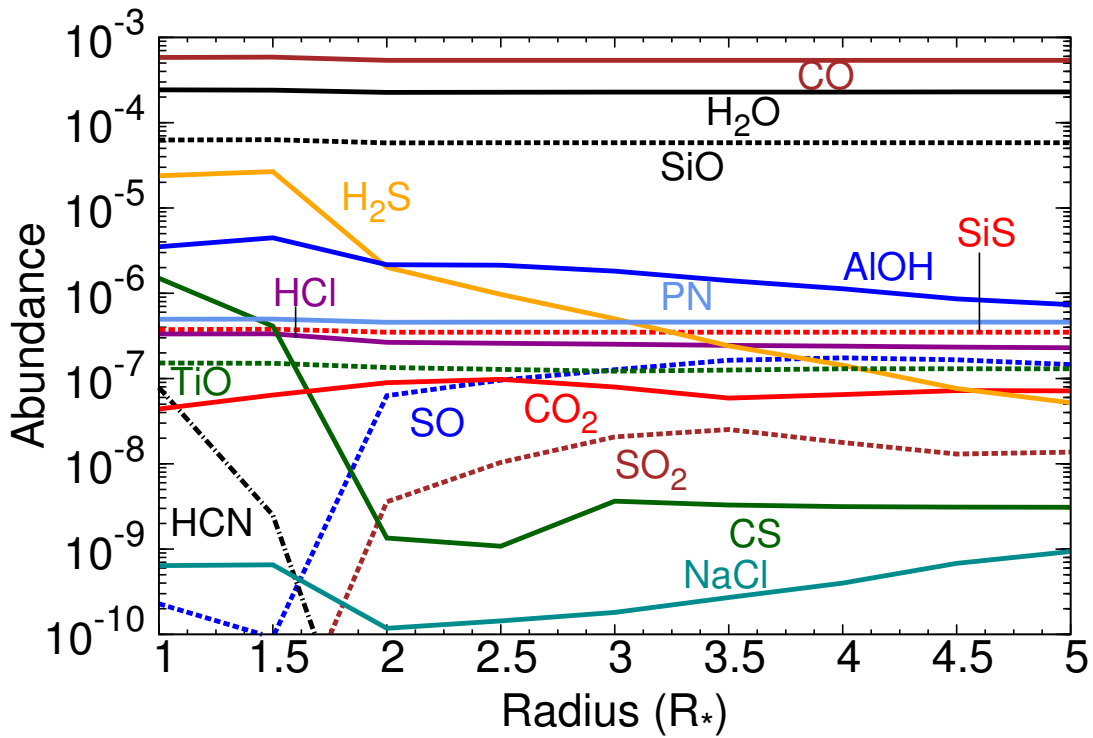


Figure 35: Modelled SRA abundances with respect to the position in the envelope for a  $10 \text{ km s}^{-1}$  shock.

were detected. The HCN lines originate from the innermost layers of the envelope, with a fractional abundance of the order of  $10^{-5}$ . The modelled abundances of CO, H<sub>2</sub>O and

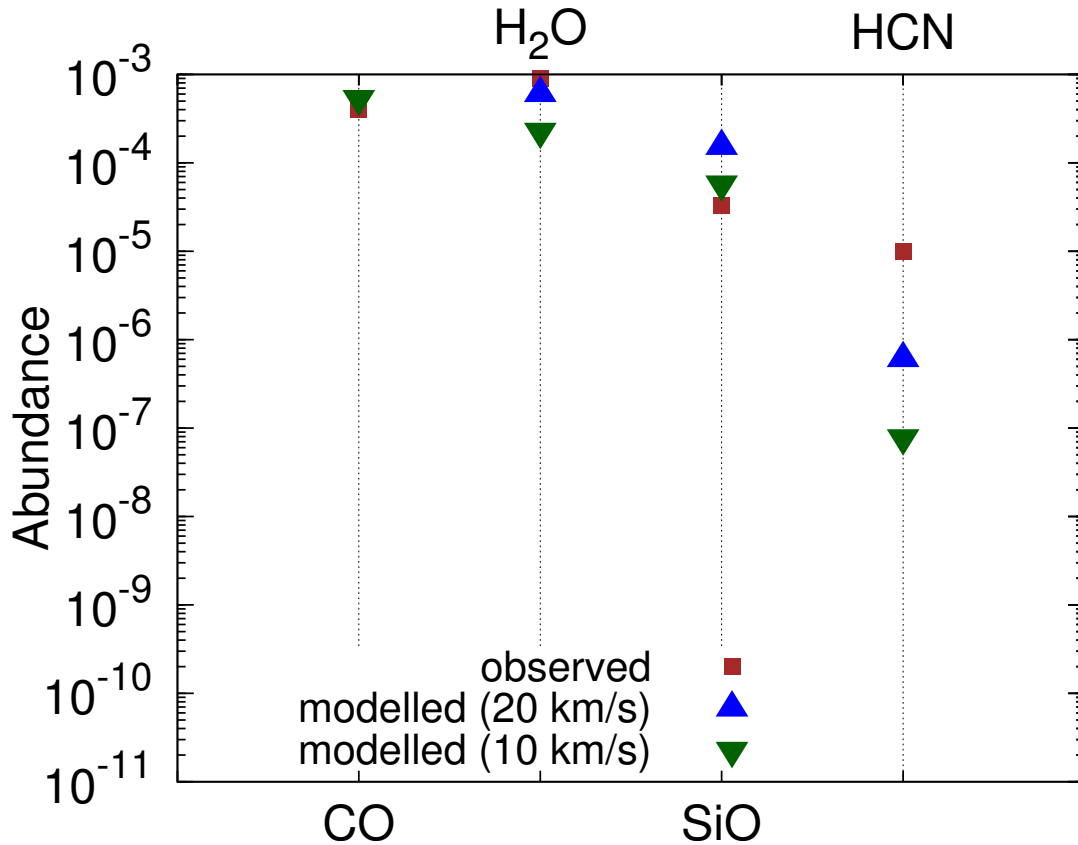


Figure 36: Modelled SRa abundances compared to observations in W Hya. The modelled values correspond to  $5 R_*$ , except HCN is evaluated at  $1 R_*$ .

SiO at  $5 R_*$  agree well with these recent Herschel observations for both models, the  $10 \text{ km s}^{-1}$  and  $20 \text{ km s}^{-1}$ , as can be seen in Figure 36. The modelled HCN abundances are lower than those derived by observations. However, the observational HCN abundance is a preliminary estimate, and the HCN presence in layers very close to star is reproduced by our models. The modelled abundance cannot discriminate between the shock speeds. A  $10 \text{ km s}^{-1}$  shock speed seems more plausible in view of the observed velocity of W Hya.

Figure 35 demonstrates that SiO is not depleted at radii  $r \geq 3.5 R_*$ , consistent with Figure 38, which shows the absence of silicate dust in the SRa model. HCN disappears for  $r \geq 2.5 R_*$ , which confirms its origin from the innermost layer. The modelled abundance hardly vary after  $3.5 R_*$ , which is a consequence of the low gas densities at this radius in the SRa model. The low gas densities prevent most of the gas phase reactions, owing to a reduced gas collision probability.

### 6.3 Clusters and Dust Grains

Although forsterite dimers become abundant and available for condensation around  $4 R_*$ , grains hardly form in the SRa case. It is due to low gas number densities around  $4 R_*$ . At densities as low as  $10^9 \text{ cm}^{-3}$ , the forsterite dimers do not coagulate efficiently and cannot produce larger grains. For alumina grains, the situation is different. They form close to the



star, where still high densities prevail. Their average grain size at  $2 R_*$  is  $\sim 200 \text{ \AA}$ . The alumina dust-to-gas mass ratio is  $5.3 \times 10^{-8}$  and thus considerably smaller than in the Mira models.

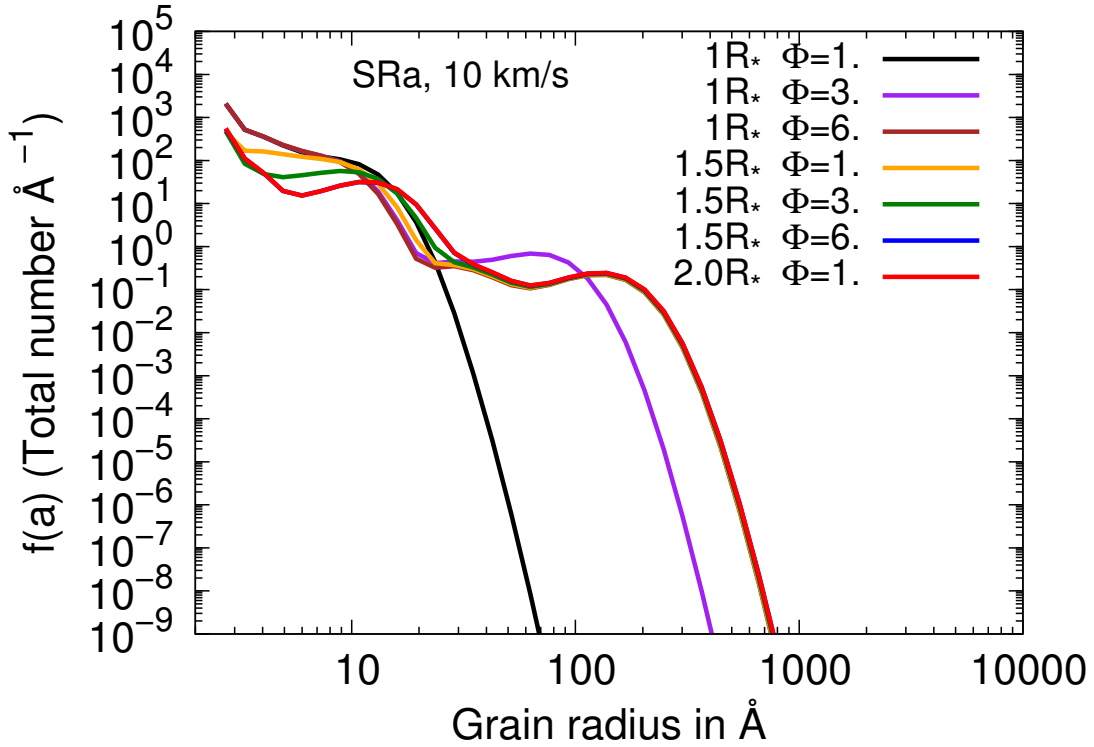


Figure 37: Alumina grain size distribution for the SRa model and a  $10 \text{ km s}^{-1}$  shock as function of radius.

The forsterite grain size distribution in Figure 38 clearly demonstrates that no forsterite grains form in the SRa model. The grain size distribution is dominated by the contribution of dimers with a size of  $\sim 3 \text{ \AA}$ . This is in contrast to the findings of Khouri et al. (2014b), in which about one-third of the silicon atoms are locked up in dust grains. Moreover, a dust-to-gas mass ratio of  $2.2 \times 10^{-3}$  is derived, according to the observed mass-loss rates and an adopted dust mass loss rate. Their dust composition mainly consists of astronomical silicates (58 % of the total dust mass). However, alumina grains and  $\text{H}_2\text{O}$  close to the star may be responsible for the dust emission (Zhao-Geisler et al., 2011). The latter study agrees with our findings, as alumina grains, as well as water, are abundant in the layers close to the star.

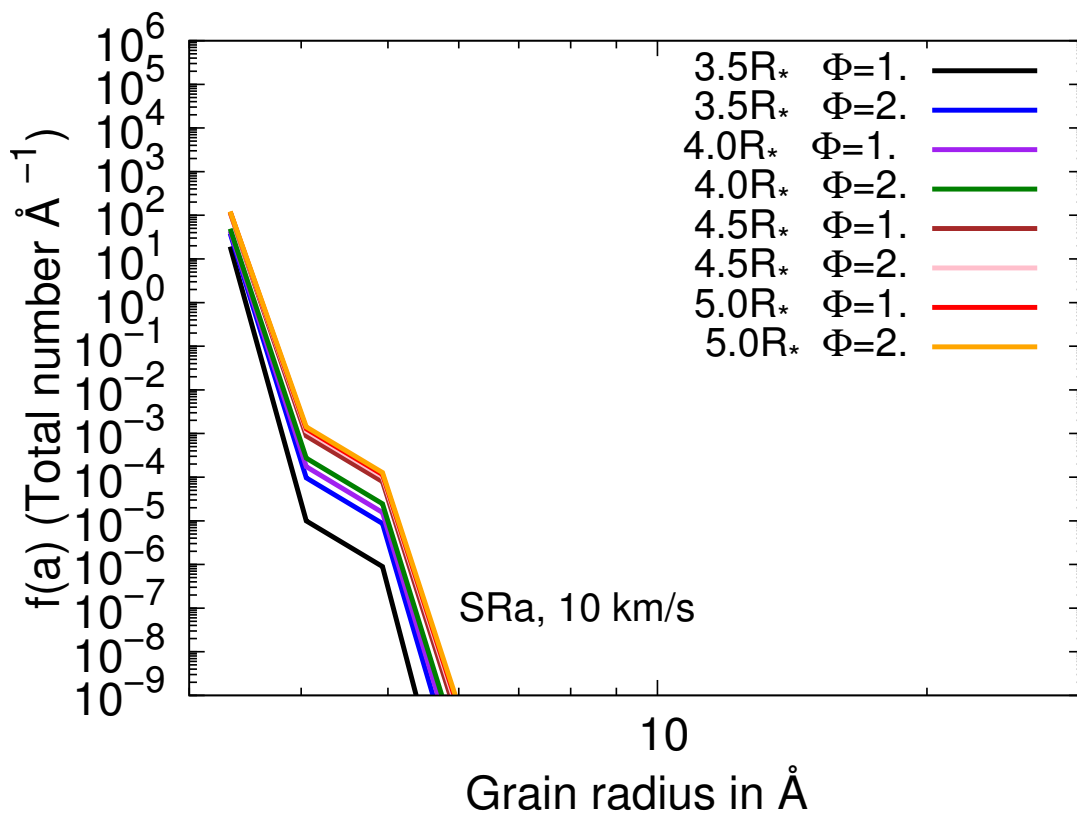


Figure 38: Forsterite grain size distribution for the SRa model and a 10 km s<sup>-1</sup> shock as function of radius.

## 7 Results for S-type AGB Stars

The best studied S type stars comprise W Aquilae and  $\chi$  Cygnus. W Aquilae is an MS star, whereas  $\chi$  Cygnus is MC star. Both types, MS and MC stars, have a C/O ratio close to 1. MS stars are slightly oxygen-rich, whereas MC have a bit more carbon than oxygen in their photosphere. Since the chemical network was initially constructed for an oxygen-rich environment, the focus is on C/O ratios smaller than unity, although close to 1. A C/O ratio greater than unity would imply a predominantly carbon-rich chemistry. It would include also molecules and reaction mechanisms not included in the current network (e.g. hydrocarbon chains, aromatic compounds). Our modelled results are thus compared to observations of W Aquilae. Three distinct shock velocities ( $10 \text{ km s}^{-1}$ ,  $20 \text{ km s}^{-1}$ , and  $32 \text{ km s}^{-1}$ ) are modelled for the S-type pulsator model, in agreement with measured shock velocities by Hinkle et al. (1997). The authors find a typical velocity amplitude for Mira of 20 - 30  $\text{km s}^{-1}$  in the radial direction. Therefore, we here consider the 20 and 32  $\text{km s}^{-1}$  shocks to test the post-shock chemistry.

### 7.1 Initial Photospheric Abundances

As initial elemental input, we choose the FRUITY evolutionary model with  $M_*^{ini} = 2 M_\odot$ ,  $Z = Z_\odot$ , and third dredge-up (TDU) episode 5 over a total of 9 TDU episodes, which results in a C/O ratio of 0.85. The C/O ratio is rescaled to the value of 0.95 in order to account for MS type stars. The rescaling seems a bit artificial, because TDU episode 6 of 9 would correspond to a C/O ratio above unity. In addition, our models cover a sequence of subsequent dredge-up episodes: Dredge-up episode 3 was used in the SRb case, TDU 4 for the SRa star, and TDU 5 for S-type AGB stars, respectively.

The TE calculation is performed at  $n_0 = 3.6 \times 10^{14}$  and at  $T = 1800 \text{ K}$  appropriate for a S-star like W Aquilae.

Table 15: Photospheric TE abundances for the S-type and the Mira case.

TE abundance	S-type	Mira
H	3.41(-2)	3.76(-1)
H <sub>2</sub>	7.98(-1)	4.83(-1)
H <sub>2</sub> O	3.04(-5)	1.01(-4)
CO	8.02(-4)	4.91(-4)
CO <sub>2</sub>	8.18(-9)	1.97(-8)
HCN	3.45(-11)	3.07(-12)
CS	2.92(-10)	9.41(-12)
SiO	5.84(-5)	4.57(-5)
SiS	4.44(-6)	1.92(-8)
SO	4.02(-9)	2.10(-8)
SO <sub>2</sub>	4.24(-13)	6.53(-12)

## 7.2 Post-Shock Chemistry

In Figures 39 and 40, the abundances of the prevalent molecules versus radius are shown. The modelled carbon-bearing species CS, HCN and CO<sub>2</sub> are expected to be enhanced in abundance, compared to IK Tau. The inspection of these Figures reveals that CS has an enhanced abundance ( $\sim 10^{-5}$ ), followed by HCN, which decreases for radii greater than 1  $R_*$ , and reforms at larger radii. CO<sub>2</sub> plays a minor role in the models. Furthermore, the sulphur oxides, SO and SO<sub>2</sub>, are suppressed, as the sulphur is locked in CS and SiS. These abundances reflect the S-type AGB phase with a C/O ratio close to unity, and a smaller amount of oxygen-bearing species is found. As the pulsation physics of S-type stars is not well characterised and several galactic S-type stars are considered, we focus on two shock velocities, 20 and 32 km s<sup>-1</sup>.

Abundances values (with respect to H<sub>2</sub>) derived from observations are listed in Table 16 for various S-type stars and detected molecules. The latter comprise the molecules CO, H<sub>2</sub>O, SiO, HCN, NH<sub>3</sub>, HCl, SH, H<sub>2</sub>S and TiO observed in several galactic S-type sources. In the following, the observed species are discussed and compared to the 20 km s<sup>-1</sup> and the 32 km s<sup>-1</sup> model.

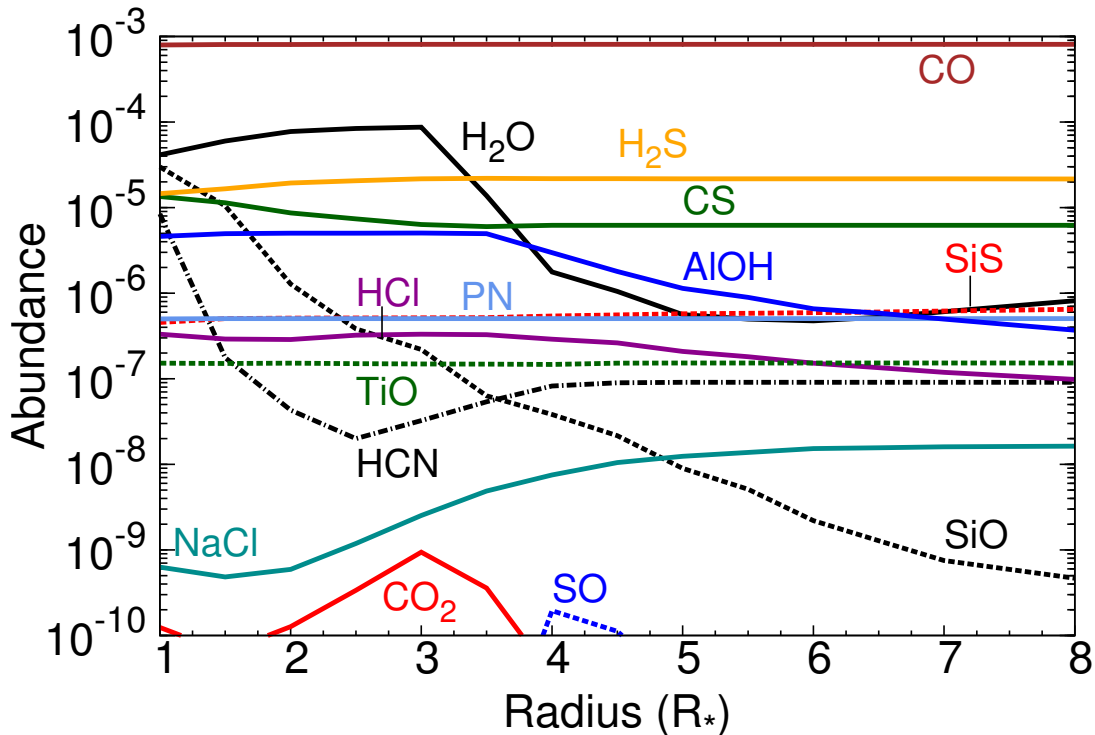


Figure 39: Modelled S-type star abundances of the prevalent molecules as function of the radial position for a 20 km s<sup>-1</sup> shock.

The most drastic difference between the two different shock speeds is reflected in the H<sub>2</sub>S, CS, and HCN. In the 20 km s<sup>-1</sup> shock model, the species abundances show no strong variation with radius. In the 32 km s<sup>-1</sup> shock model, the molecular abundances H<sub>2</sub>S, CS and HCN show a rather erratic behaviour for  $R \geq 3.5 R_*$ . The dust formation occurs for

both shock speeds, in a similar efficiency and amount, as can be seen in Table 17.

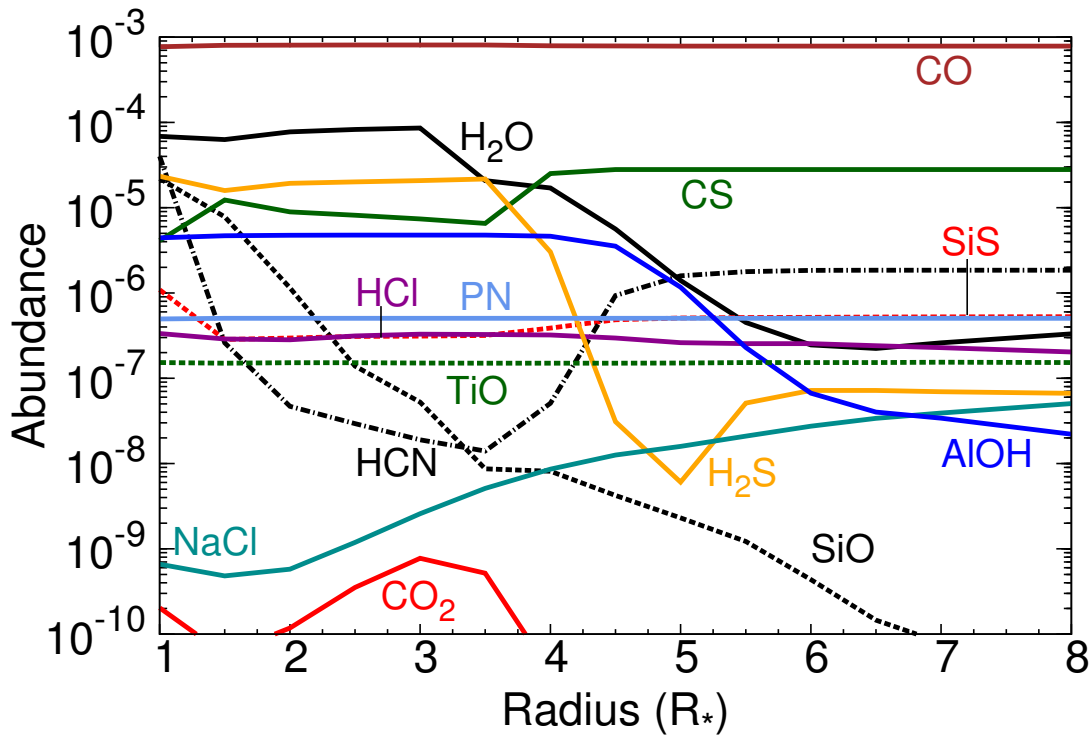


Figure 40: Modelled S-type star abundances of the prevalent molecules as function of the radial position for a  $32 \text{ km s}^{-1}$  shock.

In Figure 41 Observational abundances are compared with our modelled abundances at  $5 R_*$ . The CO abundance agrees very well with observations for both shock speeds. In addition, observations of S-type stars indicate a higher CO abundance ( $\sim 6 \times 10^{-4}$ ) than in Mira stars ( $\sim 2 \times 10^{-4}$ ). This is also the case for the corresponding models presented in this thesis.

The observational water abundance is  $(1 - 2) \times 10^{-5}$ . This is higher than the modelled values around  $6 - 8 R_*$  (see Figure 41). However, in the gas layers located at  $3 - 5 R_*$ , the  $\text{H}_2\text{O}$  abundance decreases significantly owing to silicate clusters formation. In these layers,  $\text{H}_2\text{O}$  is consumed by the oxidation of clusters. The  $\text{H}_2\text{O}$  abundance at  $3.5 R_*$  fits the observations well, as can be seen in Table 16 and Figures 39 and 40.

The modelled HCN fits the most recent observations well in the  $32 \text{ km s}^{-1}$  shock model. In the  $20 \text{ km s}^{-1}$ , however, a deviation of a factor  $\sim 30$  is found. The HCN abundance is therefore sensitive to the shock strength and its abundance could serve as an indicator for the shock physics in S-type AGB stars. The remaining nitrogen is locked in  $\text{N}_2$ , and  $\text{NH}_3$  cannot be reproduced by the current models. The  $\text{H}_2\text{S}$  and SH observations relate to a circumstellar gas layer very close to the star ( $1.1 R_*$ ) and are in agreement with the present model. The HCl and TiO abundances agree well with observations for both shock speeds. In Figures 42 and 43, the first post-shock excursions for the two shock speeds are presented. In the beginning of the parcel, a difference in CO is detectable, which arises from different post-shock temperatures and gas densities. Moreover, HCN reaches a high value at the end

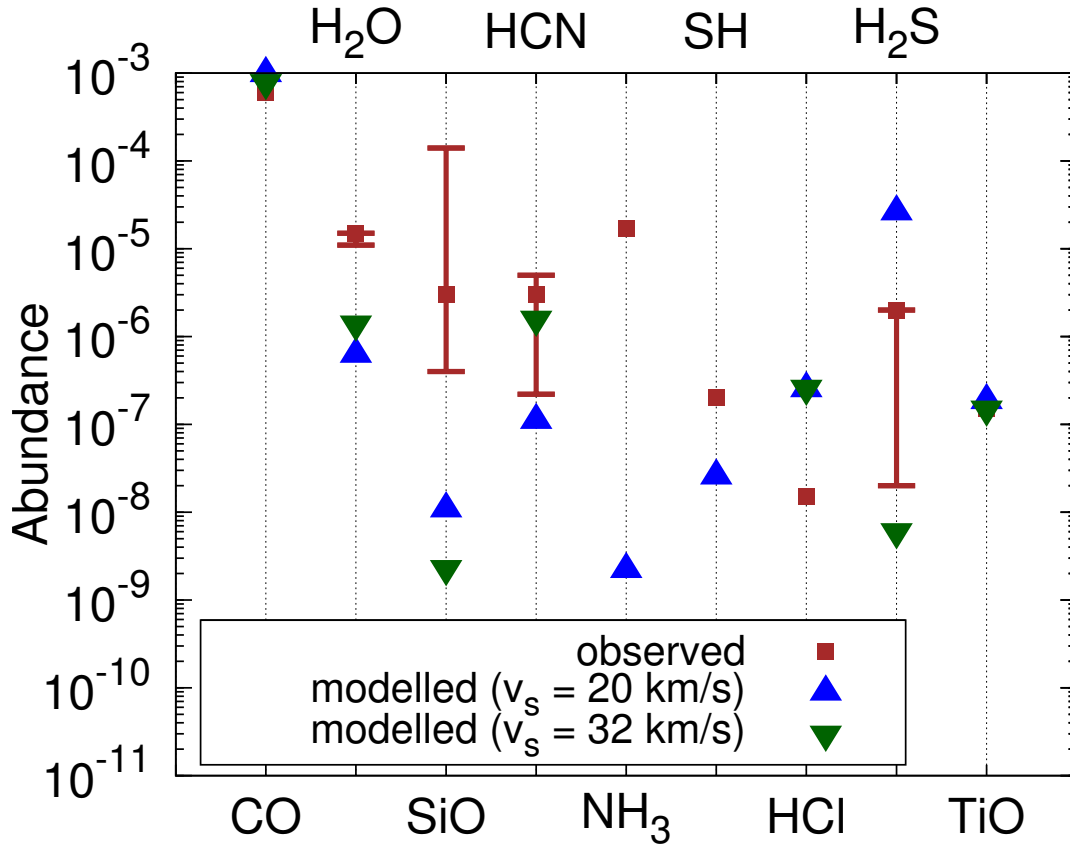


Figure 41: Modelled molecular abundances with respect to  $\text{H}_2$ ) at  $5 R_*$  in comparison with observationally derived values of S-type stars

of the excursion of the  $32 \text{ km s}^{-1}$  model ( $x(\text{HCN}) \sim 4 \times 10^{-5}$ ).

In comparison to observations, the modelled SiO abundance at  $6 R_*$  is 3-4 orders of magnitude lower. This discrepancy arises from the depletion of SiO into silicate dust grains. SiO is not only depleted in dust grains, but also decreases before silicate condensation occurs. The decrease in SiO is caused by the reaction with of H with HSiO. In the S-type star models, this barrierless reaction is enhanced in the region from 1 to  $4 R_*$ , as the densities are high compared to the Mira and SRV cases. The modelled SiO abundance with respect to  $\text{H}_2$  at  $2 R_*$  is  $x(\text{SiO}) = 1.5 \times 10^{-6}$  (for both shock speeds), and agrees with the most recent Herschel observations (Danilovich et al., 2014), as can be seen in Table 16 and Figure 39).

In conclusion:

- The modelled abundances agree well with observations for molecules not participating in cluster and dust formation.
- The modelled abundances for SiO and  $\text{H}_2\text{O}$ , actively participating in cluster formation, are lower compared to observations. However, their model abundances are greater than the observational values prior to the onset of silicate formation. It can be deduced that the cluster and dust formation in the present model can be too efficient.
- As for the Mira models, the amount of  $\text{NH}_3$  cannot be reproduced in the S-type AGB

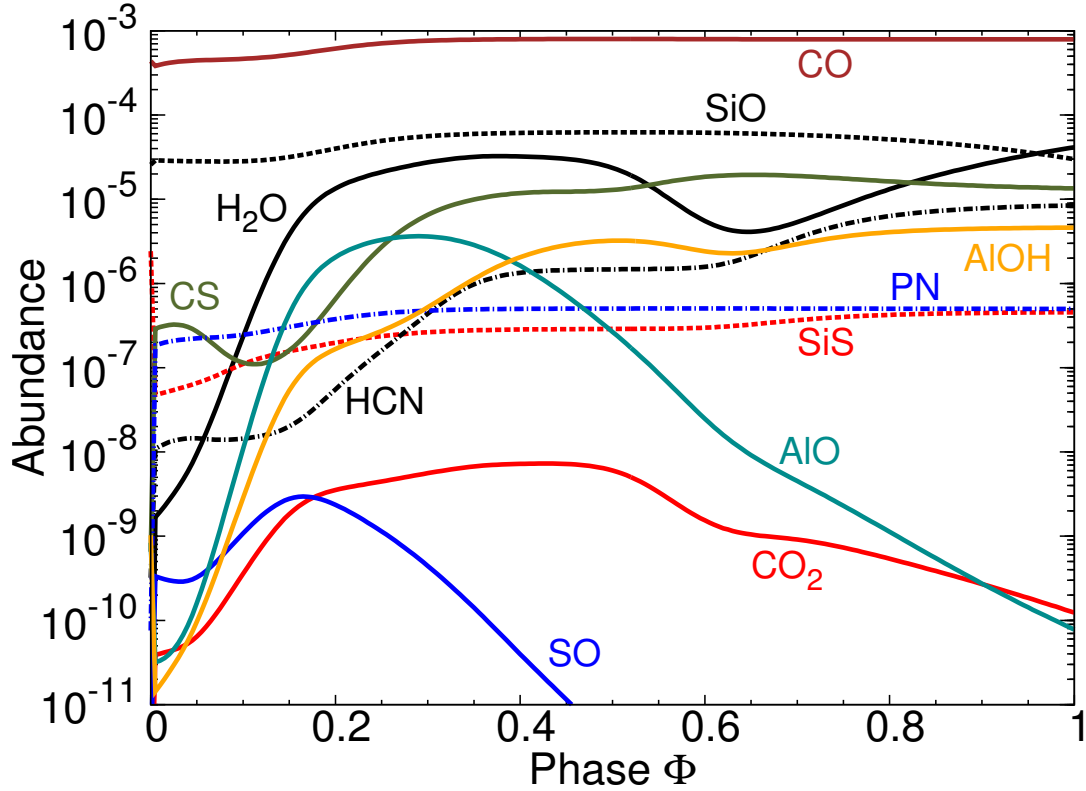


Figure 42: Modelled S-type star abundances of the prevalent molecules in the parcel excursion at  $1R_*$  for a  $20 \text{ km s}^{-1}$  shock.

model. Its presence thus indicates an origin not considered in this study (e.g. photochemistry, grain-surface chemistry).

Comparing the two different shock speeds, similar trends in the abundances are observable. Slight differences can, however, be observed. The collisional dissociation of CO is much stronger in the  $32 \text{ km s}^{-1}$  shock model. This is in particular apparent at early phase of Figure 42. Furthermore, the molecules start to reform at slightly later phase in  $32 \text{ km s}^{-1}$  shock model compared to the  $20 \text{ km s}^{-1}$  shock.

Apparently, the SiO abundance is decreasing with radius and the decrease is steeper than in the other considered cases. The barrierless reaction  $\text{SiO} + \text{H} \rightarrow \text{HSiO}$  is responsible for the strong decrease of SiO with radius. This HSiO formation is more efficient in S stars than in the Mira models, as the corresponding gas number densities are higher in the S star models.

### 7.3 Clusters and Dust Grains

Large amounts of oxygen-rich dust form in the S star models albeit less oxygen is available, compared to the Mira case (see Table 17). Both alumina and forsterite are enhanced compared to IK Tau by a factor of a few. To explain this paradoxical fact, further parameters have to be considered. The pulsation period is 490 days, which is quite close to the period of IK Tau (470 days). Hence, the timescales for condensation are large. Furthermore, the

Table 16: Molecular observations of galactic S-type AGB stars. An asterix (\*) denotes fractional abundances with respect to the total gas (all other values are with respect to H<sub>2</sub>).The notation X(Y)  $\equiv$  X  $\times$  10<sup>Y</sup> is used.

Source	Molecule	Abundance	Reference
R And	SH	2.0(-7)	Yamamura et al. (2000)
	HCl	1.5(-8)	Yamamura et al. (2000)
	H <sub>2</sub> S	< 2.0(-6)	Yamamura et al. (2000)
	HCN	2.2(-7)	Schöier et al. (2013) *
	SiO	(0.4-5.1)(-5)	Ramstedt et al. (2009) *
$\chi$ Cyg	CO	6.0(-4)	Justtanont et al. (2010),Schöier et al. (2011) *
	H <sub>2</sub> O	(1.1-1.2)(-5)	Justtanont et al. (2010),Schöier et al. (2011) *
	SiO	1.3(-5)	Schöier et al. (2011) *
	SiO	(1.0-1.3)(-5)	Ramstedt et al. (2009) *
	HCN	5.0(-6)	Schöier et al. (2011) *
	HCN	3.0(-6)	Schöier et al. (2013) *
	CN	1.9(-5)	Schöier et al. (2011) *
NP Augirae	TiO	1.5(-7)	Smolders et al. (2012)
W Aquilae	CO	6.0(-4)	Danilovich et al. (2014)
	H <sub>2</sub> O	1.5(-5)	Danilovich et al. (2014)
	SiO	3.0(-6)	Danilovich et al. (2014)
	SiO	(2-3)(-6)	Ramstedt et al. (2009) *
	HCN	3.0(-6)	Danilovich et al. (2014)
	HCN	7.0(-7)	Schöier et al. (2013) *
	NH <sub>3</sub>	1.7(-5)	Danilovich et al. (2014)
W And	HCN	5.0(-7)	Schöier et al. (2013)*
	SiO	1.2(-5)	Ramstedt et al. (2009)*
R Cyg	HCN	2.7(-7)	Schöier et al. (2013)*
	SiO	(3-4)(-6)	Ramstedt et al. (2009) *
S Lyr	HCN	4.5(-6)	Schöier et al. (2013) *
	SiO	1.0E(-5)	Ramstedt et al. (2009) *
40 sources	SiO	(4.0(-7) - 1.4(-4))	Ramstedt et al. (2009) *



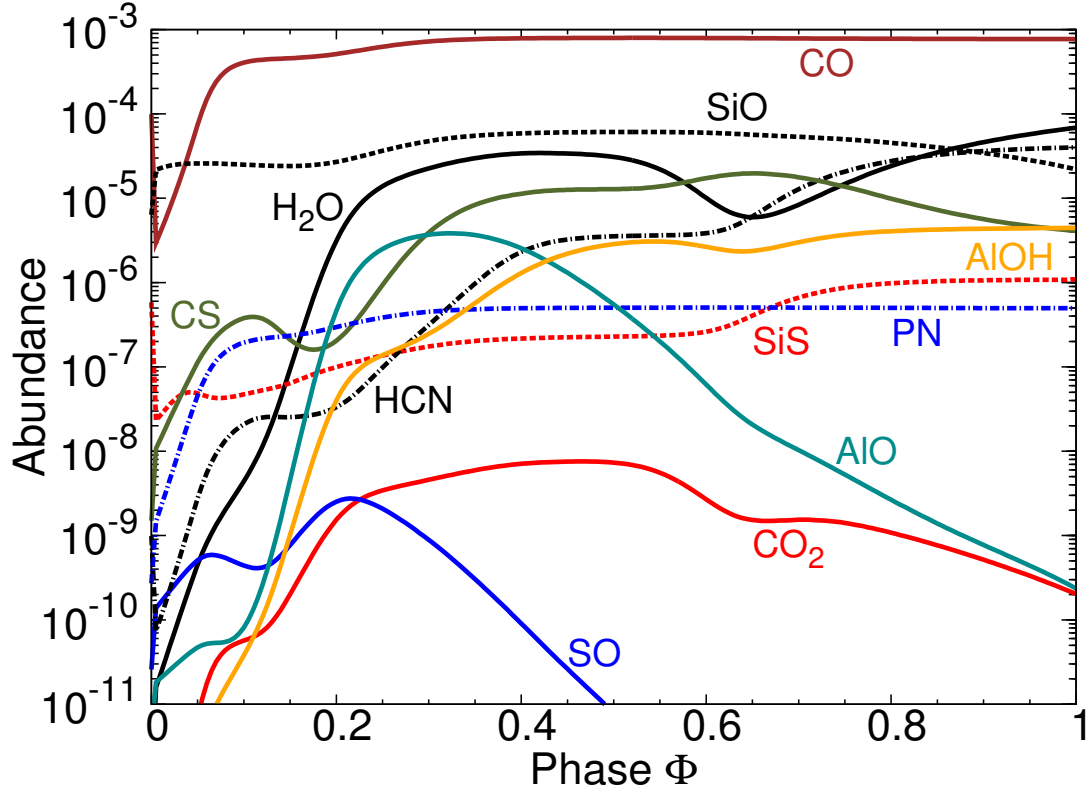


Figure 43: Modelled S-type star abundances of the prevalent molecules in the parcel excursion at  $1R_*$  for a  $32 \text{ km s}^{-1}$  shock.

Table 17: Comparison of the dust-to-gas mass ratios in the  $20 \text{ km s}^{-1}$  and  $32 \text{ km s}^{-1}$  of S-type stars with IK Tau. The notation  $X(Y) \equiv X \times 10^Y$  is used.

Radius ( $R_*$ )	S-type $20 \text{ km s}^{-1}$	S-type $32 \text{ km s}^{-1}$	IK Tau
1.0	3.5(-5)	8.0(-5)	2.1(-5)
1.5	4.6(-5)	1.1(-4)	2.7(-5)
2.0	5.7(-5)	1.4(-4)	3.3(-5)
3.5	2.2(-3)	2.0(-3)	1.3(-4)
4.0	2.7(-3)	2.9(-3)	4.6(-4)
4.5	2.9(-3)	3.5(-3)	6.0(-4)
5.0	3.0(-3)	3.9(-3)	7.3(-4)
6.0	3.3(-3)	4.4(-3)	1.0(-3)
7.0	3.7(-3)	5.3(-3)	1.4(-3)
8.0	4.1(-3)	5.8(-3)	1.7(-3)

large radius of  $6 \times 10^{13} \text{ cm}$  (more than twice the radius of IK Tau) results in huge scale heights, resulting in high gas densities at large radii. The high densities in combination with the rather low surface temperature ( $T = 1800 \text{ K}$ ) makes galactic S stars efficient dust factories, despite their comparable low oxygen abundance.

In Figures 44 and 45, the alumina grain size distributions for the S-type are presented for a  $20 \text{ km s}^{-1}$  and a  $32 \text{ km s}^{-1}$  shock, respectively. Large alumina dust grains are formed in high amounts. In both cases, two populations of grains are produced with sizes of  $\sim 540$

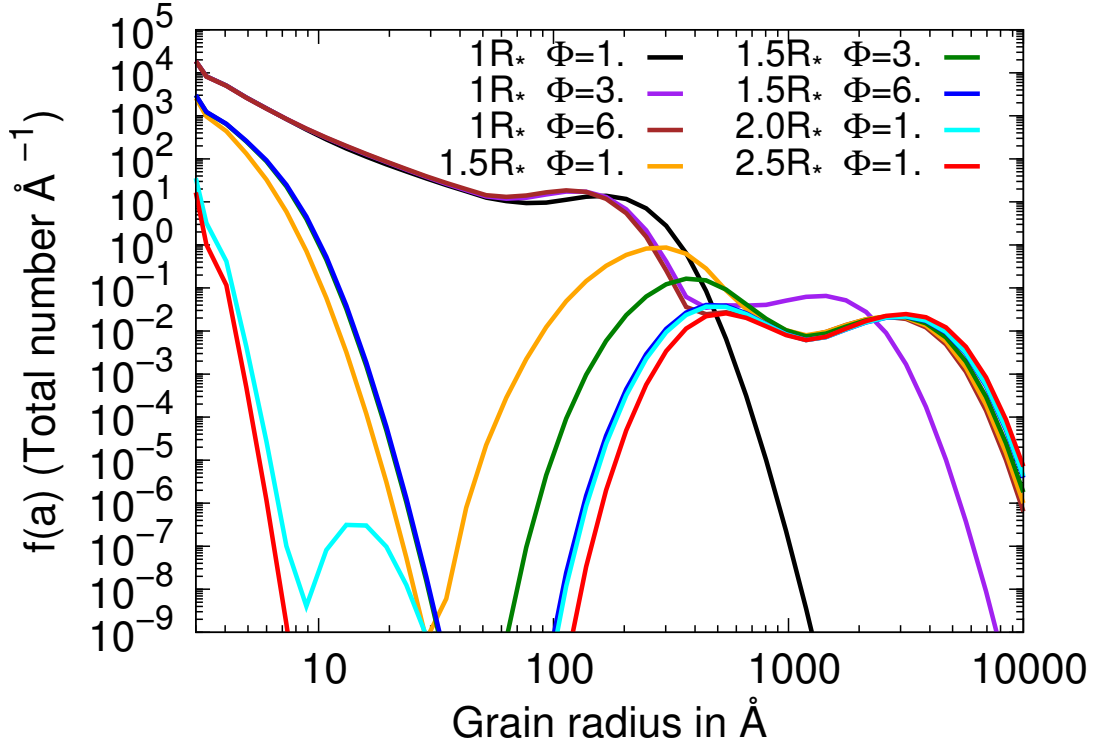


Figure 44: Alumina grain size distribution in S-type stars as function of radial distance to the stars for a  $20 \text{ km s}^{-1}$  shock.

$\text{\AA}$  and  $\sim 0.3 \mu\text{m}$  in the  $20 \text{ km s}^{-1}$  case, and  $\sim 800 \text{\AA}$  and  $\sim 0.5 \mu\text{m}$  in the  $32 \text{ km s}^{-1}$  case, respectively. The corresponding dust-to-gas mass ratios are listed in Table 17. These findings hint at the fact that S-type stars can produce high amounts of alumina dust. Moreover, the comparison between the two different shock speeds shows a more efficient alumina dust production in the  $32 \text{ km s}^{-1}$  shock model, owing to higher post-shock number densities and despite higher post-shock gas temperatures.

For silicates, the situation is similar to alumina. Grain size distribution are shown in Figures 46 and 47. Large grains form efficiently and lead to high dust masses, as can be seen from Table 17. However, in contrast to alumina, the grain size distributions exhibit just one dust size component, instead of 2. Furthermore, it is apparent in both models, that around  $5 - 6 R_*$ , almost no grains with sizes between  $30$  and  $100 \text{\AA}$  are present. Grains with these sizes have been either coagulated to larger grains or fragmented back to dimers.

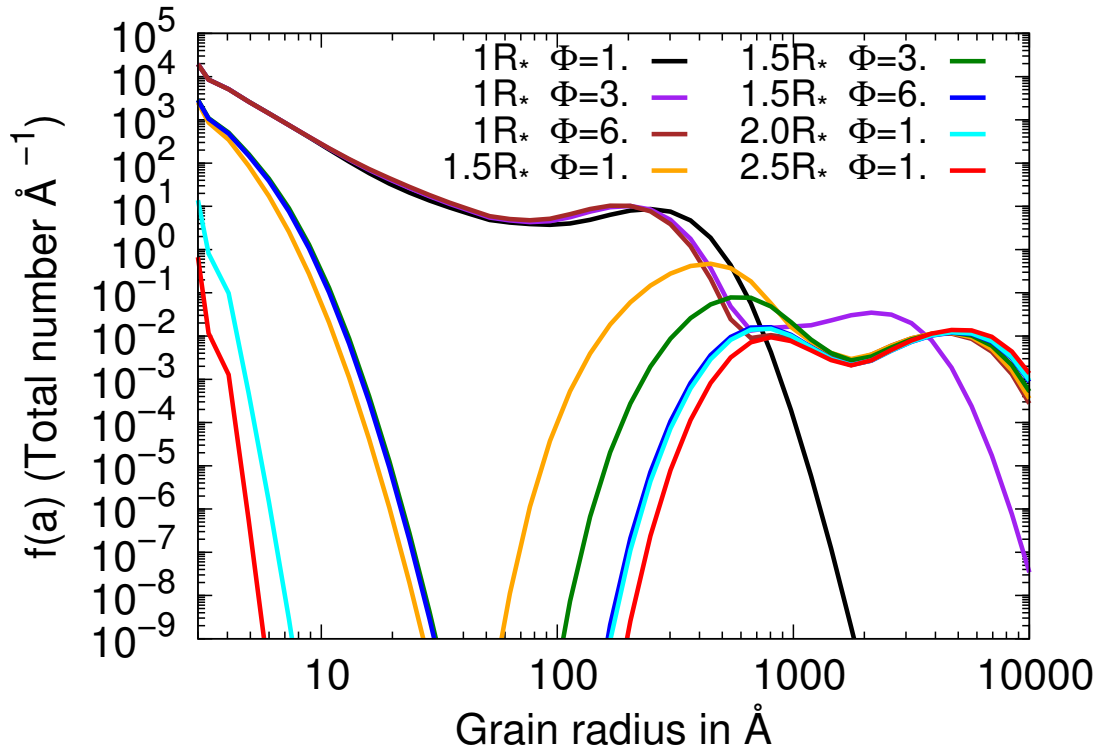


Figure 45: Alumina grain size distribution in S-type stars as function of radial distance to the stars for a  $32 \text{ km s}^{-1}$  shock.

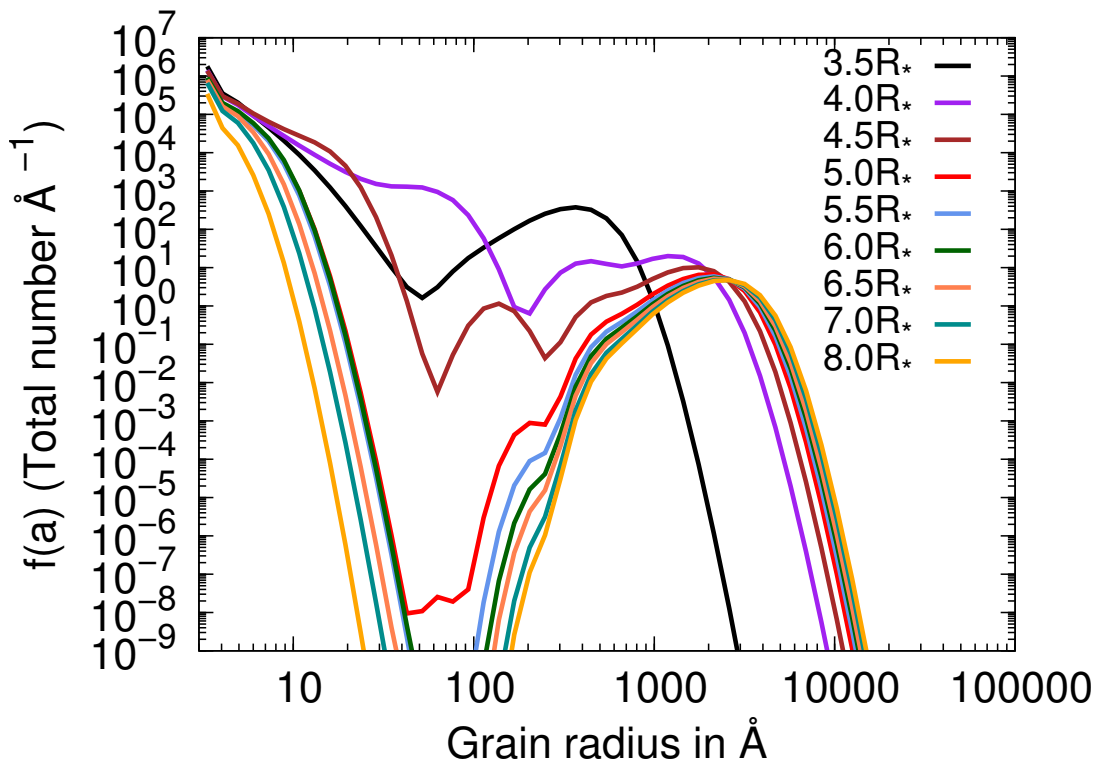


Figure 46: Forsterite grain size distribution in S-type stars as function of radial distance to the stars for a  $20 \text{ km s}^{-1}$  shock.

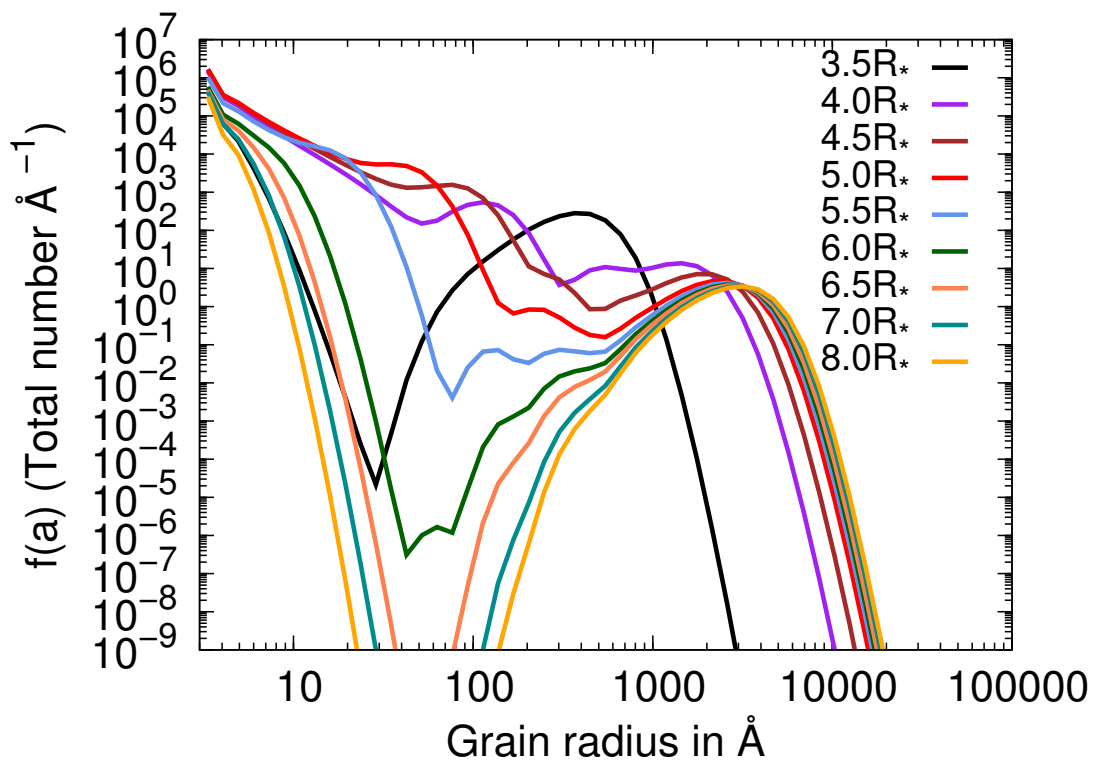


Figure 47: Forsterite grain size distribution in S-type stars as function of radial distance to the stars for a  $32 \text{ km s}^{-1}$  shock.

## 8 Results for Subsolar Metallicities

The results in this section refer stellar 'twins' of IK Tau in the Magellanic Clouds. The gas conditions (temperature, density and velocity) and the pulsation properties (period, shock strength) are identical to the IK Tau case, but subsolar metallicities, appropriate to the LMC and the SMC, are considered. This results in different initial elemental compositions.

### 8.1 Initial Photospheric Abundances

The initial elemental abundances were taken from the FRUITY  $Z=0.003$  and  $Z=0.008$  model accounting for the SMC and the LMC, respectively (see Figure 13). As the elements heavier than He are all less abundant at subsolar metallicity, 'metal'-bearing species are expected to have lower TE abundances. However, the amount of hydrogen is enhanced, therefore hydrides and molecular  $H_2$  should have higher TE abundances. Helium is a noble gas and thus does not contribute to molecular formation at TE. These trends are seen in the TE abundances of the prevalent photospheric molecules presented in Table 18

Table 18: Photospheric TE abundances for the SMC, the LMC and the solar metallicity case. The notation  $X(Y) \equiv X \times 10^Y$  is used.

Species	SMC	LMC	solar
H	3.78(-1)	3.77(-1)	3.76(-1)
$H_2$	4.89(-1)	4.86(-1)	4.83(-1)
$H_2O$	2.42(-5)	6.51(-5)	1.01(-4)
CO	1.18(-4)	3.18(-4)	4.91(-4)
$CO_2$	1.12(-9)	8.18(-9)	1.97(-8)
HCN	1.57(-12)	2.47(-12)	3.07(-12)
CS	2.28(-12)	6.11(-12)	9.41(-12)
SiO	1.11(-5)	2.98(-5)	4.57(-5)
SiS	4.68(-9)	1.25(-8)	1.92(-8)
SO	1.19(-9)	8.69(-9)	2.10(-8)
$SO_2$	8.83(-14)	1.69(-12)	6.53(-12)

### 8.2 Post-Shock Chemistry

In Figures 48 and 49, the modelled molecular abundances versus pulsational phase  $\Phi$  at  $1 R_*$  for the SMC and LMC models are presented. Molecules bearing heavy elements have lower abundances as the metallicity decreases. For example, silicon oxide, SiO, has a similar trend in all cases: its abundance decreases with the distance from the star. However, the lower the metallicity, the lower the SiO abundance at  $1 R_*$ . The proportion of the SiO abundances SMC:LMC:MW = 1:2.7:4.1 compares very well with the proportion of the SiO TE abundances SMC:LMC:MW = 1:2.7:4.2. From Figures 48 and 49, the destruction and the subsequent reformation of SiO can be seen. The difference between SMC and LMC model are the initial abundance at phase  $\Phi = 0$ , which are determined by the TE abundances.

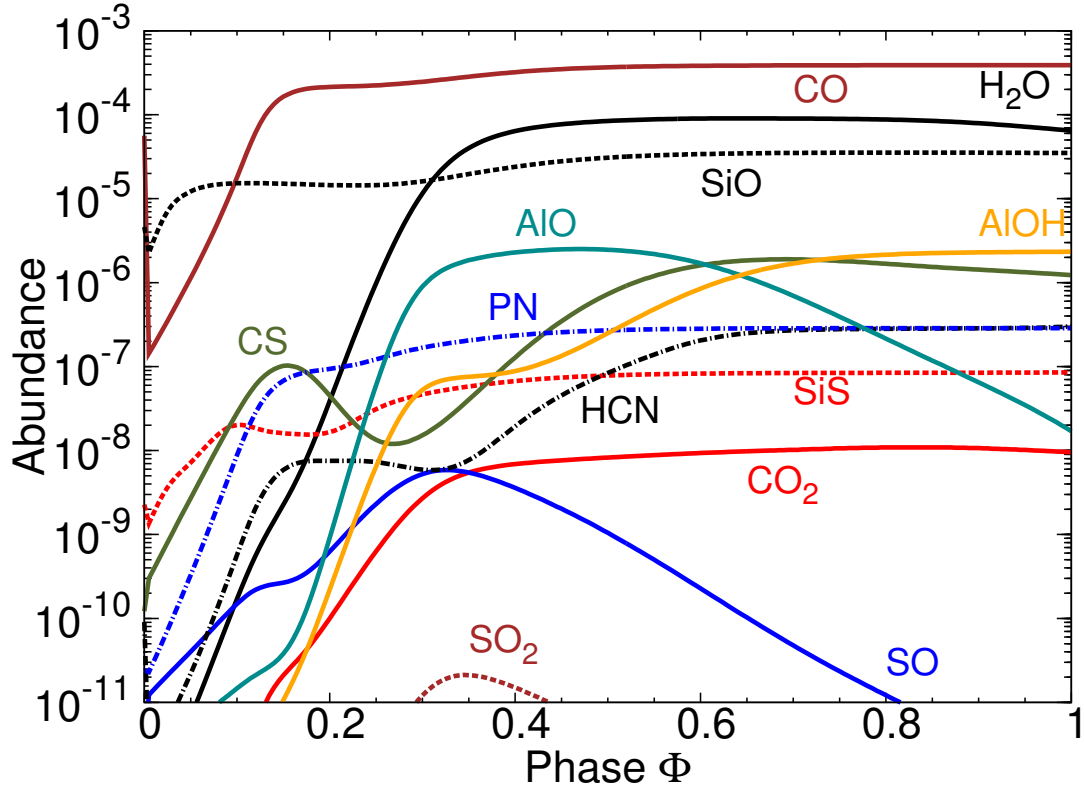


Figure 48: Molecular post-shock abundances as function of the pulsation phase  $\Phi$  in the first parcel at  $1 R_*$  of AGB star in the LMC ( $v_s = 32 \text{ km s}^{-1}$ ).

In the LMC, the trend in molecular abundances is similar to the Mira models, as can be seen in Figure 50. In the SMC, the low availability of heavy elements is apparent. The trends are similar to the LMC, however, the abundance curves are shifted towards lower values for most of the elements - see Figure 51.

### 8.3 Clusters and Dust Grains

The results on clusters and dust in the MCs reflect the decreasing amount of heavy elements with decreasing metallicity. The dust from oxygen-rich AGB stars is predominantly inorganic and involves metals such as silicon, magnesium, and aluminum. The amount of alumina and silicate dust is therefore lower in the MCs than in IK Tau (see Table 19). Particularly, the alumina dust production is suppressed in the SMC case.

In Figure 52 and 53, the alumina grain size distributions for the LMC and the SMC, respectively, are presented. In the LMC, the distribution of the grain size peaks at  $\sim 115 \text{ \AA}$  and  $\sim 1000 \text{ \AA}$ , while the SMC model reveals alumina grains with average sizes of  $\sim 13 \text{ \AA}$  and  $115 \text{ \AA}$ . The models of the SMC and LMC oxygen-rich AGB stars predict lower amounts of alumina dust (see Table 19), which is consistent with observations (Sloan et al., 2008).

In Figure 54 and 55, the forsterite grain size distributions for the LMC and the SMC, respectively, are shown. Similar to alumina dust, the amount of silicates, produced in our models, depends on metallicity. The lower the metallicity, the less forsterite is synthesised.

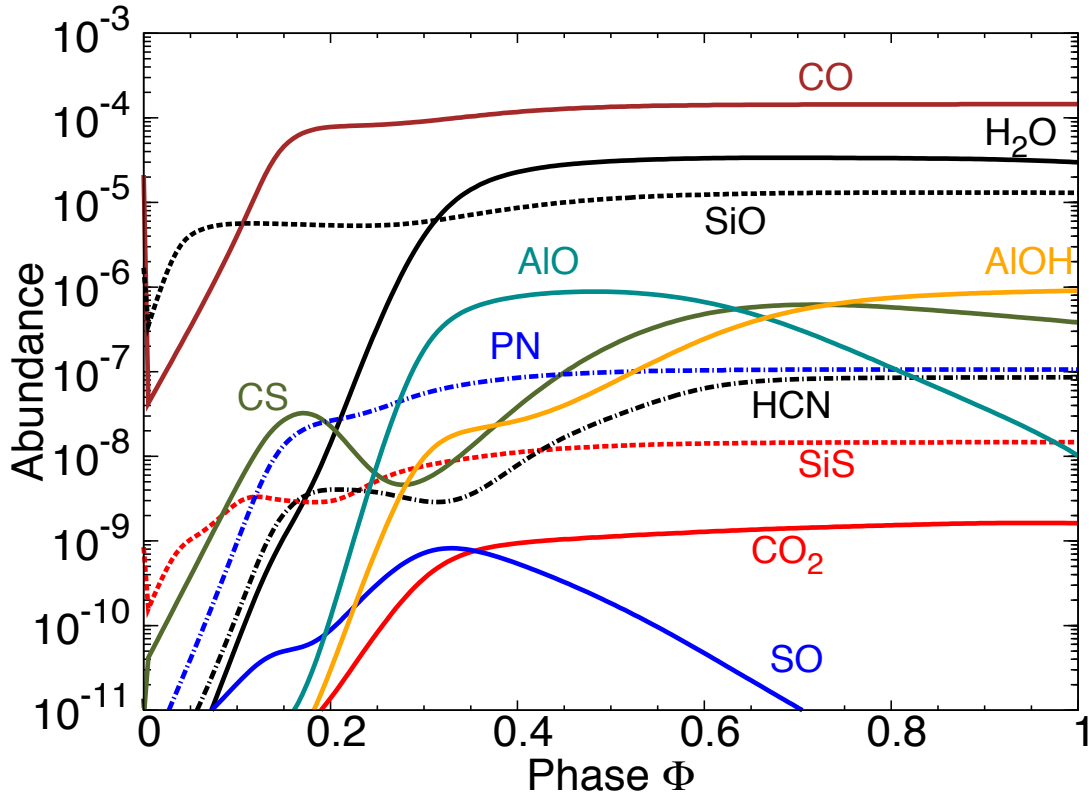


Figure 49: Molecular post-shock abundances as function of the pulsation phase  $\Phi$  in the first parcel at  $1 R_*$  of AGB star in the SMC ( $V_S = 32 \text{ km s}^{-1}$ ).

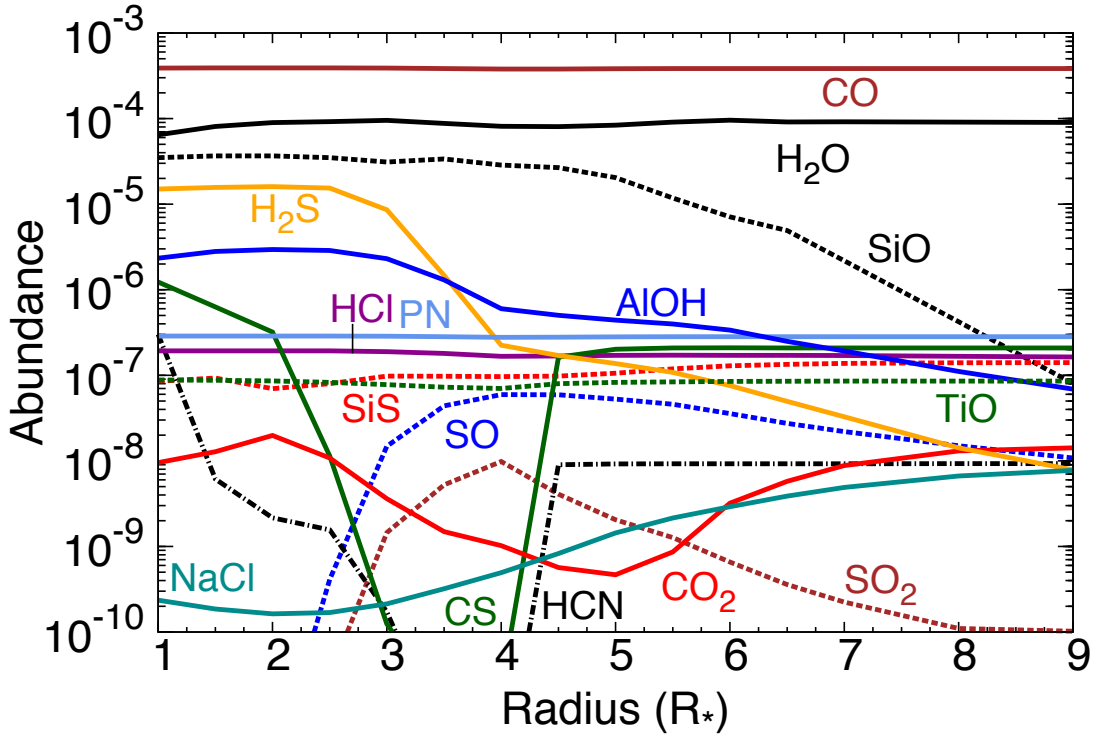


Figure 50: Post-shock fractional abundances as function of radius of AGB star in the LMC.

The average size of forsterite grains in the LMC is  $\sim 110 \text{ \AA}$  at  $9 R_*$ . In the SMC, the average size of forsterite grains at  $9 R_*$  is  $\sim 75 \text{ \AA}$ . In comparison to observations, who give

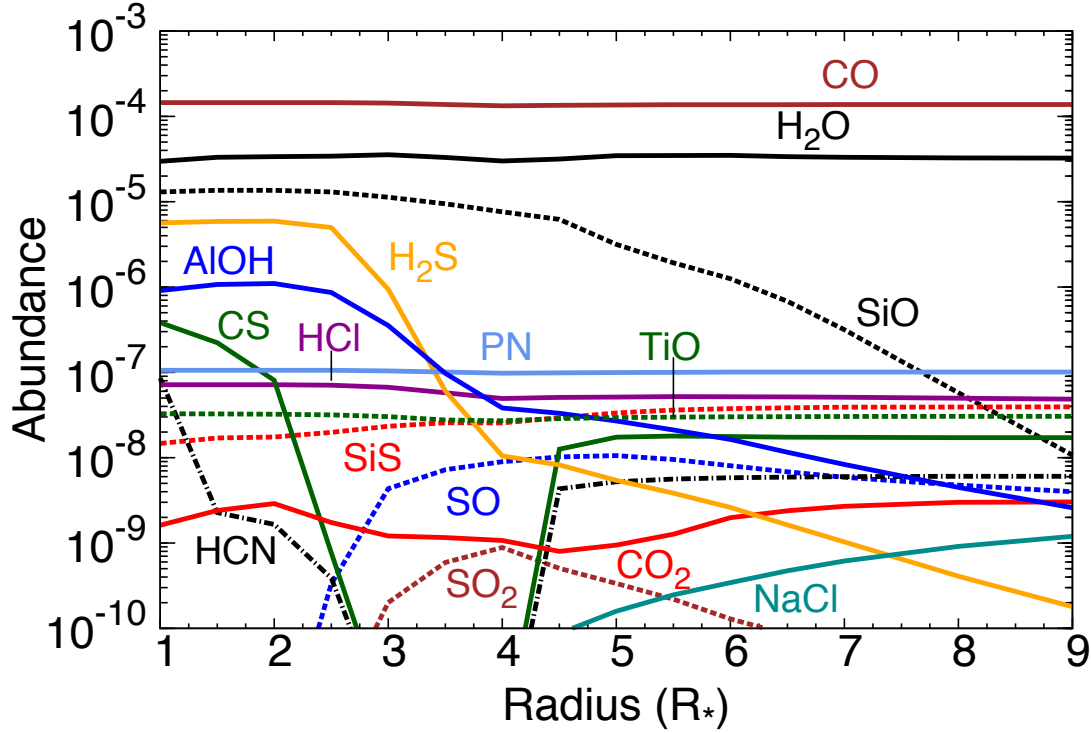


Figure 51: Post-shock fractional abundances as function of radius of AGB star in the SMC.

Table 19: Comparison of the dust-to-gas mass ratio as function of radius and metallicity. The notation  $X(Y) \equiv X \times 10^Y$  is used.

Radius ( $R_*$ )	SMC Mira	LMC Mira	IK Tau
1.0	7.9(-9)	2.1(-6)	2.1(-5)
1.5	1.0(-8)	2.6(-6)	2.7(-5)
2.0	1.3(-8)	3.2(-6)	3.3(-5)
3.5	6.5(-5)	1.2(-4)	1.3(-4)
4.0	1.3(-4)	3.7(-4)	4.6(-4)
5.0	1.8(-4)	5.4(-4)	7.3(-4)
8.0	3.1(-4)	9.7(-4)	1.7(-3)
9.0	3.5(-4)	1.1(-3)	2.0(-3)

an oxygen dust-to-gas mass ratios of the order  $10^{-3}$  -  $10^{-2}$  for oxygen-rich stars (Matsuura et al., 2009), the derived dust-to-gas mass ratios are lower in our model, as can be seen in Table 19.

Observational studies showed, that the AGB dust production rate depends on metallicity for oxygen-rich stars, but carbon stars with similar pulsation properties produce similar quantities of dust, regardless of their initial metallicity (Sloan et al., 2008). Moreover, the AGB dust synthesis in the LMC and the SMC is mainly provided by extreme carbon stars (x-AGB), albeit they represent only a small population of stars. Moreover, dust from oxygen-rich stars may play a larger role in the LMC than in the SMC (Boyer et al., 2011). The observed trends of oxygen-rich AGB dust agree thus with our models, although the observed dust masses are higher than the modelled values.



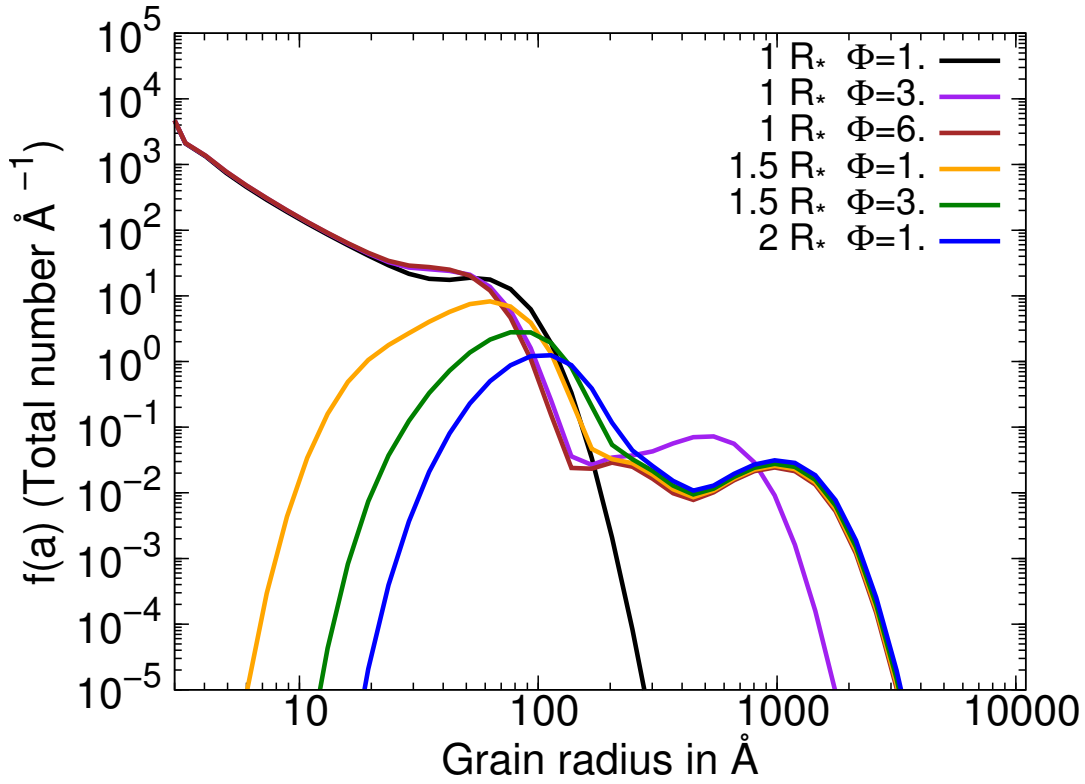


Figure 52: Alumina grain size distributions in the LMC as a function of radius.

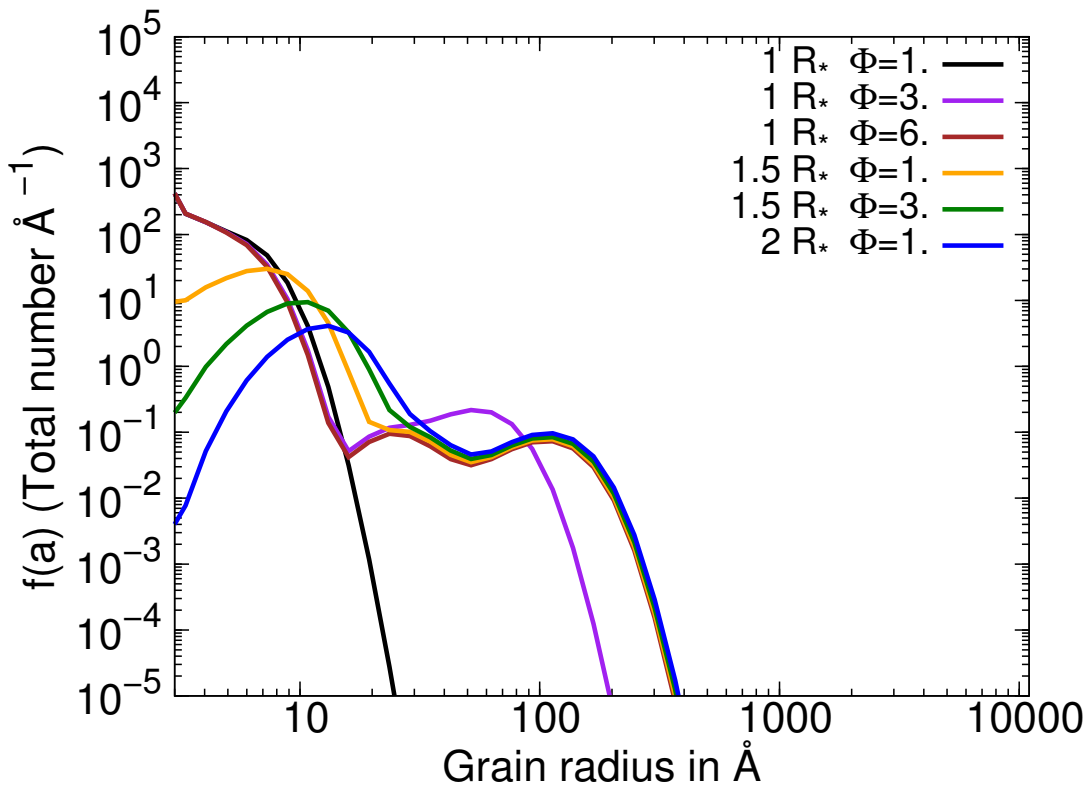


Figure 53: Alumina grain size distributions in the SMC model as a function of radius.

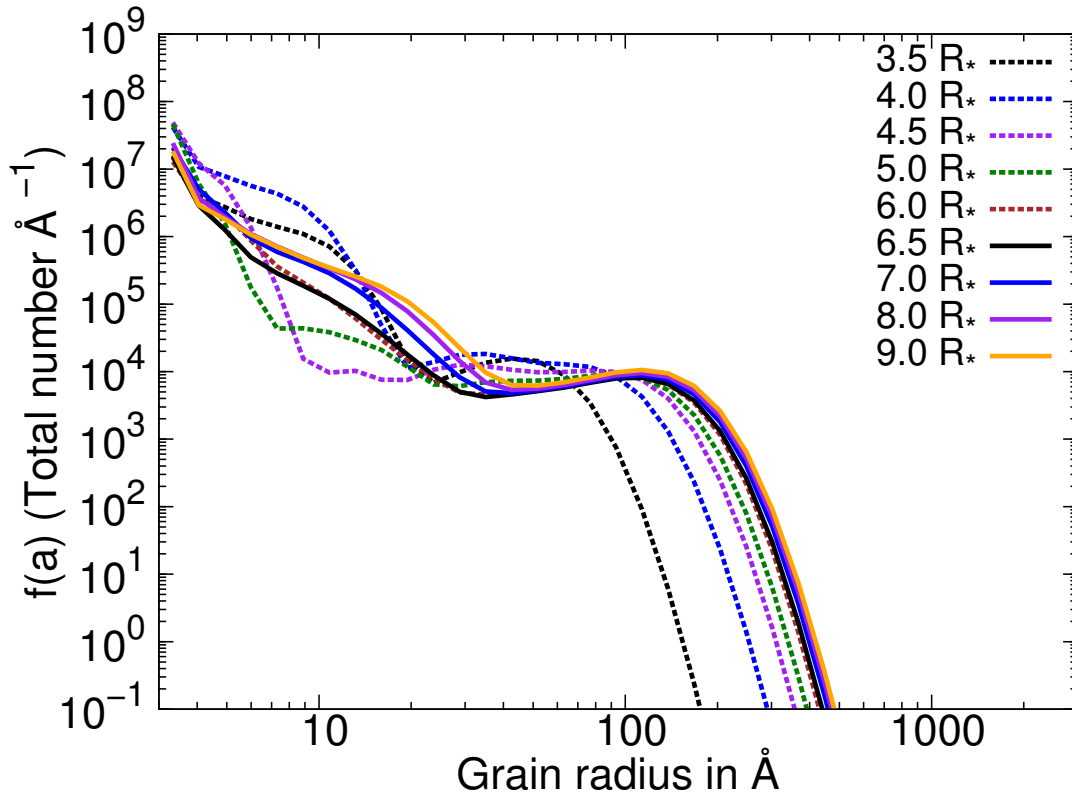


Figure 54: Forsterite grain size distributions in the LMC model as a function of radius.

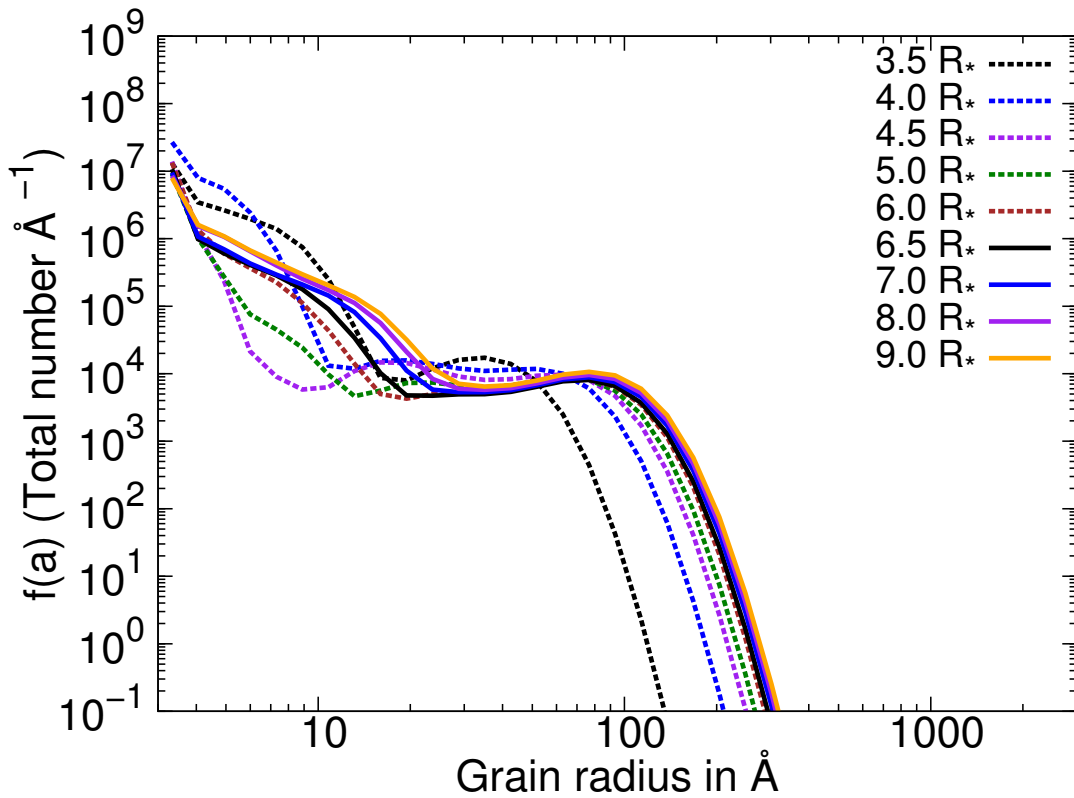


Figure 55: Forsterite grain size distributions in the SMC model as a function of radius.

## 9 Summary

In this thesis, the pulsation model (Cherchneff et al., 1992; Cherchneff, 2006, 2012; Duari et al., 1999) has been applied to oxygen-rich envelopes of AGB stars. Several models including various initial conditions (initial compositions, C/O ratio), gas conditions (temperature, density, shock velocity, timescales) and stellar evolution stage (AGB age, pulsation regularity, metallicity) have been developed, analysed and compared to observations. Moreover, the condensation of dust grains has been coupled to the gas phase via dust clusters. This is the first time a detailed and simultaneous description of the gas phase, the dust nucleation phase, and the dust condensation phase has been provided and applied to oxygen-rich stars on the AGB. Moreover, the developed models coherently and consistently account for the majority of the molecular observations and successfully explains the observed trends in dust formation and dust-to-gas mass ratios.

Owing to their young evolutionary state on the AGB, the models of the semi-regular stars have a gradually lower C/O ratio. As a consequence the carbonaceous species (e.g. HCN and CS) are formed to a lesser extent, as less carbon is available. However, it is prominent that close to the star, an active non-equilibrium chemistry takes place. As a result, the carbon-bearing species HCN, CS and CO<sub>2</sub> arise in gas shells close to the photosphere. This is a result of high temperature chemistry, releasing free carbon for CO and free nitrogen from N<sub>2</sub> and thus underlining the importance of pulsations. Whether the non-equilibrium species survive in the inner envelope, depends on the specific model.

For efficient dust condensation, three criteria are crucial: The timescale given by the pulsation period, the prevailing gas density, and the availability of clusters. If the pulsation period is short (in the case of SRVs), the clusters lack the time to coagulate and thus the dust production is low. If the gas density is too low, the critical clusters have a too low probability to coalesce and coagulate. Although too hot conditions are not favourable for dust formation, the temperature is not a crucial factor for condensation in the models, however, it plays a role for the cluster formation. The condensation formalism is based on thermal Brownian motion of the constituent dust grains. High temperatures lead to a collisional fragmentation of the grains resulting in decreasing grain sizes. Possibly, the grains fragment into critical clusters (dimers). Though fragmentation by collisions may be of minor importance at high temperatures. At high temperatures, radiative grain destruction may significantly contribute to grain fragmentations. Radiative processes are, however, not treated in the used condensation formalism and scope of future investigations. Having only a fraction of the heavy elements present in the Milky Way, the LMC and SMC circumstellar models provide less dust clusters (dust precursors), namely SiO, AlO and AlOH, from the gas phase as the galactic models do. Global dust budgets of the MCs are dominated by carbonaceous dust. Most of this dust is provided by extreme carbon stars (x-AGB), albeit they represent only a small population of stars.

## References

- Agúndez, M., Cernicharo, J., & Guelin, M. 2010, *apjl*, 724, L133
- Agúndez, M., Cernicharo, J., Pardo, J. R., Guélin, M., & Phillips, T. G. 2008, *aap*, 485, L33
- Arrhenius, S. 1899
- Asplund, M., Grevesse, N., Sauval, A. J., & Scott, P. 2009, *araa*, 47, 481
- Banerjee, D. P. K., Varricatt, W. P., Ashok, N. M., & Launila, O. 2003, *apjl*, 598, L31
- Bertschinger, E. & Chevalier, R. A. 1985, *apj*, 299, 167
- Boothroyd, A. I. & Sackmann, I.-J. 1991, *jrase*, 85, 204
- Bowen, G. H. 1988, *apj*, 329, 299
- Boyer, M. L., Srinivasan, S., Riebel, D., McDonald, I., van Loon, J. T., Clayton, G. C., Gordon, K. D., Meixner, M., Sargent, B. A., & Sloan, G. C. 2012, *apj*, 748, 40
- Boyer, M. L., Srinivasan, S., van Loon, J. T., McDonald, I., Meixner, M., Zaritsky, D., Gordon, K. D., Kemper, F., Babler, B., Block, M., Bracker, S., Engelbracht, C. W., Hora, J., Indebetouw, R., Meade, M., Misselt, K., Robitaille, T., Sewiło, M., Shiao, B., & Whitney, B. 2011, *aj*, 142, 103
- Cassisi, S. 2005, ArXiv Astrophysics e-prints
- Catoire, L., Legendre, F., & Giraud, M. 2003, *Journal of Propulsion and Power*, 19, 196
- Cau, P. 2002, *aap*, 392, 203
- Chase, M. W. 1986
- Cherchneff, I. 2006, *aap*, 456, 1001
- . 2011, *aap*, 526, L11
- . 2012, *aap*, 545, A12
- Cherchneff, I., Barker, J. R., & Tielens, A. G. G. M. 1992, *apj*, 401, 269
- Cherchneff, I. & Dwek, E. 2010, *apj*, 713, 1
- Cheung, A. C., Rank, D. M., Townes, C. H., Thornton, D. D., & Welch, W. J. 1968, *Physical Review Letters*, 21, 1701
- Cho, S.-H., Kim, J., & Yun, Y. 2014, *Journal of Korean Astronomical Society*, 47, 293
- Cioni, M.-R. L. 2009, *aap*, 506, 1137

- Cioni, M.-R. L., Girardi, L., Moretti, M. I., Piffi, T., Ripepi, V., Rubele, S., Scholz, R.-D., Bekki, K., Clementini, G., Ivanov, V. D., Oliveira, J. M., & van Loon, J. T. 2014, *aap*, 562, A32
- Cristallo, S., Piersanti, L., Straniero, O., Gallino, R., Domínguez, I., Abia, C., Di Rico, G., Quintini, M., & Bisterzo, S. 2011, *apjs*, 197, 17
- Danilovich, T., Bergman, P., Justtanont, K., Lombaert, R., Maercker, M., Olofsson, H., Ramstedt, S., & Royer, P. 2014, *aap*, 569, A76
- De Beck, E., Kamiński, T., Patel, N. A., Young, K. H., Gottlieb, C. A., Menten, K. M., & Decin, L. 2013, *aap*, 558, A132
- Decin, L., De Beck, E., Brünken, S., Müller, H. S. P., Menten, K. M., Kim, H., Willacy, K., de Koter, A., & Wyrowski, F. 2010a, *aap*, 516, A69
- Decin, L., Justtanont, K., De Beck, E., Lombaert, R., de Koter, A., Waters, L. B. F. M., Marston, A. P., Teyssier, D., Schöier, F. L., Bujarrabal, V., Alcolea, J., Cernicharo, J., Dominik, C., Melnick, G., Menten, K., Neufeld, D. A., Olofsson, H., Planesas, P., Schmidt, M., Szczerba, R., de Graauw, T., Helmich, F., Roelfsema, P., Dieleman, P., Morris, P., Gallego, J. D., Díez-González, M. C., & Caux, E. 2010b, *aap*, 521, L4
- Deguchi, S. & Goldsmith, P. F. 1985, *nat*, 317, 336
- Diamond, P. J. & Kemball, A. J. 1998, 30, 1349
- Duari, D., Cherchneff, I., & Willacy, K. 1999, *aap*, 341, L47
- Duley, W. W. 1985, *mnras*, 215, 259
- Dumm, T. & Schild, H. 1998, *na*, 3, 137
- Dwek, E. & Cherchneff, I. 2011, *apj*, 727, 63
- Feast, M. W. 1996, *mnras*, 278, 11
- Ferrarotti, A. S. & Gail, H.-P. 2006, *aap*, 447, 553
- Ford, K. E. S., Neufeld, D. A., Schilke, P., & Melnick, G. J. 2004, *apj*, 614, 990
- Fox, M. W. & Wood, P. R. 1982, *apj*, 259, 198
- . 1985, *apj*, 297, 455
- Frenklach, M. & Feigelson, E. D. 1989, *apj*, 341, 372
- Fu, R. R., Moullet, A., Patel, N. A., Biersteker, J., Derose, K. L., & Young, K. H. 2012, *apj*, 746, 42
- Gail, H.-P. & Sedlmayr, E. 1998, *Faraday Discussions*, 109, 303

- . 1999, *aap*, 347, 594
- Gautschy, A. 1999, *aap*, 349, 209
- Goumans, T. P. M. & Bromley, S. T. 2012, *mnras*, 420, 3344
- Groenewegen, M. A. T. 2006, *aap*, 448, 181
- Gullieuszik, M., Groenewegen, M. A. T., Cioni, M.-R. L., de Grijs, R., van Loon, J. T., Girardi, L., Ivanov, V. D., Oliveira, J. M., Emerson, J. P., & Guandalini, R. 2012, *aap*, 537, A105
- Habing, H. J. & Olofsson, H. 2003, *Asymptotic giant branch stars*, ed. H. J. Habing & H. Olofsson (Cambridge University press)
- Hackwell, J. A., Gerhz, R. D., & Woolf, N. J. 1970, *nat*, 227, 822
- Hale, D. D. S., Bester, M., Danchi, W. C., Hoss, S., Lipman, E., Monnier, J. D., Tuthill, P. G., Townes, C. H., Johnson, M., Lopez, B., & Geballe, T. R. 1997, *apj*, 490, 407
- Harwit, M. 1988, *Journal of the British Astronomical Association*, 98, 374
- Herwig, F. 2005, *araa*, 43, 435
- Herwig, F., Bloeker, T., Schoenberner, D., & El Eid, M. 1997, *aap*, 324, L81
- Hilditch, R. W., Howarth, I. D., & Harries, T. J. 2005, *mnras*, 357, 304
- Hindmarsh, A. C. 1980, *SIGNUM Newsl.*, 15, 10
- Hinkle, K. H., Lebzelter, T., & Scharlach, W. W. G. 1997, *aj*, 114, 2686
- Höfner, S. 1999, *aap*, 346, L9
- . 2008, *aap*, 491, L1
- Höfner, S., Gautschy-Loidl, R., Aringer, B., & Jørgensen, U. G. 2003, *aap*, 399, 589
- Hony, S., Waters, L. B. F. M., & Tielens, A. G. G. M. 2002, *aap*, 390, 533
- Iben, Jr., I. & Renzini, A. 1983, *araa*, 21, 271
- Jacobson, M. 2005, *Fundamentals of Atmospheric Modeling*
- Jenkins, E. B. 2009, *apj*, 700, 1299
- Jeong, K. S., Winters, J. M., Le Bertre, T., & Sedlmayr, E. 2003, *aap*, 407, 191
- Jones, O. C., Kemper, F., Srinivasan, S., McDonald, I., Sloan, G. C., & Zijlstra, A. A. 2014, *mnras*, 440, 631

- Joy, A. H. 1954, *apjs*, 1, 39
- Justtanont, K., Decin, L., Schöier, F. L., Maercker, M., & Olofsson, H. e. a. 2010, *aap*, 521, L6
- Justtanont, K., Feuchtgruber, H., de Jong, T., Cami, J., Waters, L. B. F. M., Yamamura, I., & Onaka, T. 1998, *aap*, 330, L17
- Kamiński, T., Gottlieb, C. A., Menten, K. M., Patel, N. A., Young, K. H., Brünken, S., Müller, H. S. P., McCarthy, M. C., Winters, J. M., & Decin, L. 2013, *aap*, 551, A113
- Kaminski, T., Gottlieb, C. A., Young, K. H., Menten, K. M., & Patel, N. A. 2013, *ArXiv e-prints*, in, prep.
- Kamiński, T., Schmidt, M. R., & Menten, K. M. 2013, *aap*, 549, A6
- Karakas, A. & Lattanzio, J. C. 2007, *pasa*, 24, 103
- Karakas, A. I. 2010, *mnras*, 403, 1413
- Karovicova, I., Wittkowski, M., Ohnaka, K., Boboltz, D. A., Fossat, E., & Scholz, M. 2013, *aap*, 560, A75
- Kemper, F., Waters, L. B. F. M., de Koter, A., & Tielens, A. G. G. M. 2001, *aap*, 369, 132
- Kerschbaum, F. & Hron, J. 1992, *aap*, 263, 97
- . 1996, *aap*, 308, 489
- Kerschbaum, F., Olofsson, H., & Hron, J. 1996, *aap*, 311, 273
- Khouri, T., de Koter, A., Decin, L., Waters, L. B. F. M., Lombaert, R., Royer, P., Swinyard, B., Barlow, M. J., Alcolea, J., Blommaert, J. A. D. L., Bujarrabal, V., Cernicharo, J., Groenewegen, M. A. T., Justtanont, K., Kerschbaum, F., Maercker, M., Marston, A., Matsuura, M., Melnick, G., Menten, K. M., Olofsson, H., Planesas, P., Polehampton, E., Posch, T., Schmidt, M., Szczerba, R., Vandenbussche, B., & Yates, J. 2014a, *aap*, 561, A5
- Khouri, T., de Koter, A., Decin, L., Waters, L. B. F. M., Maercker, M., Lombaert, R., Alcolea, J., Blommaert, J. A. D. L., Bujarrabal, V., Groenewegen, M. A. T., Justtanont, K., Kerschbaum, F., Matsuura, M., Menten, K. M., Olofsson, H., Planesas, P., Royer, P., Schmidt, M. R., Szczerba, R., Teyssier, D., & Yates, J. 2014b, *aap*, 570, A67
- Kim, H., Wyrowski, F., Menten, K. M., & Decin, L. 2010, *aap*, 516, A68
- Knapp, G. R. & Morris, M. 1985, *apj*, 292, 640
- Lamers, H. J. G. L. M. & Cassinelli, J. P. 1999, *Introduction to Stellar Winds*

- Le Sidaner, P. & Le Bertre, T. 1996, aap, 314, 896
- Lebzelter, T., Hinkle, K. H., Wood, P. R., Joyce, R. R., & Fekel, F. C. 2005, aap, 431, 623
- Lebzelter, T., Kerschbaum, F., & Hron, J. 1995, aap, 298, 159
- Li, R. & Cheng, L. 2012, ctc, 996, 125
- Li, Z. H. & Truhlar, D. G. 2008, The Journal of Physical Chemistry C, 112, 11109
- Lindqvist, M., Nyman, L.-A., Olofsson, H., & Winnberg, A. 1988, aap, 205, L15
- Little-Marenin, I. R. & Little, S. J. 1979, aj, 84, 1374
- . 1990, aj, 99, 1173
- Lodders, K. 1999, Journal of Physical and Chemical Reference Data, 28, 1705
- Maercker, M. 2009
- Markwick, A. J. & Millar, T. J. 2000, aap, 359, 1162
- Matsuura, M., Barlow, M. J., Zijlstra, A. A., Whitelock, P. A., Cioni, M.-R. L., Groenewegen, M. A. T., Volk, K., Kemper, F., Kodama, T., Lagadec, E., Meixner, M., Sloan, G. C., & Srinivasan, S. 2009, mnras, 396, 918
- Mattsson, L., Höfner, S., & Herwig, F. 2007, aap, 470, 339
- McClean, R. E., Nelson, H. H., & Campbell, M. L. 1993, The Journal of Physical Chemistry, 97, 9673
- McElroy, D., Walsh, C., Markwick, A. J., Cordiner, M. A., Smith, K., & Millar, T. J. 2013, aap, 550, A36
- Melnick, G. J., Neufeld, D. A., Ford, K. E. S., Hollenbach, D. J., & Ashby, M. L. N. 2001, nature, 412, 160
- Menten, K. M., Wyrowski, F., Alcolea, J., De Beck, E., Decin, L., Marston, A. P., Bujarbal, V., Cernicharo, J., Dominik, C., Justtanont, K., de Koter, A., Melnick, G., Neufeld, D. A., Olofsson, H., Planesas, P., Schmidt, M., Schöier, F. L., Szczerba, R., Teyssier, D., Waters, L. B. F. M., Edwards, K., Olberg, M., Phillips, T. G., Morris, P., Salez, M., & Caux, E. 2010, aap, 521, L7
- Milam, S. N., Apponi, A. J., Woolf, N. J., & Ziurys, L. M. 2007, apjl, 668, L131
- Molster, F. J., Waters, L. B. F. M., & Kemper, F. 2010, 815, 143
- Molster, F. J., Waters, L. B. F. M., Trams, N. R., Van Winckel, H., Decin, L., van Loon, J. T., Jäger, C., Henning, T., Käufel, H.-U., de Koter, A., & Bouwman, J. 1999, aap, 350, 163



- Neufeld, D. A., González-Alfonso, E., Melnick, G. J., Szczerba, R., Schmidt, M., Decin, L., de Koter, A., Schöier, F., & Cernicharo, J. 2011, *apjl*, 727, L28
- Neugebauer, G., Martz, D. E., & Leighton, R. B. 1965, *apj*, 142, 399
- NIST. 2000
- Nowotny, W., Höfner, S., & Aringer, B. 2010, *aap*, 514, A35
- O’Gorman, E., Vlemmings, W., Richards, A. M. S., Baudry, A., De Beck, E., Decin, L., Harper, G. M., Humphreys, E. M., Kervella, P., Khouri, T., & Muller, S. 2015, *aap*, 573, L1
- Olivier, E. A., Whitelock, P., & Marang, F. 2001, *mnras*, 326, 490
- Olofsson, H., González Delgado, D., Kerschbaum, F., & Schöier, F. L. 2002, *aap*, 391, 1053
- Olofsson, H., Lindqvist, M., Nyman, L.-A., & Winnberg, A. 1998, *aap*, 329, 1059
- Olofsson, H., Lindqvist, M., Winnberg, A., Nyman, L.-A., & Nguyen-Q-Rieu. 1991, *aap*, 245, 611
- Omont, A., Lucas, R., Morris, M., & Guilloteau, S. 1993, *aap*, 267, 490
- Onaka, T., de Jong, T., & Willems, F. J. 1989, *aap*, 218, 169
- Palik, E. D. 1991
- Patzer, A. B. C., Chang, C., Sedlmayr, E., & Sülzle, D. 2005, *European Physical Journal D*, 32, 329
- Pietrzyński, G., Graczyk, D., Gieren, W., Thompson, I. B., Pilecki, B., Udalski, A., Soszyński, I., Kozłowski, S., Konorski, P., Suchomska, K., Bono, G., Moroni, P. G. P., Villanova, S., Nardetto, N., Bresolin, F., Kudritzki, R. P., Storm, J., Gallenne, A., Smolec, R., Minniti, D., Kubiak, M., Szymański, M. K., Poleski, R., Wyrzykowski, Ł., Ulaczyk, K., Pietrukowicz, P., Górski, M., & Karczmarek, P. 2013, *nat*, 495, 76
- Plane, J. M. C. 2013, *Royal Society of London Philosophical Transactions Series A*, 371, 20335
- Posch, T., Kerschbaum, F., Mutschke, H., Fabian, D., Dorschner, J., & Hron, J. 1999, *aap*, 352, 609
- Ramstedt, S., Schöier, F. L., & Olofsson, H. 2009, *aap*, 499, 515
- Ramstedt, S., Schöier, F. L., Olofsson, H., & Lundgren, A. A. 2008, *aap*, 487, 645
- Samus, N. N., Durlevich, O. V., & Kazarovets, R. V. 1997, *Baltic Astronomy*, 6, 296

- Sanchez Contreras, C., Velilla Prieto, L., Cernicharo, J., Alcolea, J., Pardo, J. R., Agundez, M., Bujarrabal, V., Herpin, F., Menten, K. M., & Wyroszky, F. 2011, 280, 327P
- Sarangi, A. & Cherchneff, I. 2014, aap, 1, 1
- Saunders, R. & Plane, J. 2006, *Journal of Aerosol Science*, 37, 1737
- Scalo, J. M. & Slavsky, D. B. 1980, *apjl*, 239, L73
- Schöier, F. L., Bast, J., Olofsson, H., & Lindqvist, M. 2007, aap, 473, 871
- Schöier, F. L., Maercker, M., Justtanont, K., Olofsson, H., Black, J. H., Decin, L., de Koter, A., & Waters, R. 2011, aap, 530, A83
- Schöier, F. L., Olofsson, H., Wong, T., Lindqvist, M., & Kerschbaum, F. 2004, aap, 422, 651
- Schöier, F. L., Ramstedt, S., Olofsson, H., Lindqvist, M., Biegging, J. H., & Marvel, K. B. 2013, aap, 550, A78
- Seale, J. P., Meixner, M., Sewiło, M., Babler, B., Engelbracht, C. W., Gordon, K., Hony, S., Misselt, K., Montiel, E., Okumura, K., Panuzzo, P., Roman-Duval, J., Sauvage, M., Boyer, M. L., Chen, C.-H. R., Indebetouw, R., Matsuura, M., Oliveira, J. M., Srinivasan, S., van Loon, J. T., Whitney, B., & Woods, P. M. 2014, *aj*, 148, 124
- Sharipov, A., Titova, N., & Starik, A. 2011, *The Journal of Physical Chemistry A*, 115, 4476, PMID: 21469719
- Shingles, L. J. & Karakas, A. I. 2013, *mnras*, 431, 2861
- Sloan, G. C., Kraemer, K. E., Goebel, J. H., & Price, S. D. 2003, *apj*, 594, 483
- Sloan, G. C., Kraemer, K. E., Wood, P. R., Zijlstra, A. A., Bernard-Salas, J., Devost, D., & Houck, J. R. 2008, *apj*, 686, 1056
- Smolders, K., Verhoelst, T., Neyskens, P., Blommaert, J. A. D. L., Decin, L., Van Winckel, H., Van Eck, S., Sloan, G. C., Cami, J., Hony, S., De Cat, P., Menu, J., & Vos, J. 2012, aap, 543, L2
- Speck, A. K. 1998
- Straniero, O., Cristallo, S., & Piersanti, L. 2014, *apj*, 785, 77
- Swihart, M., Catoire, L., Legrand, B., Gokalp, I., & Paillard, C. 2003, *Combustion and Flame*, 132, 91
- Tenenbaum, E. D. & Ziurys, L. M. 2009, *apjl*, 694, L59
- . 2010, *apjl*, 712, L93

- Tielens, A. G. G. M. 2010
- Tsuji, T. 1973, aap, 23, 411
- Uttenthaler, S., van Stiphout, K., Voet, K., van Winckel, H., van Eck, S., Jorissen, A., Kerschbaum, F., Raskin, G., Prins, S., Pessemier, W., Waelkens, C., Frémat, Y., Hensberge, H., Dumortier, L., & Lehmann, H. 2011, aap, 531, A88
- Vassiliadis, E. & Wood, P. R. 1993, apj, 413, 641
- Velilla Prieto, L., Sánchez Contreras, C., Cernicharo, J., Alcolea, J., Agúndez, M., Pardo, J. R., Bujarrabal, V., Herpin, F., Menten, K. M., & Wyrowsky, F. 2013, 676
- Verhoelst, T., Decin, L., van Malderen, R., Hony, S., Cami, J., Eriksson, K., Perrin, G., Deroo, P., Vandenbussche, B., & Waters, L. B. F. M. 2006, aap, 447, 311
- Wachter, A., Winters, J. M., Schröder, K.-P., & Sedlmayr, E. 2008, aap, 486, 497
- Waters, L. B. F. M., Molster, F. J., de Jong, T., Beintema, D. A., Waelkens, C., Boogert, A. C. A., Boxhoorn, D. R., de Graauw, T., Drapatz, S., Feuchtgruber, H., Genzel, R., Helmich, F. P., Heras, A. M., Huygen, R., Izumiura, H., Justtanont, K., Kester, D. J. M., Kunze, D., Lahuis, F., Lamers, H. J. G. L. M., Leech, K. J., Loup, C., Lutz, D., Morris, P. W., Price, S. D., Roelfsema, P. R., Salama, A., Schaeidt, S. G., Tielens, A. G. G. M., Trams, N. R., Valentijn, E. A., Vandenbussche, B., van den Ancker, M. E., van Dishoeck, E. F., Van Winckel, H., Wesseliuss, P. R., & Young, E. T. 1996, aap, 315, L361
- Wenger, M., Ochsenbein, F., Egret, D., Dubois, P., Bonnarel, F., Borde, S., Genova, F., Jasniewicz, G., Laloë, S., Lesteven, S., & Monier, R. 2000, aaps, 143, 9
- White, W. B., Johnson, S. M., & Dantzig, G. B. 1958, J. Chem. Phys., 28, 751
- Willacy, K. & Cherchneff, I. 1998, aap, 330, 676
- Willson, L. A. & Bowen, G. W. 1984, 127
- Wing, R. F. & Lockwood, G. W. 1973, apj, 184, 873
- Winters, J. M., Le Bertre, T., Jeong, K. S., Helling, C., & Sedlmayr, E. 2000, aap, 361, 641
- Woitke, P. 2006, aap, 460, L9
- Wood, P. R. & Sebo, K. M. 1996, mnras, 282, 958
- Woodley, S. 2009, Materials and Manufacturing Processes, 24, 255
- Woodley, S. M. 2011, Proc. R. Soc. A, 467, 2020
- Yamamura, I., de Jong, T., Onaka, T., Cami, J., & Waters, L. B. F. M. 1999, aap, 341, L9
- Yamamura, I., Kawaguchi, K., & Ridgway, S. T. 2000, apjl, 528, L33

Zachariah, M. & Tsang, W. 1993, *Aerosol Science and Technology*, 19, 499

—. 1995, *The Journal of Physical Chemistry*, 99, 5308

Zhao-Geisler, R., Quirrenbach, A., Köhler, R., Lopez, B., & Leinert, C. 2011, *aap*, 530, A120

Zhukovska, S. & Henning, T. 2014, *ArXiv e-prints*

Ziurys, L. M. 2006, *Proceedings of the National Academy of Science*, 103, 12274

# DAVID GOBRECHT

## PERSONAL DATA

---

PLACE AND DATE OF BIRTH: BADEN, SWITZERLAND | 08 DECEMBER 1985  
NATIONALITY: SWISS | GERMAN  
ADDRESS: VIA MARIA MORGANTI 8, 64100 TERAMO, ITALY  
PHONE: +39 327 2668624  
EMAIL: [DAVID.GOBRECHT@INAF.IT](mailto:DAVID.GOBRECHT@INAF.IT)  
HOMEPAGE: [WWW.GOBRECHT.CH/DAVE.HTM](http://WWW.GOBRECHT.CH/DAVE.HTM)



## EDUCATION

---

- FEBRUARY 2015 *PhD thesis defence and examination*
- FEB 2011 - FEB 2015 PHD STUDIES “DUST SYNTHESIS IN EVOLVED OXYGEN-RICH AGB STARS”  
IN THE SUBJECT *Theoretical Physics*  
PHYSICS DEPARTMENT, **University of Basel**, SWITZERLAND  
THESIS ADVISOR: PD DR ISABELLE CHERCHNEFF
- SEP 2008 - DEC 2010 MASTER STUDIES IN *Theoretical Physics*  
PHYSICS DEPARTMENT, **University of Basel**, SWITZERLAND  
ADVISORS: PROF FRIEDRICH-KARL THIELEMANN & PD DR AHMAD A. HUJEIRAT
- JAN - DEC 2010 MASTER THESIS “ON THE SETTLING OF MATTER ON NEUTRON STARS”  
PHYSICS DEPARTMENT, **University of Basel**, SWITZERLAND  
LANDESSTERNWARTE, **University of Heidelberg**, GERMANY  
ADVISORS: PROF FRIEDRICH-KARL THIELEMANN & PD DR AHMAD A. HUJEIRAT
- DECEMBER 2009 MASTER EXAM IN *Plasma physics* AND *Nuclear Astrophysics*  
PHYSICS DEPARTMENT, **University of Basel**, SWITZERLAND  
EXAMINATORS: PROF MATTHIAS LIEBENDÖRFER & PD DR THOMAS RAUSCHER
- MAY - OCT 2009 MASTER PROJECT “ACCRETION AROUND STRONGLY MAGNETISED NEUTRON STARS”  
PHYSICS DEPARTMENT, **University of Basel**, SWITZERLAND  
LANDESSTERNWARTE, **University of Heidelberg**, GERMANY  
ADVISORS: PROF FRIEDRICH-KARL THIELEMANN & PD DR AHMAD A. HUJEIRAT
- SEP 2005 - SEP 2008 BACHELOR STUDIES IN *Physics*  
PHYSICS DEPARTMENT, **University of Basel**, SWITZERLAND
- SEP 2001 - SEP 2005 HIGH SCHOOL “HOCHRHEIN-GYMNASIUM”,  
CONCLUDED SUCCESSFULLY WITH THE “ABITUR”  
WALDSHUT, GERMANY
- AUG - SEP 2001 ECONOMY HIGH SCHOOL “WIRTSCHAFTSMITTELSCHULE (WMS)”  
AARAU, SWITZERLAND
- AUG 1997 - AUG 2001 SECONDARY SCHOOL “BEZIRKSSCHULE”  
WINDISCH, SWITZERLAND

AUG 1992 - AUG 1997    PRIMARY SCHOOL "BRÜHL"  
GEBENSTORF, SWITZERLAND

## PROFESSIONAL EXPERIENCE

---

MAY 2015 - NOW	POSTDOCTORAL RESEARCH FELLOWSHIP "ADVANCES IN AGB MODELLING" AT THE ASTRONOMICAL OBSERVATORY (INAF-OACTe) IN TERAMO, ITALY ADVISOR: DR. SERGIO CRISTALLO
MAY 2010 - FEB 2015	SCIENTIFIC ASSISTANT AND TUTOR AT THE UNIVERSITY OF BASEL TUTOR IN MECHANICS, THERMODYNAMICS, ASTRONOMY AND EXPERIMENTAL PHYSICS, INCLUDING ADMINISTRATION AND LECTURE REPRESENTATION FOR PROF. F.-K. THIELEMANN
NOV 2010 - FEB 2011	MATH TEACHER AT BEZIRKSSCHULE WETTINGEN, SWITZERLAND TEACHING MATHEMATICS FOR 7TH YEAR PUPILS
AUGUST 2010	MATH TEACHER AT BEZIRKSSCHULE SCHÖFTLAND, SWITZERLAND TEACHING MATHEMATICS AND GEOMETRICAL DRAWING FOR 7TH - 9TH YEAR PUPILS
JUNE 2006 - JULY 2007	SCIENTIFIC WORK AT PSI IN VILLIGEN, SWITZERLAND INTERPRETATION OF SATELLITE DATA AND ANALYSIS OF GAMMA RAY BURSTS (GRB'S)
AUGUST 2006	TECHNICAL ASSISTANT AT THE ICN+T CONFERENCE IN BASEL
JULY 2005 - OCT 2009	PART-TIME JOB AT DENNER AG IN BRUGG AND BASEL (FROM 2008 ON) IN THE WORKING DOMAINS CASHIER, FLOORMAN AND CLEANER
MAY 2002	PRACTICAL COURSE AT ALSTOM IN BADEN, SWITZERLAND IN THE INTELLECTUAL PROPERTY AND PATENT SECTION OF ALSTOM

## PUBLICATIONS, TALKS, POSTERS

---

### Publications

DUST FORMATION IN THE OXYGEN-RICH AGB STAR IK TAURI  
GOBRECHT, D.; CHERCHNEFF, I.; SARANGI, A.; PLANE, J. M. C.; BROMLEY, S. T.  
ASTRONOMY & ASTROPHYSICS, VOL. 585, P. 6, 2016

DUST FORMATION IN THE INNER WIND OF THE OXYGEN-RICH AGB STAR IK TAU  
GOBRECHT, D.; CHERCHNEFF, I.; SARANGI, A.  
ASTRONOMICAL SOCIETY OF THE PACIFIC CONFERENCE SERIES, VOL. 497, P. 321, 2015

EVOLUTION, NUCLEOSYNTHESIS, AND YIELDS OF AGB STARS AT DIFFERENT METALLICITIES.  
III. INTERMEDIATE-MASS MODELS, REVISED LOW-MASS MODELS, AND THE PH-FRUITY INTERFACE  
CRISTALLO, S.; STRANIERO, O.; PIERSANTI, L.; GOBRECHT, D.  
ASTROPHYSICAL JOURNAL SUPPLEMENT SERIES, VOL. 219, P. 40, 2015

FROM NUCLEI TO DUST GRAINS: HOW THE AGB MACHINERY WORKS  
GOBRECHT, D.; CRISTALLO, S.; PIERSANTI, L.  
EUROPEAN ASTRONOMICAL SOCIETY PUBLICATIONS SERIES, VOL. 71, P. 251, 2015

## GRANTED OBSERVATION TIMES AND SUPERCOMPUTER ACCESS TIMES

---

- NOVEMBER 2015 SUCCESSFUL APPLICATION FOR MACHINE TIME (128'000 CPU HOURS)  
ON THE GALILEO CLUSTER AT CINECA IN BOLOGNA, ITALY
- NOVEMBER 2012 SUCCESSFUL APPLICATION FOR COMPUTING TIME  
AT THE HIGH PERFORMANCE COMPUTER (HPC) IN BARCELONA, SPAIN
- JULY 2013 OBSERVATIONS AT THE IRAM 30M TELESCOPE  
IN GRANADA, SPAIN
- FEBRUARY 2013 OBSERVATIONS AT THE OSO 25M TELESCOPE  
IN ONSALA, SWEDEN

## AWARDS

---

- JUNE 2005 MEMBERSHIP OF THE GERMAN PHYSICAL SOCIETY (DPG)  
FOR DISTINGUISHED WORK IN THE SCHOOL SUBJECT PHYSICS

## LANGUAGES

---

- GERMAN NATIVE, MOTHER-TONGUE
- ENGLISH EXCELLENT KNOWLEDGE IN READING, WRITING AND SPEAKING  
DEEPENED BY MULTIPLE LANGUAGE STUDIES IN ENGLAND: PAIGNTON (2001) AND MALTA: GZIRA (2003)
- FRENCH EXCELLENT KNOWLEDGE IN READING, WRITING AND SPEAKING  
DEEPENED BY MULTIPLE LANGUAGE STUDIES IN FRANCE: LA ROCHELLE (2004) AND BLOIS (2002, 2003)
- ITALIAN BEGINNER LEVEL

## IT SKILLS

---

- BASIC KNOWLEDGE: ORIGIN, OSX, SHELL-SRIPTING
- ADVANCED KNOWLEDGE: FORTRAN, HTML, LINUX, UBUNTU,  $\LaTeX$ , GNUPLOT, MATLAB,  
HIGH-PERFORMANCE COMPUTING, EXCEL, WORD, POWERPOINT

## INTERESTS AND ACTIVITIES

---

TECHNOLOGY, OPEN-SOURCE, PROGRAMMING  
SKIING, BIKING, CLIMBING, PLAYING THE PIANO